Master Thesis in Geosciences

Reactivity of alum and black shale in the Oslo region, Norway

By Abreham Yacob Abreham

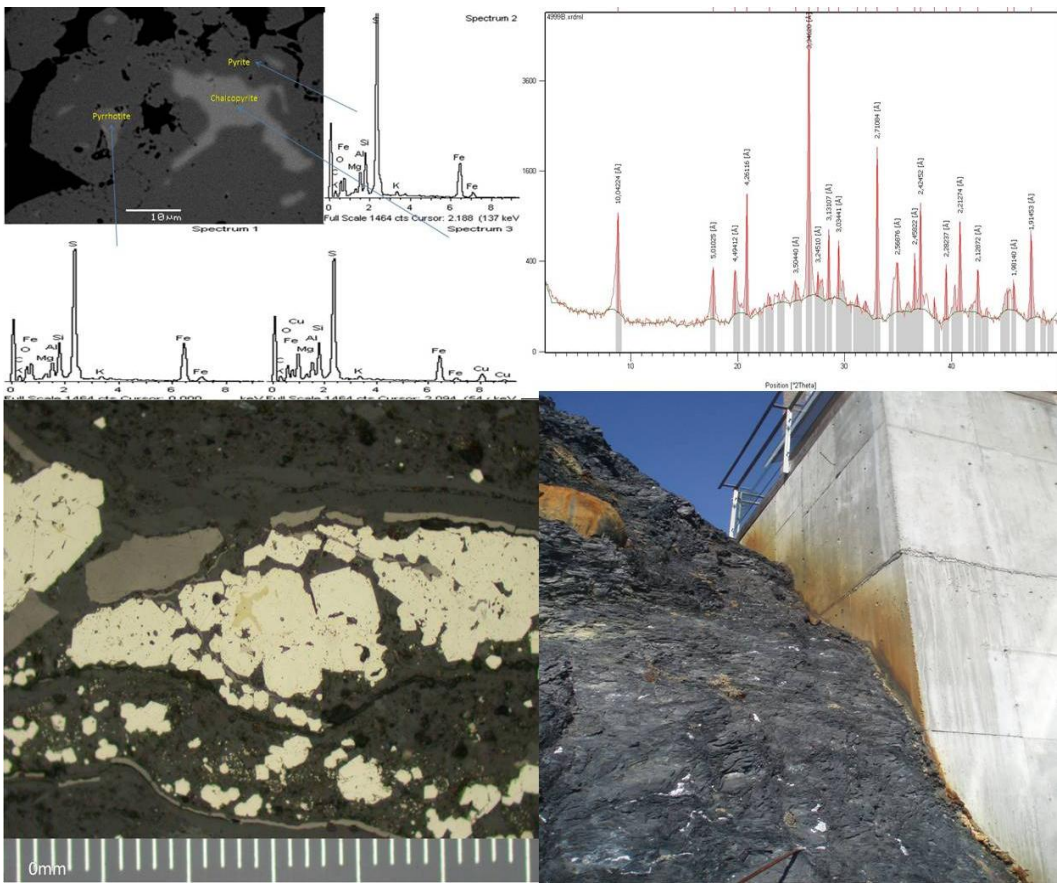

UNIVERSITY OF OSLO

FACULTY OF MATHEMATICS AND NATURAL SCIENCES

Reactivity of alum and black shale in the Oslo region, Norway

By Abreham Yacob Abreham

Master Thesis in Geosciences

Discipline: Environmental Geology and Geohazards

Department of Geosciences

Faculty of Mathematics and Natural Sciences

UNIVERSITY OF OSLO

December, 2007

Tutor(s): Professor Per Aagaard (Geosciences, UIO), Dr. Per Hemil (Multiconsult), Dr. Odd Nilsen (Geosciences, UIO)

This work is published digitally through DUO – Digitale Utgivelser ved UiO

http://www.duo.uio.no

It is also catalogued in BIBSYS (http://www.bibsys.no/english)

Acknowledgements

My first and foremost heartfelt gratitude goes to my research supervisor, Professor Per Aagaard, for his encouragement, guidance and assistance. My special thanks also go to Dr. Odd Nilsen, my second supervisor from the Department of Geosciences University of Oslo, and Dr Per Hemli, my external supervisor from Multiconsult, for his support and constructive comments.

I would also like to express my gratefulness to Dr Kim Rudolph-Lund, who is the leader of black shale research from NGI, for his inspiring, supportive and constructive comments. His dedication and enthusiastic support even while he was outside Norway helped me to materialize this work. I respectfully thank Mr. Tor Løken from NGI for his help in sampling and field description.

My gratitude, in a sense of debt, also goes Ms Marit Carlsen, student advisor at the Department of Geosciences, University Oslo who has made my study in the department easy and comfortable with warm welcome to entertain and come up with solutions for all the questions and problems I had in the last two years.

Finally, most of the job was done in the laboratory of the institute and I was inspired by the charming staff, specially Miss Berit Løken, Mr Mufak Naoroz, Miss Turid Winje and Mr Benites Tulio Eloy for their enthusiastic technical and professional support in the laboratory.

Oslo, December 2007
Abreham Yacob Abreham

Abstract

Mineralogical and chemical analysis of alum shale and black shale samples were done using the XRD, XRF, sulfur chemical analysis, petrographic and scanning electron microscopy. Samples from two study areas in the Oslo region, Konows gate and Slemmestad have abundant of quartz and pyrite. Calcite and gypsum minerals were also found in the Konows gate and Slemmestad areas samples. Other minerals in small concentrations such as barite, chalcopyrite, pyrrhotite, sphalerite and dolomite were detected by the petrographic and scanning electron microscopy.

The microscopic analysis (SEM and reflected light ore microscopy) showed recrystallization of the pyrite and graphite minerals in the alum shale. The alum shale from the Konows gate area had high graphite content and recrystallized cubic pyrite, while the Slemmestad samples had small amount of pyrite, most in framboidal form. The vein formations of calcite, pyrite and graphite depicted active site of transformation or reactions, as here there is access for the oxygen and water to come in contact with the minerals of the alum shale.

Geochemical simulations showed that the most reactive and at the same time most abundant sulfide mineral in the alum shale when coexisting with calcite a high reaction was demonstrated. The pyrite undergoes both aqueous and electrochemical oxidation. The oxidation of pyrite changed the composition and also property of the rock through time. The change in composition may cause swelling problem due to loss of density, because of formation of gypsum due to oxidation of pyrite, and dissolution of calcite. The minerals calcite and pyrrhotite have an effect on the rate of pyrite oxidation. The calcite caused inhibition on the rate of pyrite oxidation but it was important for the growth of gypsum, and while the mineral pyrrhotite had a catalytic effect on the process of oxidation. Free swelling test showed that there was no expanding clay or smectite in the alum shale sample from the Konows gate and the black shale sample from the Slemmestad.

Contents

Chapter 1 Introduction

1.1 Essence of the study

Lower Paleozoic sedimentary sequence bedrocks in Oslo contain frequent black shale which reacts with oxygenated water and causes a number of problems. The alum shale which is one type of black shale is specifically the focus of this study. One of the problems regarding the alum shale in Oslo region occur when the groundwater level lowers, draining the alum shale and causing considerable swelling. This is thought to be due to oxidation of iron sulfides and formation of gypsum (Moum and Rosenqvist 1959, Ramberg et al. 2006). However, other mechanisms, like the transformation of clay minerals, have also been proposed (Boggs 2006). The swelling characteristic of the alum shale is not fully understood at this time.

This study was done in the Oslo region of Norway. The alum shale samples were taken from the Konows gate area, which is close to the center of Oslo city, and the Slemmestad area on the outskirts of Oslo city. All the samples were alum shales with the exception of one black shale sample, which is not alum shale, which was taken from excavated bedrock of the Slemmestad sewage tunnel while construction of the tunnel was underway.

The alum shale in Oslo contains two iron sulfide minerals, pyrite (FeS_2) and pyrrhotite ($Fe_{1-x}S$) which are responsible for the oxidation reactions. The oxidation of the iron sulfides is a complex processes which undergoes both electrochemical and aqueous oxidation of the minerals. The aqueous oxidation takes place with the presence of oxygenated water and the electrochemical reaction is due to the transfer of electrons between the positively and negatively arranged structures of the minerals existing in the shale. Rimstidt and Vaughan (Rimstidt and Vaughan 2003) showed that the process of the electrochemical oxidation was clearly active under pyrite oxidation but the situation regarding the aqueous oxidation was less clear.

The main source of oxygenated water for the aqueous oxidation is the groundwater that leaks through the rocks and soil moisture in the pore space. Soil and oxygen

depleted water containing ferrous sulfate has been shown to cause considerable deterioration of buildings foundation in only a very few months (Moum and Rosenqvist 1959). Since the alum shale is interbedded with limestone and other calcite mineral sources, the oxidation output of ferrous sulfate reacts with calcite to form gypsum and results in a swelling of the sediment due to reduction in density. The gypsum growth was reported by Hagelia (Hagelia et al. 2003) as a possible reason for the swelling of the shales. However, it does not explain in detail the growth in time and factors which affect amount of formation in alum shale such as the concentration of reacting minerals and elements.

The first step in this study is to determine the mineralogical and chemical composition of the alum shale, and identify the reactive minerals coexisting in the alum shale of Oslo region. The mineralogical analysis was done to identify the minerals composition and their proportion in the alum shale, and the chemical analysis was carried out to determine the alum shale composition based on the chemical elements in it. The analysis was performed using X-ray Diffraction (XRD), X-ray Fluorescence (XRF), Petrographic Microscope, Scanning Electron Microscope (SEM) and chemical analysis of the sulfide species in the alum shale.

The main goal of this research is to identify the possible reasons for the reactivity of the alum shale, which may explain the swelling of the sediment. The pyrite is one of the most abundant mineral in the alum shale of Oslo; pyrite is not so reactive when it exists alone. However, the existence of combined pyrite and pyrrhotite in the alum shale makes it very reactive (Moum and Rosenqvist 1959). Other minerals may also interact in this process and enhance or hinder the reactivity. The rate of pyrite oxidation were also variable among samples of different sources, although surface area difference may exert a great control and needs for further study (Rimstidt and Vaughan 2003). To explore the reactivity of pyrite in alum shale interaction to other coexisting minerals, I have simulated the rate of pyrite oxidation with geochemical code PHREEQC. PHREEQC is a computer program for speciation, batch-reaction, one-dimensional transport, and inverse geochemical calculation (Parkhurst and Appelo 1999). It was simulated based on the level of pyrite in the Konows gate area to see the change in the chemical composition of the alum shale, the effect of other

minerals which exist together in the alum shale like the calcite and pyrrhotite, and to have rough idea of the time scale of the process rate expressions and parameters proposal by Williamson and Rimstidt were applied (Williamson and Rimstidt 1994) were applied.

1.2 Objectives of the research

To summarize:

The general objective of this research was to study the reactivity of the alum shale and to identify the reasons of its swelling characteristics.

The specific objectives were the following

- To characterize the mineralogical and chemical composition of the black shale samples using different analytical techniques (such as XRD, XRF, SEM and Petrographic microscope) and compare the results with evidence from the field
- Model the rate of pyrite oxidation and determine the effect of other reactive minerals coexisting with pyrite in the black shale

1.3 Research sites

Two sampling sites were selected for this study. The first one is in the center of Oslo city in the Konows gate area (263585, 6648060; UTM WG84 zone 33) is located just north of the Ekeberg fault. The sampling site was previously the basement for an old building, but at the time of sampling the basement of a new building was under construction. The second sampling location was in the Slemmestad area (247000, 6635600; UTM WG84 zone 33), 20 Km south for Oslo. New buildings have been constructed in the area.

The sites are depicted in the geological map below from Norwegian geological survey web site (http://www.ngu.no/).

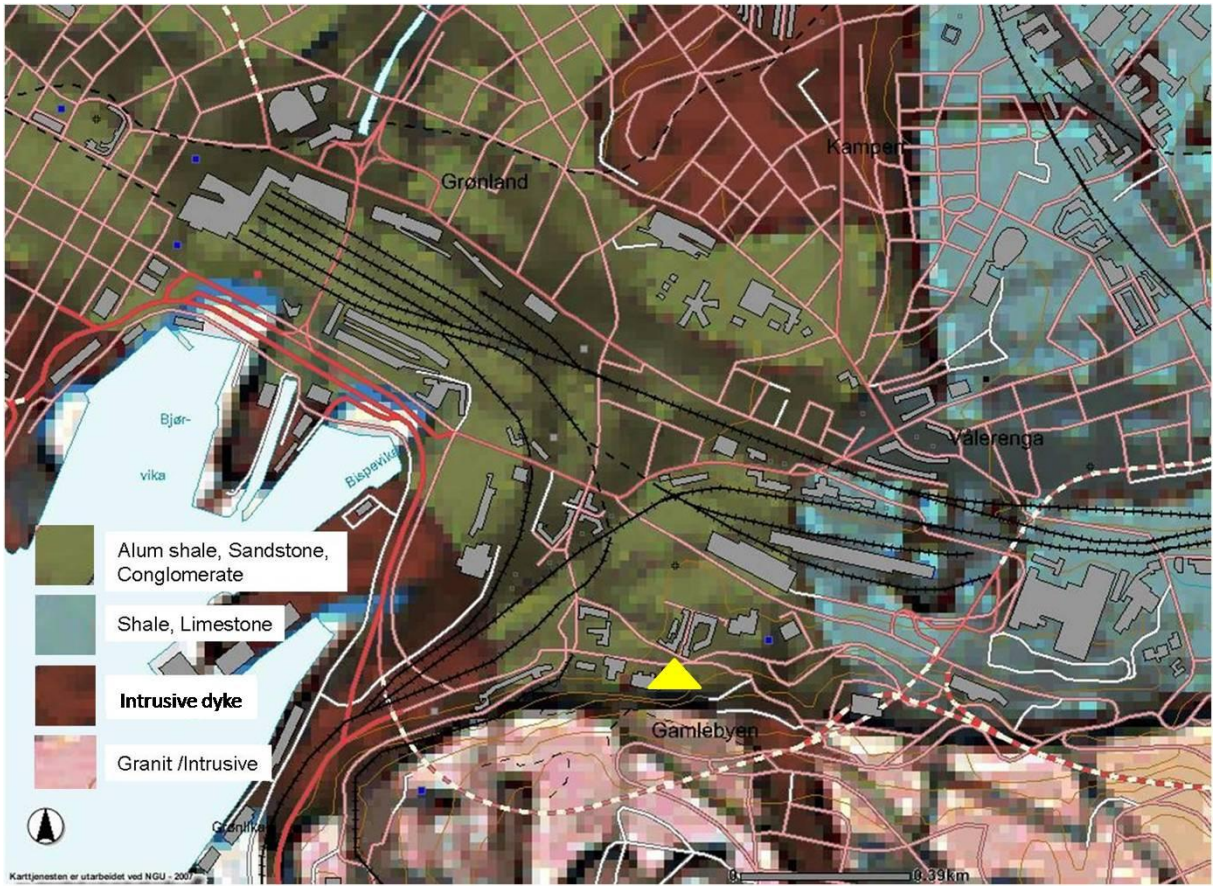

Figure 1-1 Location of the Konows gate sampling site in yellow dot and the background in dark green is the alum shale deposit

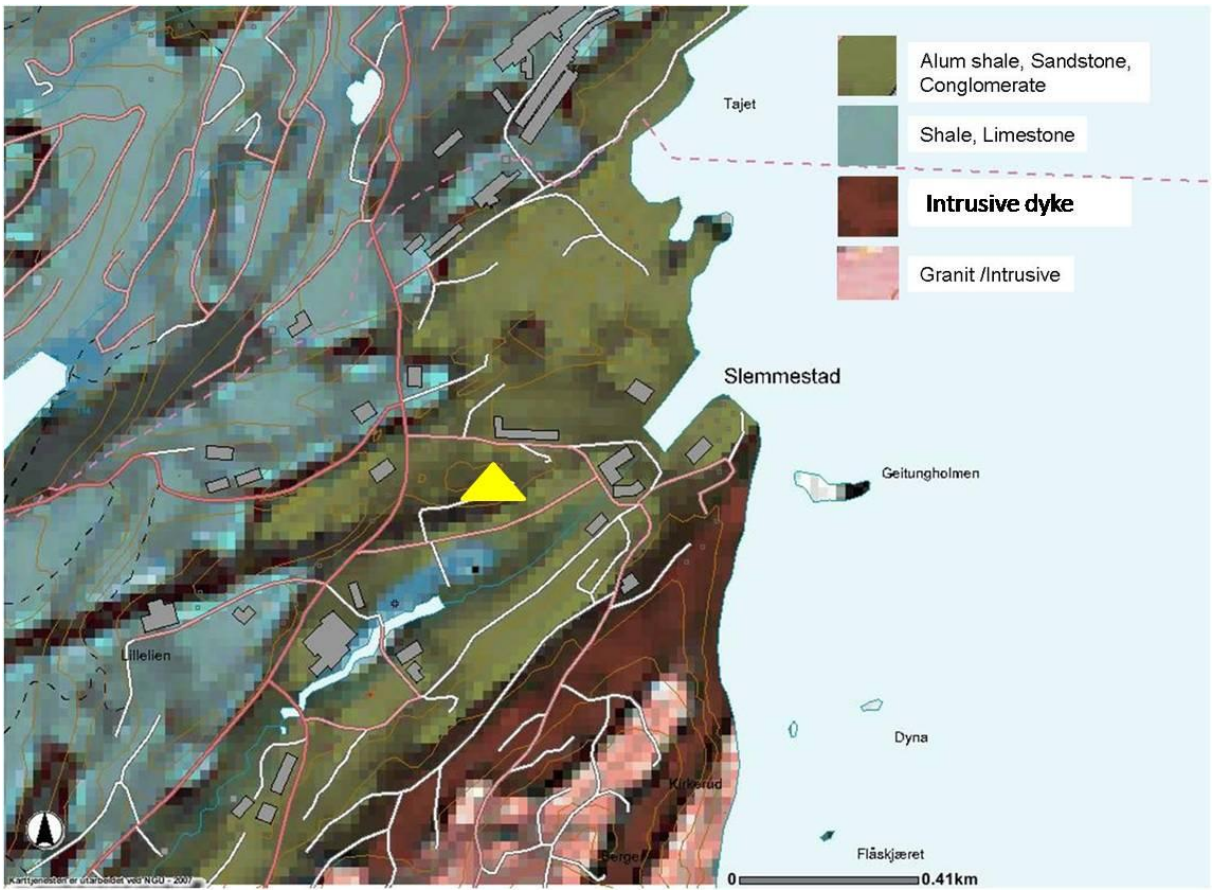

Figure 1-2 Location of the Slemmestad sampling site in yellow dot and the background in dark green color is the alum shale deposit

1.4 Geology of the study area

Sedimentary rocks of Oslo region from lower Paleozoic were deposited within an epicontinental sea, shallow water carbonate ramp or platform and in a foreland basin. One of the four basin fills in the lower Paleozoic is a basin with low sedimentation rate of the typical epicontinental sea, from Cambrian to Middle Ordovician (Larsen and Olaussen 2005) includes the alum shale, a type of black shale, of Oslo region.

The alum shale in Oslo region is a sedimentary rock slightly to moderately metamorphosed (Moum and Rosenqvist 1959). It is around 50 m thick in the Oslo center, Oslo kretsfengsel, Tøyen and along Ekebergskrenten (Ramberg et al. 2006). Field and microscopic observations of foliaceous structures from the Konows gate and Slemmestad areas showed the alum shale went through tectonic movement.

The time of the Oslo rift formation may be the peak movement of the alum shale. The Konows gate area is a transition between the intrusive rock and the alum shale. The alum shale is tilted 40 degrees west at the on site measurement.

Chapter 2 Literature review

2.1 Black and Alum Shale formation

Shales are composed primarily of clay minerals and fine sized quartz and feldspars. They may also contain carbonate minerals (calcite, dolomite, and siderite), sulfides (pyrite, marcasite), iron oxides (goethite), and heavy minerals, as well as small amounts of organic carbon. Many factors including tectonic settings and provenance (source), depositional environment, grain size, and burial diagenesis (Boggs 2006) affect the composition of shales. Formation of black shales requires high organic productivity so that early digenetic reactions do not consume all organic matter, but leads to residual organic carbon in the sediments.

The term “alum shale” originated from the fact that this rock type in Scandinavia was used for manufacturing potassium aluminum sulfate ($KAl(SO_4)_2.12H_2O$) (Moum and Rosenqvist 1959). The alum shale is a type of black shale with high organic matter contents. At field level the alum shale distinguish from the black shale by scratching the shale with knife or other equipment. The scratch line is dark in color if it is alum shale and white if it is black shale. In this study, all the discussion about the alum shale applies for the black shale.

Most works now appear to agree that large iron formations were deposited in continental shelf to upper slope marine environments (Boggs 2006). The middle Cambrian-lower Ordovician shale were deposited on a continental shelf which is the site for the deposition of iron in a reduced environment with little or no oxygen. Moreover, with the presence of organic materials, it is the site for the formation of the Alum shale in Oslo. The origin of the iron is believed to be a continental source and the sulfur is from sulfate reduction from sea water by the action of microbials.

The alum shale in Oslo consists of anthracitic carbon, quartz, feldspar, clay mineral chlorite, calcite as well as sulfides and has swelling properties which is partly due to the growth of gypsum (Hagelia et al. 2003). Bastianen summarized in a three year study that the alum shales in Oslo have pyrite together with reactive pyrrhotite (Bastiansen et al. 1957). These reactive sulfides are able to catalyze other minerals reaction in the sediment causing a swelling and uplifting of buildings in Oslo, e.g. at the geological museum at Tøyen.

In the Oslo local area, the carbonate content of the alum shale sediment is 10 to 15%, and in the extreme cases it is up to 40%, and iron sulfide minerals of pyrite and pyrrhotite are also contained in the sediment. Sulfur content of the sediment is from 5 up to 7% (Bastiansen et al. 1957, Moum and Rosenqvist 1959, Larsen and Olaussen 2005, Ramberg et al. 2006).

2.2 Sulfide minerals

Pyrrhotite ($Fe_{1-x}S$), a non-stoichiometric compound of iron sulfide where x varies from 0 (FeS) to 0.125 (Fe_7S_8), is often associated with pyrite (Fe_2S) in sulfide ores and waste products (Belzile et al. 2004). Microscopic investigation of unweathered alum shale in Oslo contains pyrrhotite in minute grains often indirectly in contact with pyrite (Moum and Rosenqvist 1959). The non-stoichiometry is due to a system of ordered vacancies within the Fe lattice (Vaughan and Craig 1978, Pofsai and Dodonay 1990, Thomas et al. 2000, Thomas et al. 2001). The iron content ranges between 46.5 and 46.8% in Fe (on a mole basis) in monoclinic pyrrhotite and between 47.4 and 48.3% in hexagonal forms (Ward 1970).

The pyrite appears as euhedral and framboidal forms. The euhedral forms are cube and pentagonal dodecahedron which are the most common ones. Other common forms are the octahedron and the diploid. The framboidal form is low grade pyretic material dispersed heterogeneously through out the host rock as either massive or granular material. The massive framboidal pyrite consists of small grains ranging in size from 2 to 5 µm in diameter. These grains tend to agglomerate in spheres of between 10 and 30 µm diameter. Disseminated pyrite is seldom visible to the naked

eye because of its low occurrence and minute size. Its morphology is framboidal, with grain size of 1- 5 µm diameter and an agglomerate size of 5 – 25 µm diameters. Primary massive pyrite consists of crystalline masses, commonly in the range 150 – 600 µm diameter, encapsulated by the ground mass. The above information in this paragraph is taken from Lowson (1982) since the pyrite in the alum shale of Oslo has the morphology and the size elucidated by the above statements. The different forms of pyrite in the alum shale of Oslo are described in section 4.1.4.

The pyrite was found to be the most abundant and undergoes oxidation reaction in the alum shale of Oslo. Its reactivity plays the central role in the reactivity of the alum shale.

2.3 Chemical reaction in alum shale

Because the alum shale in Oslo often is embedded with calcium carbonate bearing rocks, the oxidation of the iron sulfides together with calcite mineral leads to the development of gypsum. Gypsum has a lower density and causes the expansion of the shale, with differential heavily disruption of the floor and wall of the buildings; as Hagelia suggests was the reason for the swelling of the alum shale in Oslo region (Hagelia et al. 2003). Also the oxidation of pyrite produces ferric sulfate, and if not drained jarosite will precipitates, resulting in an increase in material volume, which can cause disastrous results under structures built on pyretic shale (Lowson 1982). Ironically enough, the geological museum in Oslo which is located on top of alum shale, has a crack on the basement floor (Hagelia et al. 2003, Ramberg et al. 2006). If the expansion of the alum shale is due to the chemical change in the alum shale, the oxidation of the iron sulfides is playing the main role in the reactivity of the rock.

Pyrite and pyrrhotite were both undergo aqueous and electrochemical oxidation. Rimstidt J.D. and Vaughan D.J. (2003) pointed out that the processes of the electrochemical oxidation had to take place, but chemical aqueous oxidation was less clear. They also mentioned that there were differences in the rate of oxidation for pyrite samples from different sources. This might be partly due to grain size (and hence surface area) differences; further studies at this point are needed. Pyrrhotite is

an unstable form of iron sulfide and undergoes oxidation reaction with the exposure to oxygenated water.

2.3.1 Electrochemical oxidation

Sulfide minerals are semiconductors which undergo electrochemical reaction in nature. The coexistence of pyrite and pyrrhotite may also have higher electric conductivity in a mixture than for the minerals separately (Moum and Rosenqvist 1959). Concrete deterioration in contact with alum shale free from pyrrhotite was not found and the intensity of the reactivity seemed to increase with pyrrhotite content, possibly due to an increase in the conductivity of the mixture. The semi conducting properties of sulfide minerals are dependent upon the precise composition of the particular pyrite sample or even the zone or region of a particular sample (Rimstidt and Vaughan 2003). This gives more particular emphasis on the search for the mechanism of the oxidation reaction specifically to the shale in the Oslo localities. Subtle difference in stoichiometry also influences the electric properties which may in turn significantly affect the reactivity.

2.3.2 Aqueous oxidation of pyrite/pyrrhotite and the oxidation product

Oxygen is the ultimate oxidant of sulfide minerals and the direct oxidant at pH>4. At pH<4, sulfides are oxidized by ferric iron. The overall process of pyrite oxidation has been described by the following reaction steps (Lowson 1982, Rimstidt and Vaughan 2003, Appelo and Postma 2005).

In the beginning there is an oxidation of disulfide is by oxygen to sulfate

$$FeS_2 + 3.5O_2 + H_2O = Fe^{2+} + 2SO_4^{2-} + 2H^+ \quad \textbf{(1)}$$

In the second step Fe^{2+} is oxidized by oxygen to Fe^{3+}

$$Fe^{2+} + 0.25O_2 + H^+ = Fe^{3+} + 0.5H_2O \quad \textbf{(2)}$$

The oxidation of monosulfide minerals (e.g., sphalerite, galena) requires as many as eight electron transfer, and disulfides (e.g., pyrite and marcasite) require seven electron transfers to release sulfate ions. Incomplete pyrite oxidation, due to an

insufficient supply of electron acceptors results in a solution enriched in Fe^{2+} and SO_4^{2-}. Unless the pH is extremely low, Fe^{3+} will precipitate as goethite according to the following reaction which produces three quarters of the acidity of the overall processes (Appelo and Postma 2005).

$$Fe^{3+} + 3H_2O = Fe(OH)_3 + 3H^+ \quad \textbf{(3)}$$

The predominant oxidation products of pyrrhotite are: goethite, elemental sulfur, as well as small amounts of ferric sulfate and various sulpho-oxyanioins (Steger and Desjardins 1978). There is evidence from field and laboratory studies that the oxidation may not be complete and instead generates elemental sulfur according to the following acid consuming reaction.

$$Fe_{1-x}S + 0.5(1-x)O_2 + 2(1-x)H^+ = (1-x)Fe^{2+} + S^0 + (1-x)H_2O \quad \textbf{(4)}$$

Kinetics of pyrite oxidation

At the higher pH, pyrite oxidation by oxygen is dominant because of Fe^{3+} is inhibited by the low solubility of Fe $(OH)_3$ which keeps the Fe^{3+} concentration very low. The process is slow. The specific rate of the reaction is given by Williams and Rimstidt (1994); see section 3.6.1 in the input data description for the simulation of pyrite oxidation rate using PHREEQC.

The overall rate of pyrite oxidation is also dependent on the initial concentration of pyrite and the concentration at a given period of time, and the surface area of the pyrite. The rate is also dependent on the solution composition, like pH, the distance from equilibrium, and the effect of the catalysis and inhibition (Aagaard and Helgeson 1982). The presences of calcite, pyrrhotite and the level of oxygen and water have significant influence in the rate of oxidation of pyrite in the alum shale of the Oslo region. In order to observe the reactivity and swelling behavior of the alum shale in the Oslo region, it is also very important to know the rough time scale of weathering (oxidation changes in the shale).

Chapter 3 Methodology

The research methodology employed in the study presented in this thesis has three major sections: sampling, mineralogical and chemical analysis of the samples and simulation of the rate of pyrite oxidation in equilibrium with other reactive minerals existing in the alum shale. The sampling consists of collecting of the alum shales from the field and characterizing the site. Identification of the minerals and the elemental compositions of the shales were performed in the mineralogical and chemical analyses part. The analysis employed XRD, XRF, SEM, Petrographic Microscope, and chemical analysis of sulfides. After analysis of the mineralogical and chemical composition of the shales, modeling of the chemical reactions in the shales was undertaken using PHREEQC software. Each section is described as follows.

3.1 Sampling

The samples from Konows gate were taken while construction of a building was under way. It was a proper time to collect unexposed sample without cost of digging. The new construction was taking place on the alum shale as foundation of the building. The site was a foundation of an old building too. Since the alum shale deposit in the area is up to 50m thick, it is not possible to avoid the deposit from the foundations even if it has a problem of swelling. Three representative shale samples from depth of around three to four meter were taken from the Konows gate area.

In the Slemmestad area sampling was done with the help of a loader truck to remove weathered alum shale from the top surface. Three alum shale samples which were less exposed after removing the top layer by the truck were taken. A building in contact with the alum shale sampled site was observed with reddish brown color (see Figure 3-1).

In the Slemmestad area a black shale samples excavated out from constructed sewage tunnel (see Figure 3-2 and 3-3) were also taken and analyzed since the black shale which is not the alum shale also has same problem described in the above section like the alum shale. The black shale placed on an embankment of the

sea was fractured into small pieces. The one which is away from the sea was not fracture into pieces.

Figure 3-1 A building in contact with the alum shale of the Slemmestad area from which samples were taken

Figure 3-2 Slemmestad Black shale rock placed on an embankment of the sea, were fractured into small pieces

Figure3-3The Slemmestad black shale, which was placed away from the embankment of the sea with out disintegration

3.2 Mineralogical and Chemical analysis

3.2.1 X-ray diffraction (XRD) techniques

Each mineral has a unique diffraction pattern while interacting with X-rays. This characteristic of the diffraction is used as identification of the minerals by comparing with diffraction against a database maintained by the international center for diffraction data (http://www.icdd.com).

The X-ray powder diffraction patterns from the samples were used to identify the different minerals in the alum and black shale samples by comparing with the database in analytical software which has same database as the international center for diffraction data. In the following sections, the XRD settings and preparation of the samples for the XRD will described briefly.

XRD equipment and settings

A Philips X'Pert MPD X-ray diffractometer coupled with high score analytical software was used in analyzing the samples. The radiation was Cu K alpha with wavelength 1.54 Å generated by voltage of 40 kv and filament current of 50 mA.

The data collected with an angle of rotation starts from 2 degree to 50 degree 2 theta angles with step size of 0.06 and frequency of one which measured every 3 second of the ray reflected from the sample which is the counting time step.

Sample preparation for XRD

The rock sample first crushed into powder form using cadmium jaw crusher for two minutes. The powder sample of 2 g has placed in the aluminum plate with a rectangular box holding place for the 2 g sample, and compacted well using a mechanical device before it was used for analysis in the X-ray diffractometer.

3.2.2 X-ray Fluorescence (XRF)

The XRF is used to determine the elemental composition of the shale samples. It is based on analysis of secondary X-ray emission from the sample after illuminated by high energy X-ray. The emitted secondary X-ray is detected, processed and recorded when a sample interacts with the primary X-ray beam from the source. The atoms converted into ions, which are unstable, and emit secondary radiation (fluorescence) at wavelengths characteristics of each element present. Each element in the sample emitted unique wavelengths and intensity of emitted energy. The detector converts x-ray photon energy into electric pulses that provide a measure of elements concentration. The chemical compositions were calibrated based on standards with known proportions of particular elements.

XRF instrument and settings

A Philips PW 2400 spectrometer was used to measure concentration of major and trace elements of the samples. Sample changer PW2510 was applied in the analysis. The current and the voltage optimized for each element. The standards curves were tested with known concentrations of samples: SGR-1, AWI-1, and NIM-G 200 standards for the major elements curve test. SGR-1 and SDC-1 standards were used for the trace elements.

Sample preparation technique

The samples were prepared as fused glass disks for the major elements spectrometry analysis and pressed pellets for the trace elements spectrometry analysis. The preparations of the samples are described in the following subsections.

Major elements

1g of crushed rock samples placed in a ceramic container, heated at 110 ^{0}C for half an hour to remove moisture, and weighted to reduce the moisture loss. The sample heated again for one hour at 1100 ^{0}C to calculate the ignition loss. The heated sample mixed with spectroflux ($Li_2B_4O_7$) in a 0.45:4.072 ratio in gram measured at an

accuracy of 0.0001. The mixture melted at 1350 ^{0}C and made as fused glass disk using Philips Per' X3 machine.

Trace elements

10 g crushed sample with less than 100 µm diameter mixed with 2 ml paraloid liquid to bind the grains. The mixture compressed into pelle using a mechanical device that applies a weight of 20 tones. The pellets were heated for about half an hour at 80 ^{0}C to harden them before analysis in the spectrometer.

3.2.3 Petrography and Scanning Electron Microscopy (SEM)

Since only small sections of the samples, which aren't representative of the whole shale are possible to see under the microscopes, the microscopic analysis were used to have qualitative and semi-quantitative information which was employed to compare the minerals abundance between the samples of the two different areas in the Oslo region. The microscopic study was aimed to get information on minerals found in a small concentration which aren't detected by the XRD, environment of their formation and distributions of the minerals in the shales.

Petrographic microscopy

It is the identification of the minerals in the samples based on their optical property (reaction with the transmitted and reflected light) with the aid of polarized light (Nesse 2004). Reflected light microscopy was used to differentiate the various minerals in the shale samples.

Scanning electron microscopy

It is the interaction of the primary electrons beam with the sample which produces various forms of radiations like secondary electrons, characteristics X-rays, auger electrons, backscatter electrons and background X-ray (Steinmetz 1984). So that the elemental composition of the minerals analyzed from the secondary electrons (SEM micrograph) and the characteristic X-rays (EDX spectrum) detected by the secondary electron detector mounted in the SEM sample chamber and processed by the

electronics console into the familiar SEM image and the X-ray detector mounted adjacent to the secondary electron detector for the elemental analysis of the sample.

JEOL JSM 840 electron microscope was used in this study. Each element in the sample produces X-rays with characteristic energies and wavelengths which can be analyzed using an energy sensitive Si (Li) detector in an energy dispersive system (EDX) or by dispersing the X-rays according to wavelength using the crystal detector of a wavelength dispersive system (WDX). In this study the WDX used to quantitative analyses.

Samples preparation

Since the samples were very large, they were first cut into smaller size using a mechanical saw and covered with epoxy to avoid further breaking into small pieces and exposure to oxygen and water. Cross section of representative of the samples, covered with epoxy were cut again into a standard sizes of 3x4x2 cm and sent for preparation of polished section to geological museum in Oslo, where preparation of polished section were done by skilled technician. Polished section of the samples cross sections mounted in an epoxy plug were prepared and used for the petrographic and SEM analysis. For the petrographic analysis the polished section mounted plug was directly used to see through the microscope but for the SEM analysis the polished section surface coated with carbon using evaporative-coater. The purpose of the coating was to obtain clear image of an insulating samples (Steinmetz 1984). The coating was so thin to hinder the identification of the minerals.

3.2.4 Chemical method of Sulfur analysis

The method employed was taken from the Norwegian Geotechnical Institute internal report 25464 (Bastiansen et al. 1957). It was capable of quantifying different sulfide species from the samples. It is possible to have the total sulfur concentration in the XRF analysis (the XRF analysis is dependent on the calibration standard used to quantify the compositions), feasible to undertake semi-quantitative mineralogical analysis using XRD, and also SEM used to identify the different sulfide species unfortunately these procedures tend to be less accurate for quantitative

determination compared to the chemical techniques which are liable to be simpler and provides more accurate data. However, currently there is no suitable procedure exists in determining the sulfides directly using the chemical techniques. It is determined indirectly from the difference between the total sulfur and acid soluble sulfur. It may over estimate the pyretic sulfur due to the presence of monosulfides (pyrrhotite, mackinawite), acid insoluble metal sulfates (barite, celestite), organic and elemental sulfur (Czerewko et al. 2003).

Sample preparation

A sample of minimum 500 grams is crushed to size 0-10mm three times in jaw crusher. Crushed sample is split down to sample size approximately 100 grams. This sample is grounded to fine powder in steel planetary ball for 5 minutes. The sample powder is sieved on 0.5mm sieve to assure complete grinding. Powder sample is stored in containers under vacuum to prevent oxidation of sulfides.

Reactive sulfur (monosulfides)

10 g of the sample powder is placed in a closed glass flask. Hydrochloric acid (1:1) is added, which causes H_2S gas to evolve from monosulfides in the sample. A nitrogen cylinder is connected to the flask and a gentle flow of nitrogen gas transports the H_2S gas through a cooling column into a test tube containing a solution of ammonium cadmium sulfate (NH_3CdSO_4) causing sulfur to precipitate as cadmium sulfide (CdS). CdS is filtered, washed and placed in a beaker. 20ml of 0.1 N iodine solutions is added together with 1ml of concentrated HCl causing a reaction with iodine. Amount of iodine spent in the reaction is determined by titration with 0.1 N sodium thiosulfate solutions. Amount of sulfur in the sample is then calculated.

Total sulfur (monosulfides, disulfides, and sulfates)

The analysis is based on oxidation of all sulfides to sulfate. The sulfate amount is determined by gravimetric analysis with barium chloride. 1 gram of sample is dissolved in 50 ml of an acid mix containing two parts of concentrated nitric acid and one part of concentrated hydrochloric acid. The solution is heated and evaporated to

complete dryness. The acid treatment is repeated with concentrated hydrochloric acid. From this point the analysis is performed like ordinary gravimetric sulfate analysis with precipitation with barium chloride (see in the next section).

Acid soluble sulfate

The analysis is based on gravimetric determination of acid soluble sulfates by precipitation of barium sulfate with barium chloride. 10 grams of sample is dissolved in 100ml of de-ionized water and 10ml of hydrochloric acid. After heating the solution to boiling point the solution is filtered and added barium chloride for precipitation of barium sulfate. After standing overnight the precipitate is filtered in a filter crucible, heated to 600 ^{o}C for one hour and weighted. Weight of $BaSO_3$ is calculated to sulfate content as SO_3.

3.3 Modeling of chemical reaction using PHREEQC

Modeling of chemical reaction in the alum shale was included to investigate the change in chemical composition which further may result in swelling of the alum shale due to increase in volume.

PHREEQC is a useful geochemical model tool, which can simulate reactions between minerals, aqueous solutions and gases. It is advantageous to see the chemical change in the sediments in aqueous, gases, and mineral phases with graphic view and grid data. It is easy to see the effect of minerals in equilibrium phase with the aqueous solution.

The input data for the simulations was taken from mineralogical and chemical analysis of the alum shales from the previous sections of this study. Identification of the reactive minerals was done from the mineralogical analysis and the concentration of the sulfide minerals was calculated from the chemicals analysis. The input data are described in the following section.

3.3.1 Input data

Pore water solution, relative abundance of minerals which are assumed to be in equilibrium with the pore water solution, and amounts of the reactive minerals which undergo the reaction are the input data for the simulation.

Pore water solution

Pore water samples practically from the shale samples were not available, so another water sample from the same area was used instead. The water sample was taken from a leak through a crack in the alum shale, which is in contact with the pore water solution (see table – 3.1). It is probably very similar to unaffected groundwater from behind Åkeberg (very close to the Konows gate), Oslo (Hagelia et al. 2003).

Table 3-1 result of water analyses from Åkeberg, Oslo (concentration in mg/l)

pH	temp(^{o}C)	Ca^{2+}	Na^{+}	K^{+}	Mg^{2+}	Cl^{-}	NO_3^{-}	SO_4^{2-}
7.6	25	615	26	22	110	276	25	1841

High sulfate concentration in the water analyzed (see table 3-1) is due to the pyrite oxidation from the alum shale. High calcium ions were probably due to the calcite dissolution and chlorine from clay minerals.

Kinetic reaction

The solution was reacted with the various minerals identified using the mineralogical analysis, and their level in the alum shale estimated using the chemical analysis of the sample. In gases phase, oxygen is used in equilibrium with the solution in pore water. The oxygen gas was used in two different levels. The first scenario was fixed amount of oxygen added to the simulation and the second scenario was constant supply of oxygen into the simulation.

3.4 Free Swelling Test

In the swelling test, 10 cm3 of air dried and fine-grained (less than 0.02 mm) clay was placed in a 50 cm3 cylinder filled with distilled water. The hight of the settled clayey sediment was then measured from the scale on the cylinder. The clay thus soaked which increased their volume from 10 cm3 to more than 13 cm3 proved to contain smectite when studied by X-ray analysis.

Chapter 4 Result and Discussion

4.1 Mineralogical and Chemical analysis

4.1.1 XRD

Quartz is by far the most common of the silica minerals in sedimentary rocks and its diffraction lines can be used as internal standard for the accurate and precise measurement for the interplanar spacing (d, in Å)(Moore and Reynolds 1989). In the analysis of the XRD diffractogram of all the alum and black shale samples, the high-score spectral analysis software automatically detected the quartz mineral peaks from all the samples. The quartz peaks were found at 4.26Å (20.8, 2ɵ) (35), 3.346Å (26.6, 2 ɵ) (100), 2.46Å (36.5, 2 ɵ), 2.28(39.5, 2 ɵ), 2.24(40.3, 2 ɵ), 2.13Å (42.2, 2 ɵ) and 1.981Å (45.8, 2 ɵ) d spacing (2 ɵ) positions from the Konows gate (KS2) sample (see Figure 4-1).

The next highest peak from the quartz (3.346Å) was the peak at 2.71Å, which is the 85% intensity peak of pyrite. The pyrite peak was also found at 2.425Å d-spacing positions. After sorting out the quartz and pyrite peaks, the next highest peaks were at the 10.042Å d-spacing position, which was identified as the illite 100% intensity peak. The peak at 4.494Å d-spacing position was also the 90% illite peak along with the 10.042Å position. In the same way calcite peaks were found at 3.0344Å (100), 2.282Å and 2.095Å d-spacing positions. Microcline peaks were found at 3.245Å (100) and 4.48Å (60) and 3.83(50) d-spacing positions. The identification of the minerals in the rest of the samples was done in the same manner and the results are presented in Appendix-A with the peaks found in the samples and the identified minerals with their peaks.

Summary of the mineralogical composition of the samples from the XRD analysis is given below in Table 4-1. Quartz is a common mineral in all the samples. Pyrite was found in all the alum shale samples but not in the black shale sample, in which the peak of pyrite wasn't detected by the program. Illite is a common clay mineral in the alum shale of the Konows gate area samples and muscovite is common in all the

Slemmestad samples including the black shale sample. Gypsum was found in all the Slemmestad alum shales but not in the black shale sample.

Samples	KS1	KS2	KS3	SM	SW	SL	BS
Minerals composition	Quartz Pyrite Illite Orthoclase Calcite Glauconite	Quartz Pyrite Illite Calcite Microcline	Quartz Pyrite Illite Orthoclase Glauconite	Quartz Pyrite Muscovite Orthoclase Albite (ordered) Gypsum	Quartz Muscovite Gypsum Pyrite Sanidine	Quartz Muscovite Pyrite Bernalite Microcline Gypsum	Quartz Clinoclore (ferroan) Calcite Albite(Ca-rich, ordered) Ankerite Muscovite

Table 4-1 Mineralogical composition of the samples analyzed using XRD, KS1, KS2, and KS3 are samples from the Konows gate area and SM, SW, SL are alum and BS is black shales from the Slemmestad areas

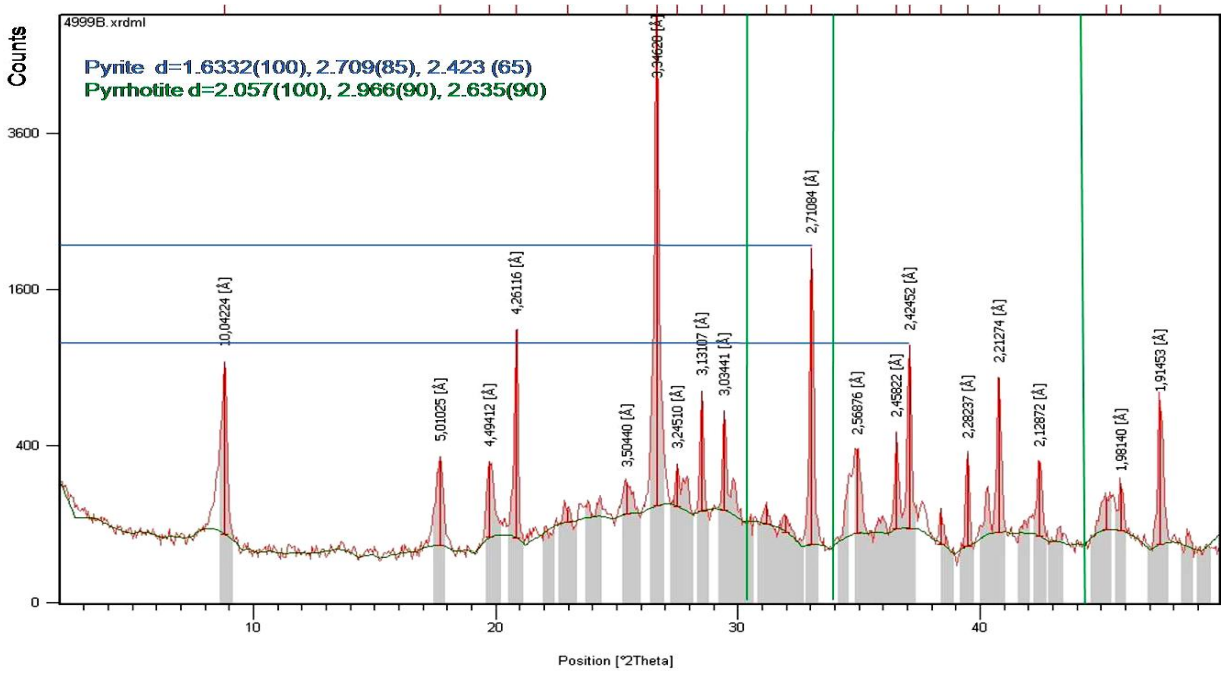

Figure 4-1 Diffractogram of the Konows gate area sample KS2 with the peaks indicated by the blue count lines were from pyrite. The green lines show there were not any pyrrhotite peaks.

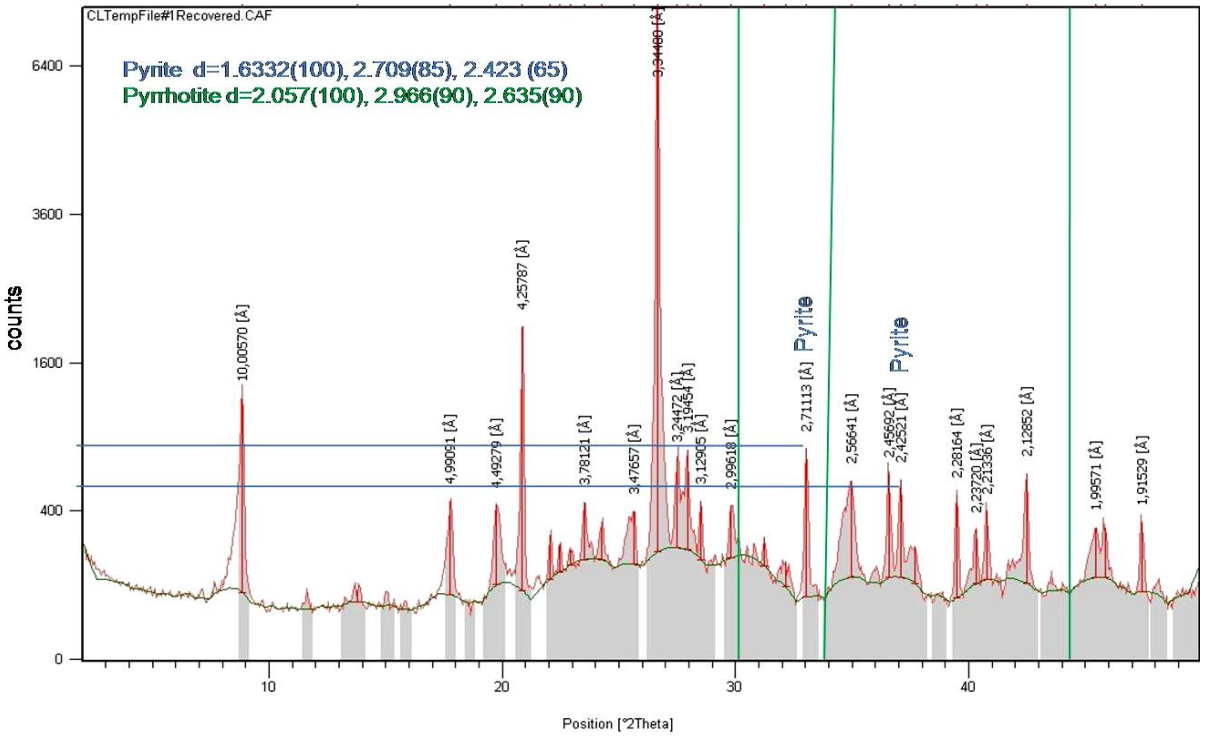

Figure 4-2 Diffractogram of the Slemmestad area sample SL with the blues line drawn to the counts of the pyrite peaks, which is less compared with the Konows gate area. The green lines to show there are not any pyrrhotite peaks. The sample contains quartz, muscovite, bernalit ($Fe(OH)_3$), microcline and gypsum peaks in addition to pyrite

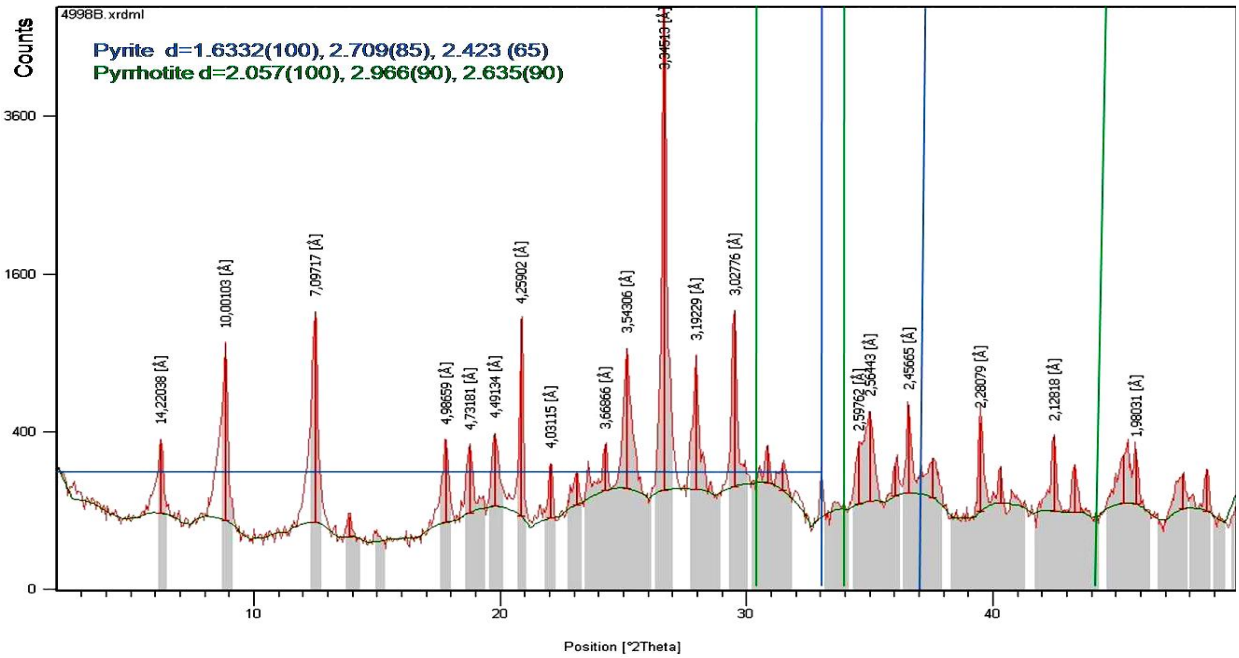

Figure 4-3 Diffractogram of the black shale sample, The blue lines show an undetected peak of pyrite with small concentration. The green lines show the position of the pyrrhotite peaks. The sample

contains quartz, clinoclore (ferroan), calcite, albite (Ca-rich), ankerite and muscovite in addition to pyrite

The X-ray diffraction was used to identify the different minerals in the alum shale and black shale samples. Pyrrhotite exists associated with the pyrite in the shale and has specific diffraction peaks in the X-ray diffractogram. Pyrrhotite has the three strongest diffraction lines at d spacing of 2.057(100), 2.966(90), and 2.635(90), where as pyrite at 1.6332(100), 2.709(85), and 2.423(65) (Roberts et al. 1974). The XRD diffractograms from the samples analyzed in the figures 4-1 to 4-3 have pyrite minerals but not pyrrhotite. It was not possible to find the pyrrhotite minerals peaks in the other samples diffractogram analysis too.

The XRD analysis is semi quantitative based on the fact that the peak height in the diffractogram is proportional to the concentration of the mineral in the sample. The peak height at 2.71 and 2.425Å of the three diffractograms in Figure 4-1, 4-2 and 4-3 compared using the blue horizontal lines to the number of counts depicts the pyrite concentration as highest in the Konows gate area alum shale sample (which is shown in Figure 4-1) compared with the alum shale sample (in Figure 4-2) and the black shale sample (in Figure 4-3) from Slemmestad. There is just amount of pyrite in the black shale of the Slemmestad. This is evident from the sulfur analysis in table 4-3 and the pyrite peak in figure 4-3.

In general, the XRD has limitation on identification of minerals that exists in small amounts like the pyrite in the black shale sample. It is difficult to quantify the concentration of the minerals from their peaks that may be possible, but it is tedious and time consuming. In addition to that it is a bulk method, which does not give the information about grain size, shape and coexistence of minerals. Therefore, microscopic study of the samples to identify minerals in small concentration, grain size and distribution and the depositional environment of the alum and black shales was done in the following sections.

4.1.2 X-Ray Fluorescence (XRF)

All the samples were analyzed for the major and trace elements. The results are presented below in table 4-2 for the major elements and iron in their oxide weight percentage and table 4-3 for the trace elements and total sulfur in part per million (ppm). The most abundant element found was SiO_2, which is almost close to half of the rock samples and the second abundant element is Al_2O_3. The sum of the SiO_2 and Al_2O_3 is almost 60 to 70% of the rock mass. The Fe_2O_3 and S are the third and fourth most abundant elements in the rock respectively.

The results depicted the sulfur content in the first three samples from the Konows gate area, which is in the range of 3.9 to 6.54 % by weight, is twice the Slemmestad alum shale samples, which is 1.9 to 2.8 % by weight. The lowest amount of total sulfur was found in the black shale sample of Slemmestad.

In the same manner the iron content of the Konows gate samples, which ranges from 8.79 to 17.04% is higher than the Slemmestad samples, which was in the range of 3.84 to 6.49%. However, an important difference showed up for the black shale sample. It has the lowest amount of the sulfur and higher amount of iron compared from the surrounding alum shale sample of the Slemmestad area, which is 7.46%. From the result of the XRD analysis of the black shale, it was found ferroan chlorite, ankerite and mica minerals which contain iron.

Another important result was the high loss of ignition (L.O.I.) in the major element determination. The L.O.I. is the sum of the organic matter, inorganic carbon, sulfur and water in crystalline form. If the amount of the sulfur, which is estimated with the trace elements analysis, is subtracted from the ignition loss, the resulting L.O.I. from the Konows gate area is 14.39, 14.24 and 13.83% and the Slemmestad area is 12.2, 10.7, 9.96 and the black shale value is 9.05. The variation of L.O.I. within the samples was probably due to the sulfur variation in the samples. The number represented the organic and inorganic carbons. The total organic carbon in the alum shale of Oslo, example from Krekling is 12% (Bharati et al. 1996) and typically alum

shale has 10 to 12%. Therefore, it is possible to say that the carbon content of the alum shale in the Konows gate area is higher than the Slemmestad area.

Table 4-2 XRF major elements concentration in %wt of their oxides (KS1, KS2 and KS3 are alum shale samples from the Konows gate. SM, SW and SL are alum shale samples and BS is black shale sample from Slemmestad)

Composition	KS1	KS2	KS3	SM	SW	SL	BS
SiO_2	46.15	42.14	53.07	52.01	55.63	56.83	50.18
Al_2O_3	13.2	12	16.05	15.99	17.35	15.47	17.45
Fe_2O_3	12.18	17.04	8.79	6.49	3.84	5.24	7.46
MnO	0.02	0.02	0.02	0.01	0.01	0	0.06
MgO	0.89	0.83	1.09	1.12	1.19	1.13	3.71
CaO	0.98	1.59	0.46	0.24	0.05	0.16	5.4
Na_2O	0.28	0.22	0.34	0.85	0.87	0.83	1.06
K_2O	3.92	3.55	4.72	5.13	5.75	5.2	3.68
TiO_2	0.69	0.64	0.85	0.87	0.97	0.83	0.79
P_2O_5	0.15	0.18	0.23	0.13	0.01	0.13	0.11
L.O.I.	19.83	20.78	17.73	15	12.62	12.17	9.53
SUM	98.29	98.99	103.3	97.85	98.28	97.99	99.42

Table 4-3 XRF trace elements concentration in ppm

Composition	KS1	KS2	KS3	SM	SW	SL	BS
V	676	572	618	1526	1012	1728	168
Cr	108	99	104	167	143	189	265
Co	60	50	81	52	206	50	45
Ni	168	137	147	396	139	221	114
Cu	157	146	184	190	88	175	39
Zn	115	119	163	260	39	123	99
Rb	140	125	160	169	190	162	159
Pb	32	29	35	38	34	30	20
Sr	118	130	59	88	77	83	386
Y	42	38	55	53	32	44	21
Zr	132	116	152	170	180	154	129
Nb	16	15	18	19	21	18	12
Th	13	12	15	17	12	15	10
U	132	91	136	184	51	89	5
Ba	1546	1509	1538	1653	2127	1489	1087
S	54380	65406	39005	27965	19182	22139	4831

The existence of pyrite in high level in the XRD data draws the way to see the ratio of the iron to sulfur in the sample. The result of the iron to sulfur ratio is shown in Figure 4-4 below. The iron to sulfur ratio in the samples are close to 1:2 ratio depicts the dominant sulfur containing mineral in the samples is pyrite except for the black shale sample of the Slemmestad area.

The lowest amount of sulfur was found in the black shale sample of the Slemmestad area. Perhaps the existence of the iron in excess of the 1:2 ratio of iron to sulfur may have good environment for the formation of the pyrrhotite structure in the absence of oxygenated water even if other iron containing minerals existed the iron may have preference to attach with the more reactive sulfur.

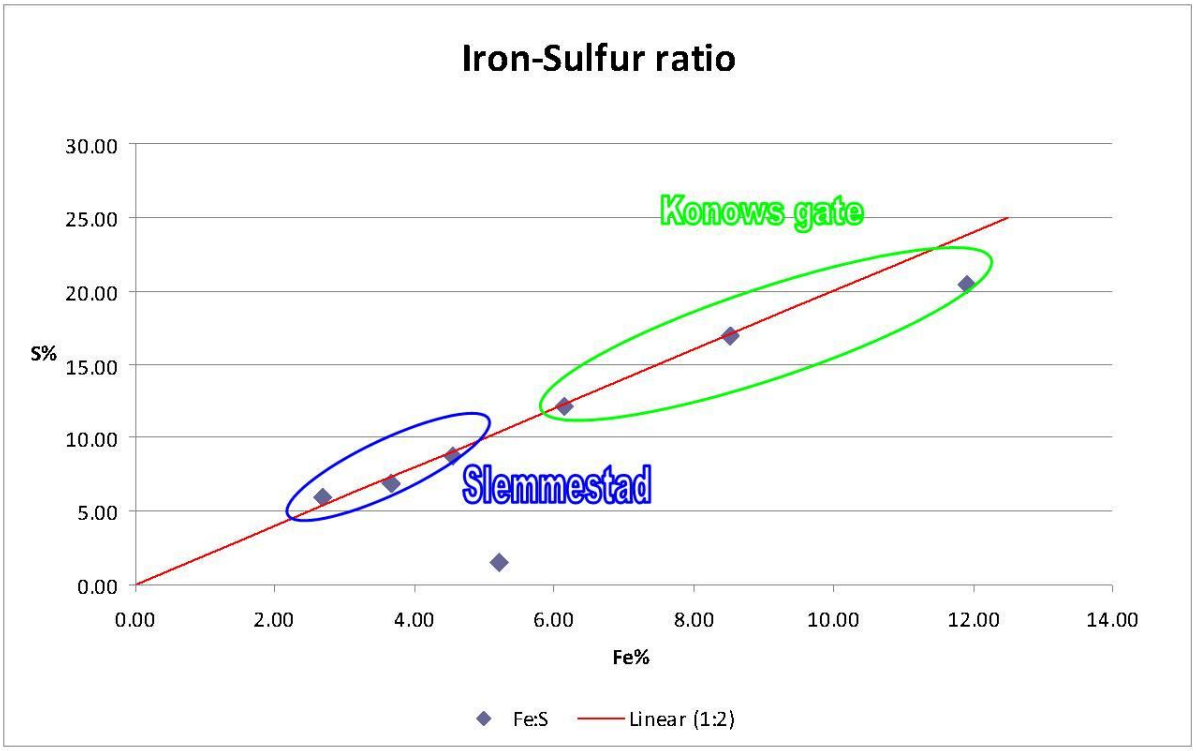

Figure 4-4 the ratio of iron and sulfur in the bulk rock samples is close to 1:2 except the black shale sample, which have other iron containing minerals in atomic%. Sample KS2 has more sulfur above the 1:2 ratio compared with the other alum shale samples

4.1.3 Chemical analysis of sulfide species

Analysis of sulfur on two samples from the Konows gate and one sample from the Slemmestad black shale were done to examine the concentration of monosulfides, total sulfur and acid soluble sulfates in the alum and black shales samples.

The result of the analysis were 0.034 and 0.037% reactive sulfur (monosulfides), 9.62 and 7.62% total sulfur, and 0.035 and 0.027% acid soluble sulfate from sample 1 and 2 of the Konows gate area respectively. The black shale of Slemmestad had less than 0.001% reactive sulfur, 0.85% total sulfur and 0.01% acid soluble sulfate.

The alum shale and black shale have the potential of swelling when the content of reactive sulfur is greater than 0.01% and the total sulfur in the order of 1.5 to 2% and above (Bastiansen et al. 1957). According to the above elucidated criteria the alum shale of the Konows gate area in the central region of Oslo has the potential of swelling and the black shale of the Slemmestad area has negligible potential of swelling.

In this study the result of the chemical analysis technique was used to determine the pyrite concentration more accurately. It is also used as supporting information for the swelling of the shale but it is not the scope of this study to test the limit of the reactive sulfur and the total sulfur to characterize swelling of the shale. However in the simulation model of the rate of the pyrite oxidation with the coexisting minerals such as the calcite and pyrrhotite, since the concentration of the reactive sulfur is close to the limit 0.01% can be tested to see the change in the chemical composition of the shale.

Table 4-4 sulfide species of the Konows gate area samples in wt%

Sample	Monosulfides	Sulfate	Total sulfur
1	0.034	0.035	9.62
2	0.037	0.027	7.29

4.1.4 Petrographic microscopic analysis

The results from the petrographic microscopic investigation are presented in the following ten selected pictures (see Figure 4-5 to 4-14). From the petrographic analysis, it was possible to find additional minerals like chalcopyrite, sphalerite, pyrrhotite, dolomite and graphite which were not detected by the XRD analysis. It was also possible to see their environments of formations and changes in the form of the minerals due to geophysical and chemical processes and other reasons.

Chalcopyrite was identified in the samples of both the Slemmestad and Konows gate areas (see Figure 4-5 and 4-6). It has a brassy yellow color and found associated with the pyrite. Sphalerite was also found in the Slemmestad area samples (see gray color area of Figure 4-5). The sphalerite and chalcopyrite were found as impurities in the middle of recrystallized cubic pyrite.

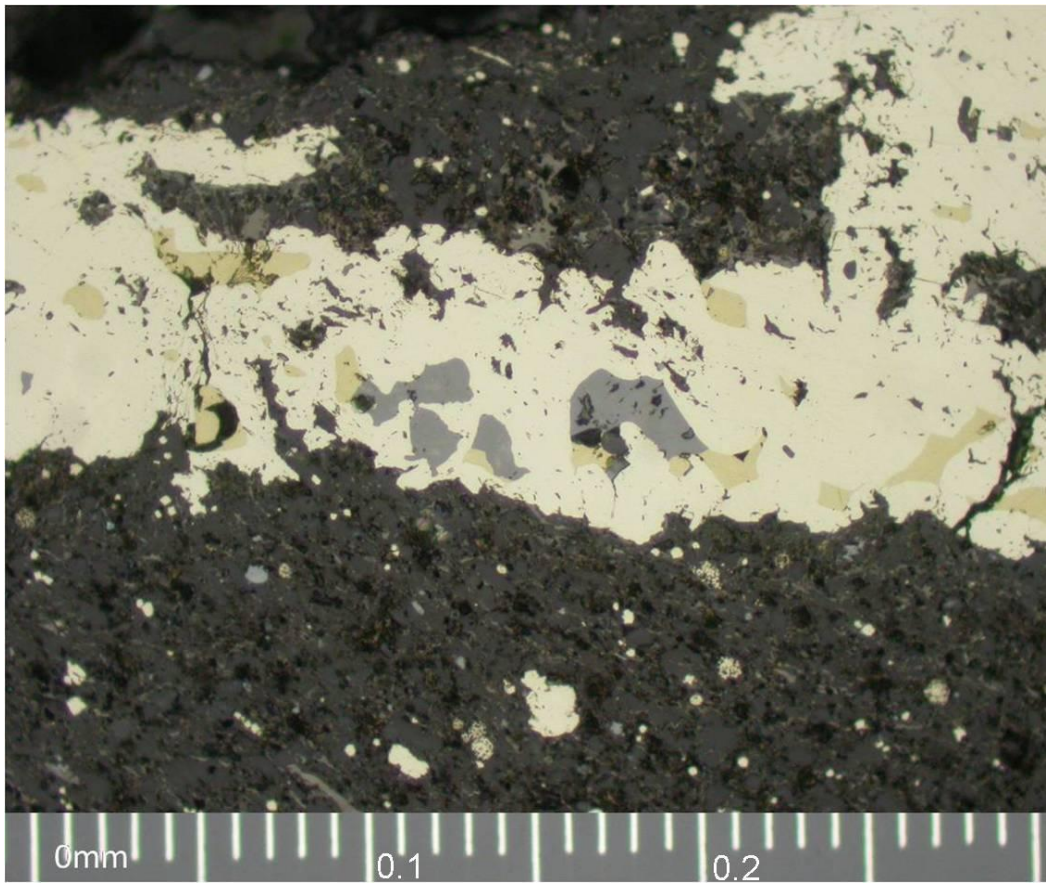

Figure 4-5 Aggregates of pyrite in white, chalcopyrite in brassy yellow and sphalerite in gray in the Slemmestad area, X40 SM

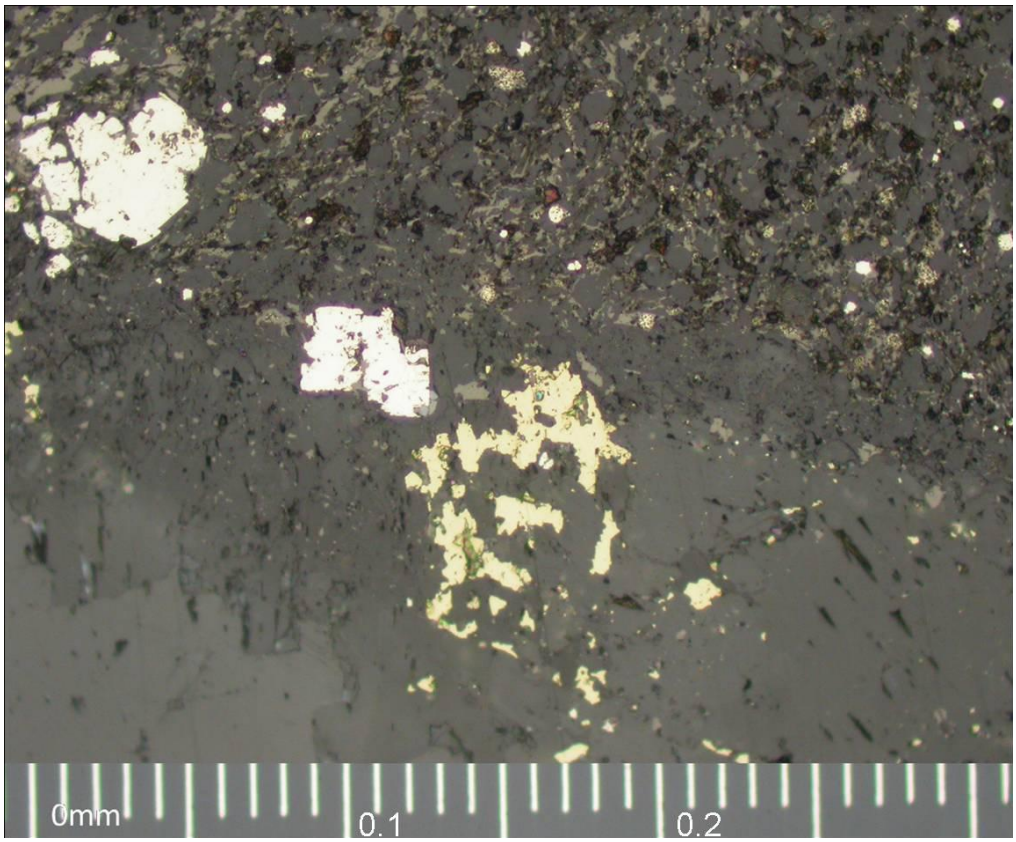

Figure 4-6 Aggregates of chalcopyrite in brassy yellow and pyrite in white in the Konows gate area, X40 KS-1

In polished sections euhedral pyrite is creamy white, isotropic, and sometimes anisotropic and may display pleochroism. It may exhibit zonal growth banding (Lowson 1982). Recrystallization of framboidal pyrite and formation of large cubic pyrite were found in all the samples. The framboidal and cubic pyrites were found in very close to each other in the black shale sample of the Slemmestad area (see Figure 4-7 and 4-8). From shape of the formation, it is possible to say that the framboidal transformed into cubic pyrite. This may be a special property of pyrite, which shifts its structure into more stable form.

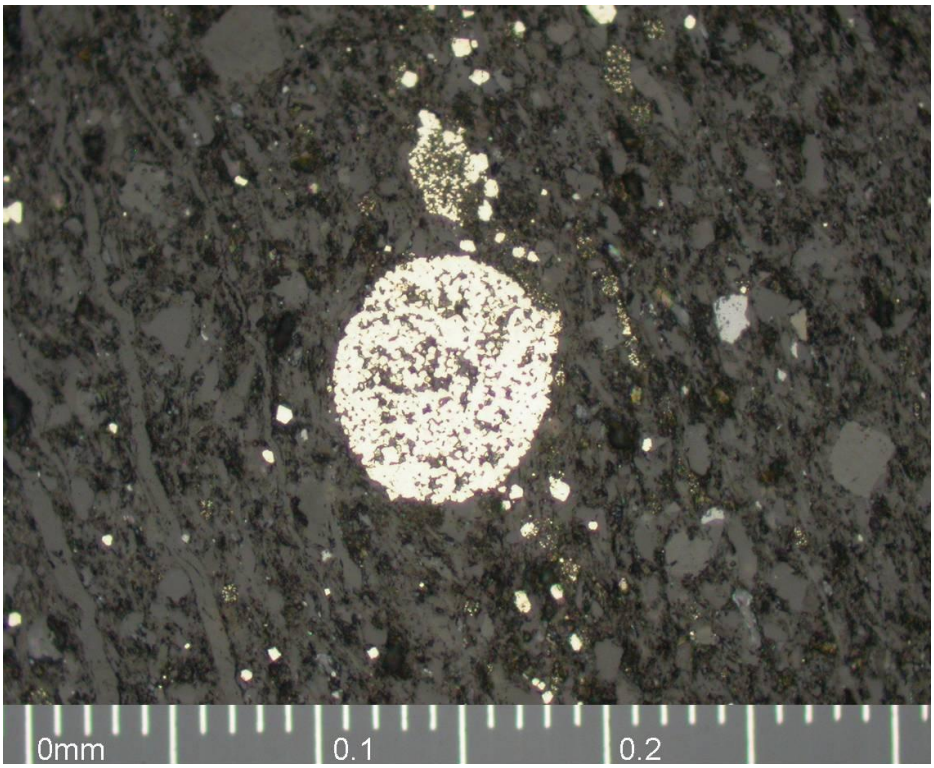

Figure 4-7 Framboidal pyrite aggregate dispersed in the host black shale and formation of the framboidal aggregate. X40 BS

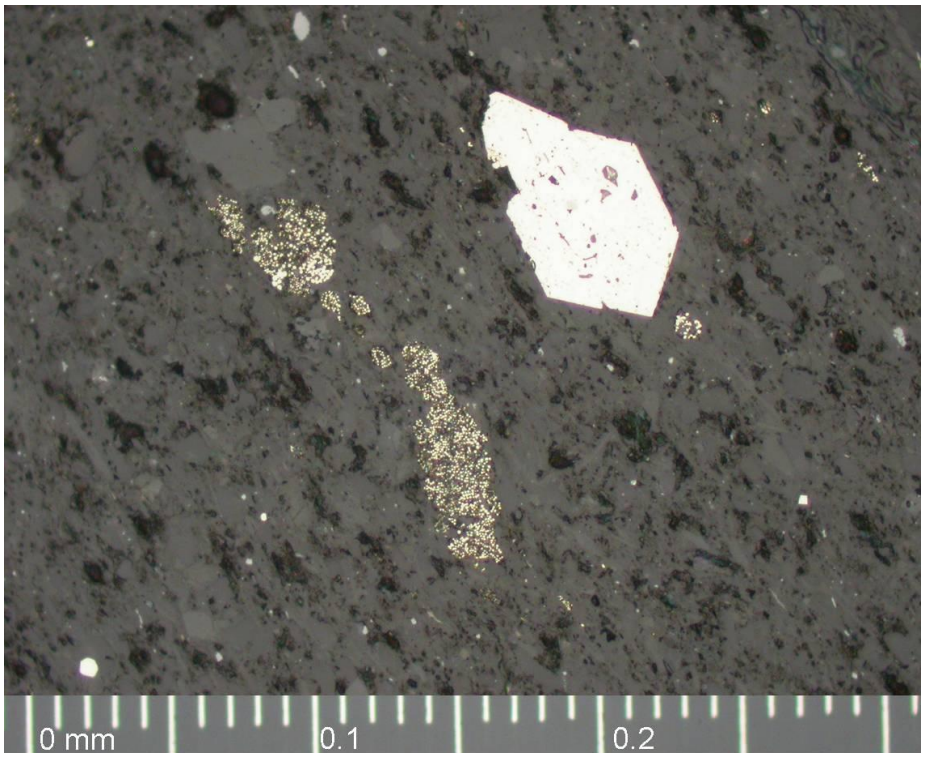

Figure 4-8 Framboidal and euhedral pyrite porphyrorblast, X40 BS

Long veins of pyrite formation (see Figure 4-9) and well tectonized formations which have faults and folds were found in the Slemmestad alum shale. The parallel lines of pyrite or primary sedimentary layers (see Figure 4-10) were observed with little recrystallization and metamorphoses relatively compared with the Konows gate samples (see Figure 4-11). Perhaps it was a formation during the processes of slow sedimentation in the marine environment due to the layering of the sediments. Moreover, most of the pyrites were framboidal with very little graphite in a small trade like shape.

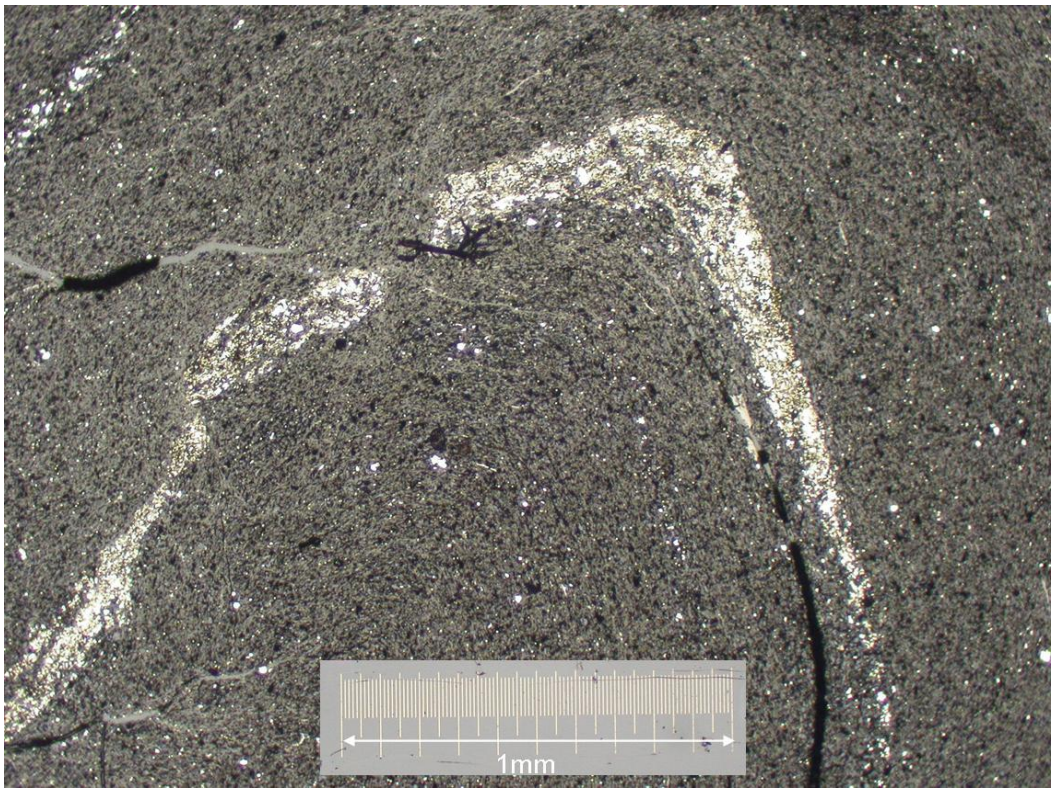

Figure 4-9 Very folded pyrite layer of the alum shale in Slemmestad. X5 SW

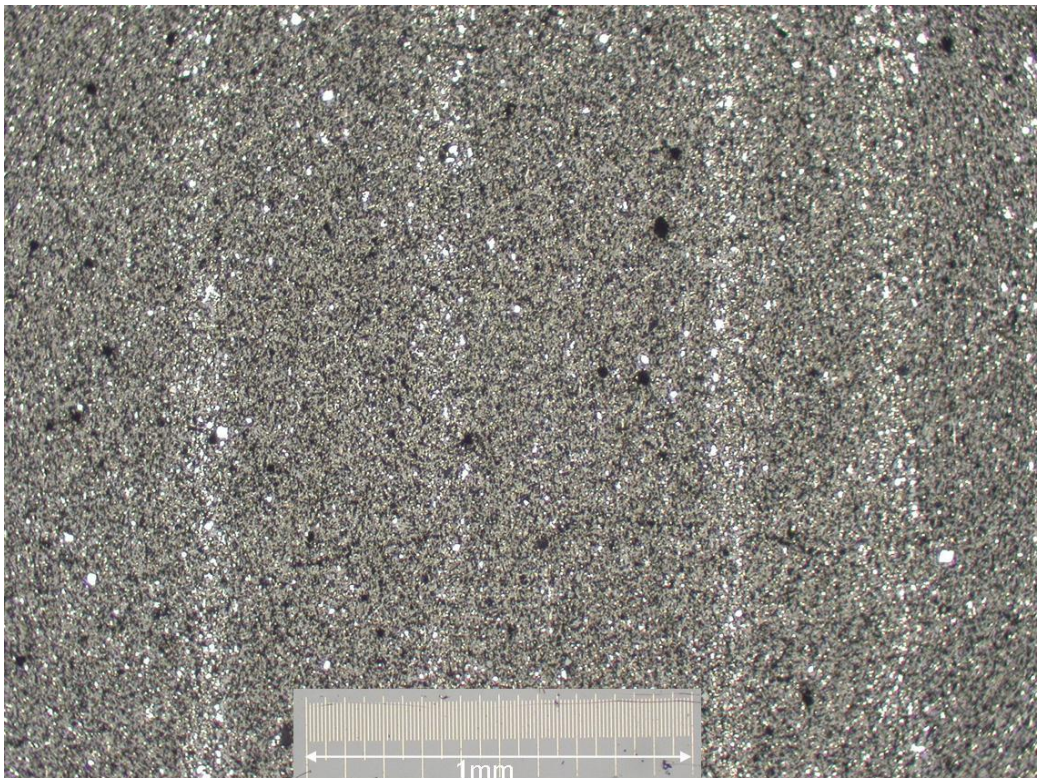

Figure 4-10 the white parallel lines are layering of recrystallized framboidal pyrite from Slemmestad area. X5 SL

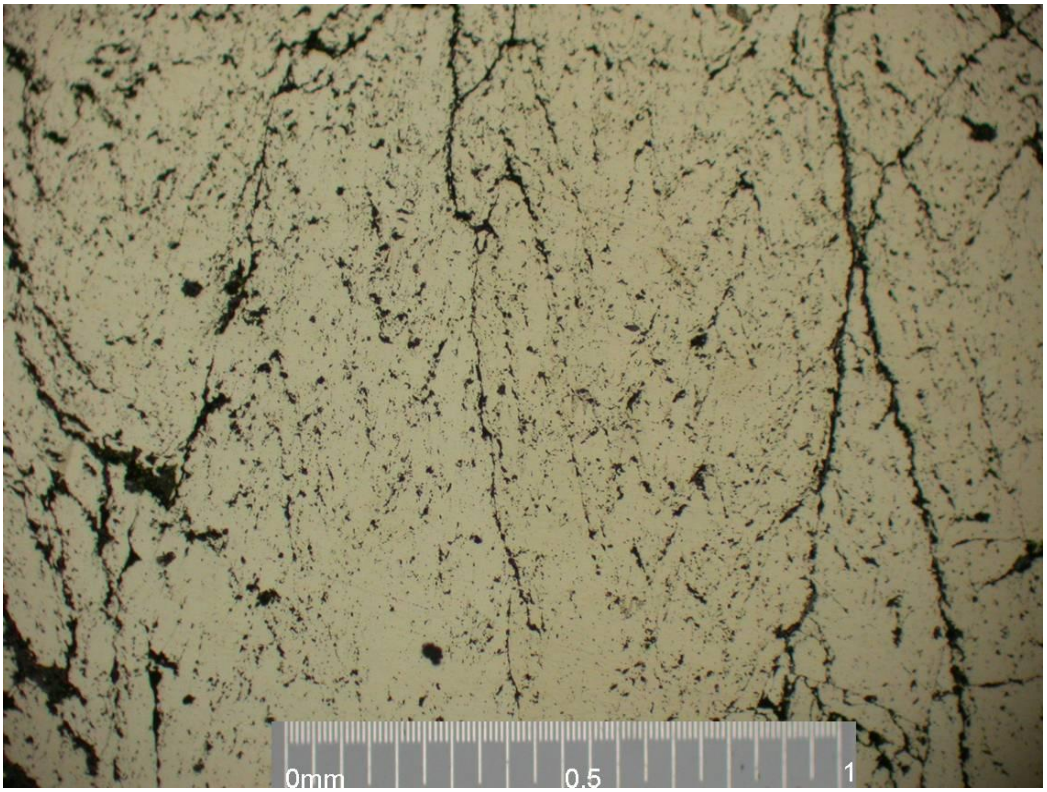

Figure 4-11 Surface of zoned pyrite growth depicted the tectonic movement from the Konows gate area sample. X10 KS2

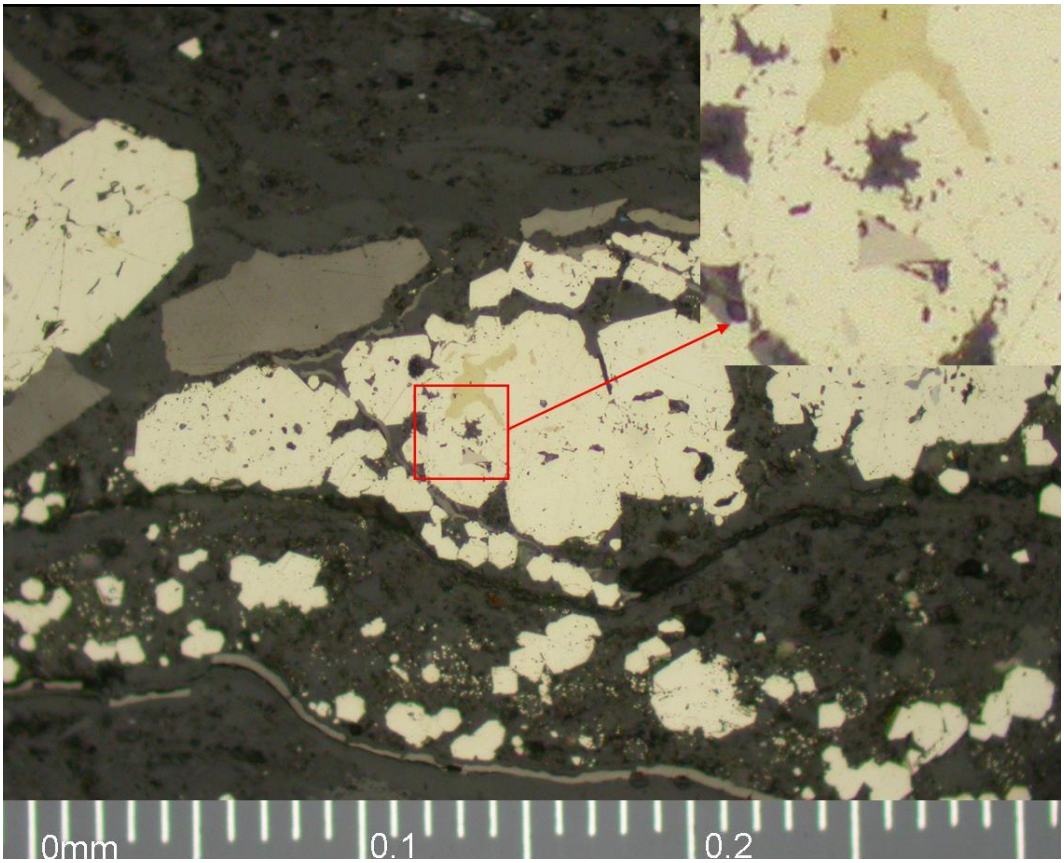

Figure 4-12 Chalcopyrite in brassy yellow, both framboidal and cubic pyrite in white, pyrrhotite (the little white grey which is a bite darker than the pyrite) and recrystallized and broken graphite were shown. X40 BS

Chalcopyrite, graphite and pyrrhotite mineral were found in the black shale of the Slemmestad (see Figure 4-12). The presence of the pyrrhotite in the black shale of Slemmestad may probably due to high content of iron (see the table 4-2 and 4-3, XRF result) and low sulfur content. Even if the iron existed in the other mineral forms, the sulfur may attach with the iron in the excess with lower ratio compared with the 1:2 ratio in the pyrite formation.

Graphite was found in the veins of the samples from the alum shale of the Konows gate area and also in the Slemmestad area. It is due to recrystallization of carbon in the area. Graphite is electrical conductor and may have significant effect on oxidation of pyrite in the rock. It may also depict the temperature of above 200 degree low

metamorphoses of the alum shale. The organic matter in the Oslo area (location Krekling) is graphitic in nature and over-mature (Bharati et al. 1996). More carbon and sulfides in the Konows gate samples were observed compared with the Slemmestad samples (see Figure 4-13 and 4-14). The graphite exists with the pyrite in the veins. Veins of calcite found in the samples of both areas which may be due to the metamorphoses and/or introduction of carbon dioxide.

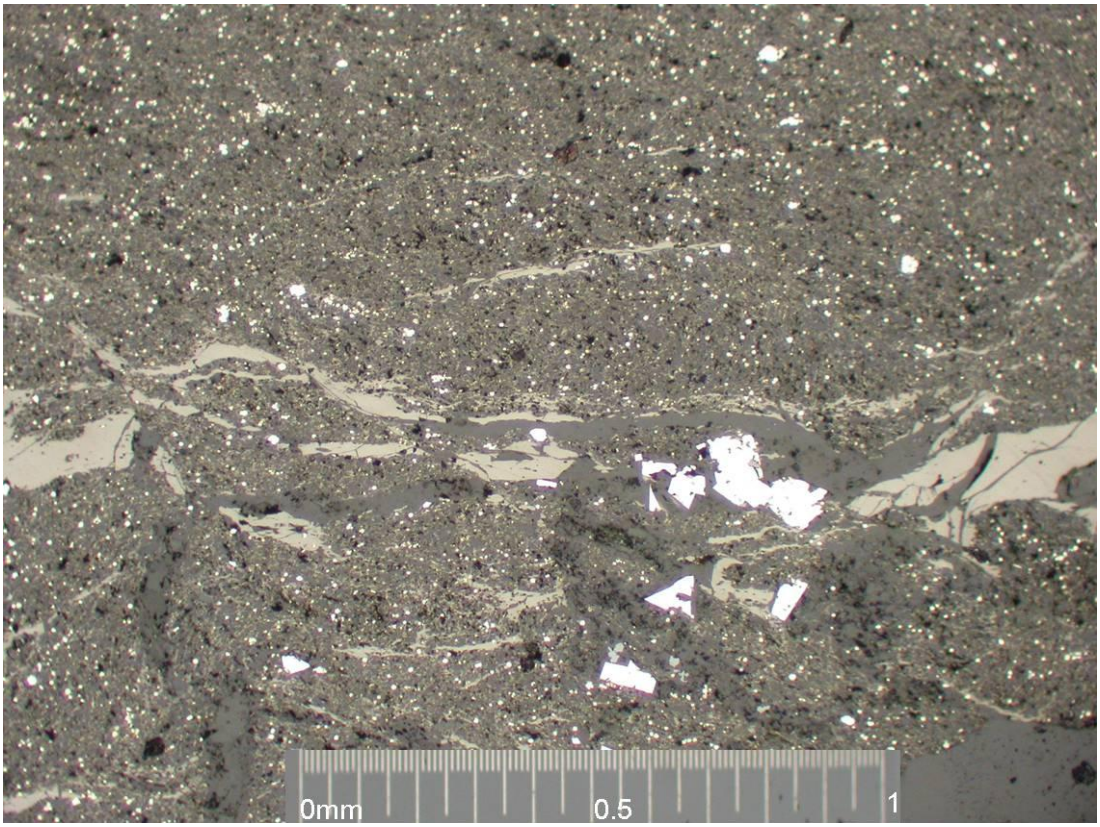

Figure 4-13 recrystallized graphite formations in the veins, framboidal pyrite in round dispersed and cubic pyrite large white formation in the center towards the right in Knows gate area. KS-1 X10

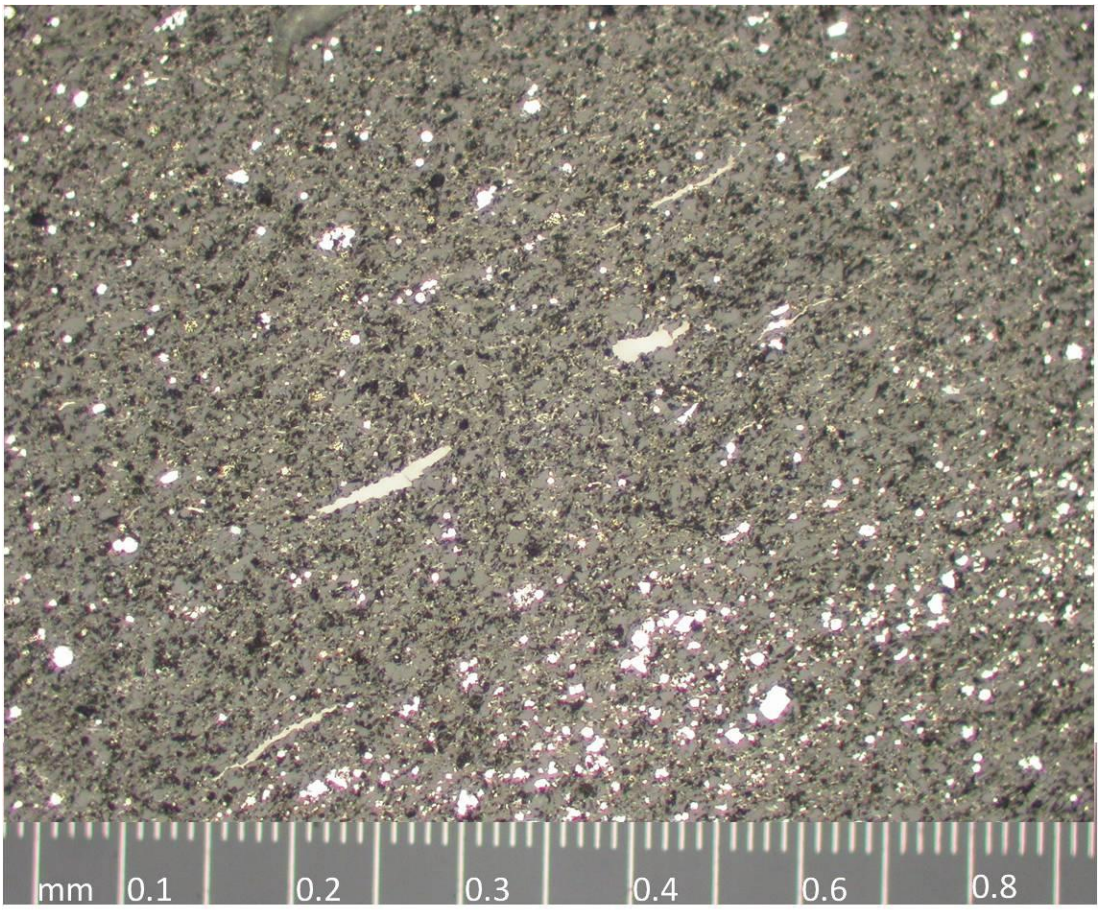

Figure 4-14 the formations of parallel bedded graphite flakes in the Slemmestad area depicts the low level of carbon compared with the Konows gate area. The pyrites are mostly framboidal. X20 SLE

Minerals which were not found using the XRD analysis were found in the optical microscopic view. Minerals like chalcopyrite, pyrrhotite, sphalerite, barite, graphite and dolomite were visible in the petrography microscope. Perhaps these minerals exist in small concentration which can't be detected by the XRD technique.

Even if the quantification of the minerals concentration is very tedious and time consuming, the ore microscopic analysis have the best view of the different sulfide minerals even existing in very small amount. In addition to the difficult quantification of the minerals the Petrographic microscopic couldn't show you the elemental composition of the minerals. It needs support of the SEM specially to see the elemental composition of new minerals and if you are hesitations of the type of mineral.

4.1.5 Scanning Electron Microscopy (SEM)

The scanning electron microscopy is used to identify different minerals in the samples from their backscatter intensity detection, and energy dispersive X-ray detection was used to quantify their chemical composition.

Two types of samples preparation techniques were employed to undertake the SEM study of the samples. The first one is polished specimen in epoxy cover and conductive carbon coating used to avoid the back scattering signal from the surface, and the second was rough-cut specimen to detect the type of mineral structure and covered with conductive gold coating.

Analyses of polished specimens with epoxy cover and rough-cut samples was done for all the six samples and analysis of one sample from Konows gate was done on rough-cut specimen. In the next sections below, the results are described as follows.

4.1.5.1 Polished section

SM sample from Slemmestad area

In the XRD analysis, quartz, pyrite, muscovite, orthoclase, albite and gypsum were found. It is also possible to identify these minerals in the SEM. Moreover, the SEM was capable of identifying more minerals in the polished section such as sphalerite, and chalcopyrite (see Figure 4-15 and table 4-5 below). The chalcopyrite and sphalerite were not detected by the XRD due to their very small abundance in the bulk of the rock. Since the iron content of the sphalerite in spectrum 4 of Figure 4-15 is very low, the value did not appear in Table 4-5.

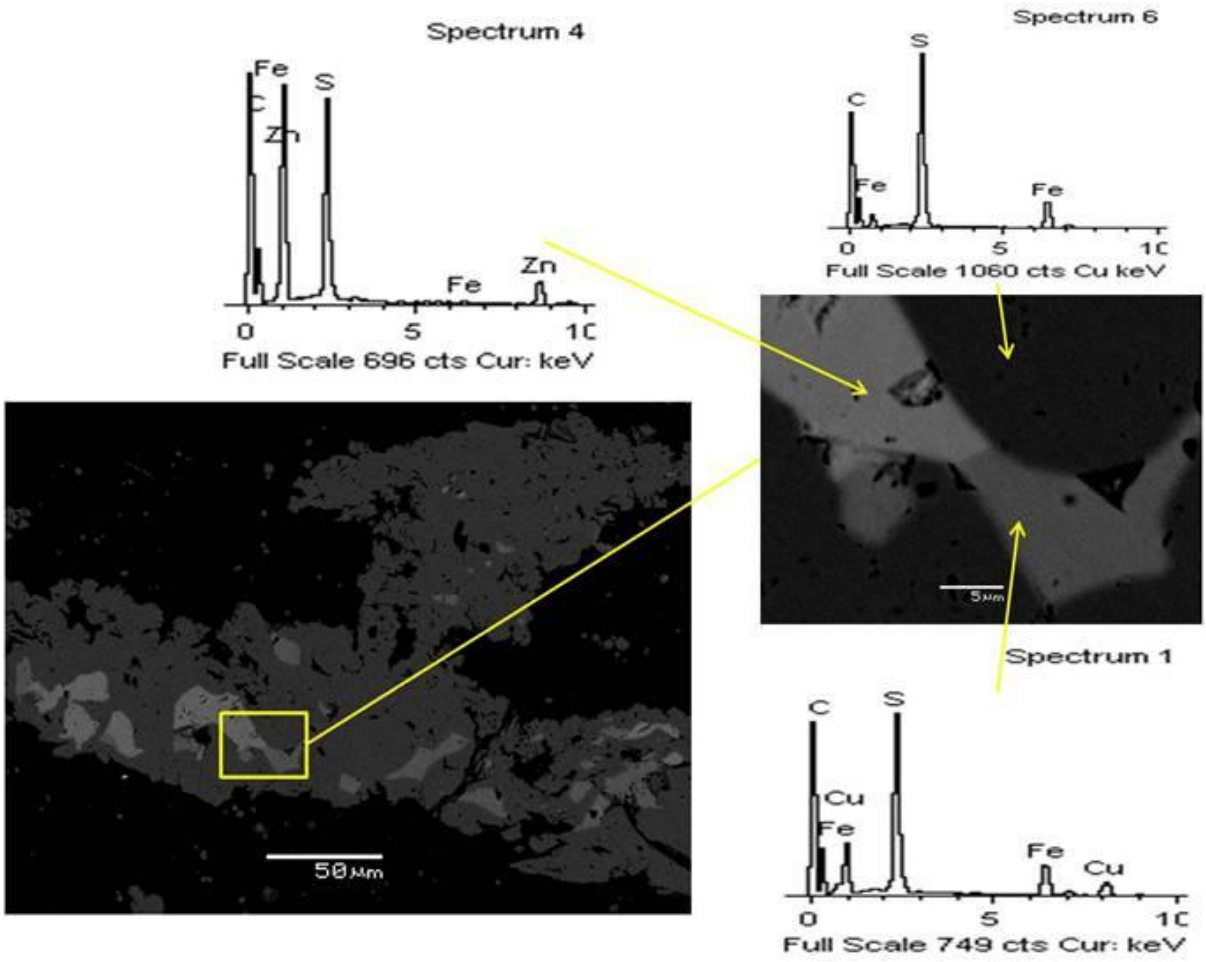

Figure 4-15 Slemmestad SM sample with chalcopyrite, zinc sulfide and pyrite (FeS_2)

Table 4-5 Weight percentages of the elements of the minerals in the Figure 4-15

Spectrums	S	Fe	Cu	Zn	Minerals
1	37.24	31.56	31.20		Chalcopyrite
2	37.45	32.58	29.97		Chalcopyrite
4	41.96			58.04	Sphalerite
5	54.93	45.07			Pyrite
6	53.52	46.48			Pyrite

SW sample from Slemmestad area

In the SEM micrograph below, the minerals pyrite, barite and chalcopyrite were found in the sample. The pyrite was also detected by the XRD since it is abundant in the sample.

The result of the XRF showed high Ba in the Slemmestad SW sample and the lowest calcium recorded. Barites is the most common barium mineral, occurring mainly as veins or cavity filling concentrations in shales and commonly associated with pyrite, quartz, zinc minerals and carbonates (Deer et al. 1966). Appreciable replacement of barium by calcium is an uncommon and its solubility in water is very slight at room temperature.

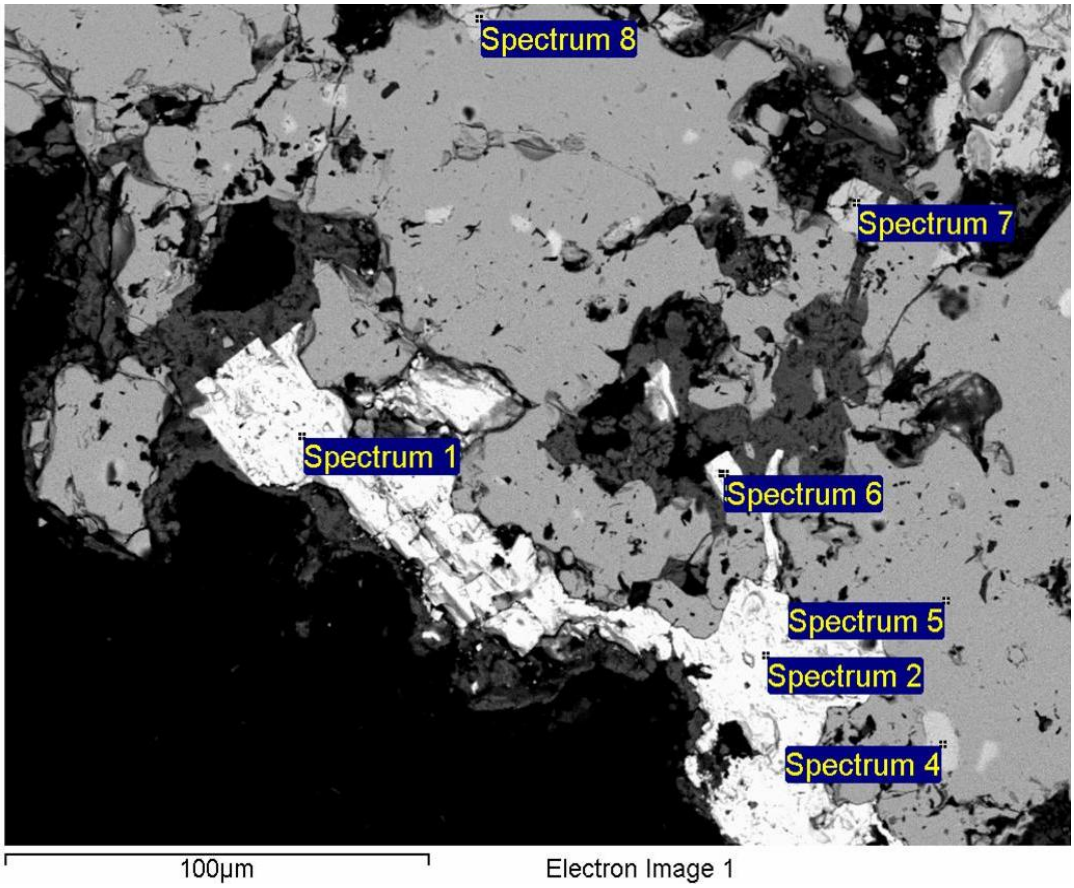

Figure 4-16 the white area in spectrum 1 and 2 are barite ($BaSO_4$), in the vast grey area with slightly bright spots in spectrum 4, 7, and 8 is chalcopyrite ($CuFeS_2$), and the large grey area with spectrum 5 is pyrite(FeS_2)

Table 4-6 spectrum analysis result of the minerals elemental composition in atomic %

Spectrum	O	S	Fe	Cu	Sr	Ba	Minerals
1	34.05	33.21			3.70	29.04	Barite
2	34.33	33.22			1.69	30.76	Barite
3	34.42	34.96			2.35	28.27	Barite
4		52.86	26.52	20.63			Chalcopyrite
5		67.58	32.42				Pyrite
6	34.88	33.79				31.33	Barite
7		51.67	26.38	21.96			Chalcopyrite
8		53.03	24.94	22.03			Chalcopyrite

SL sample from Slemmestad area

In the XRD analysis the minerals quartz, muscovite, pyrite, bernalite ($Fe(OH)_3$), K-feldspar and gypsum were found. From the spectral analysis outlined below pyrite, quartz, microcline (potassium feldspar), and muscovite were identified in the sample.

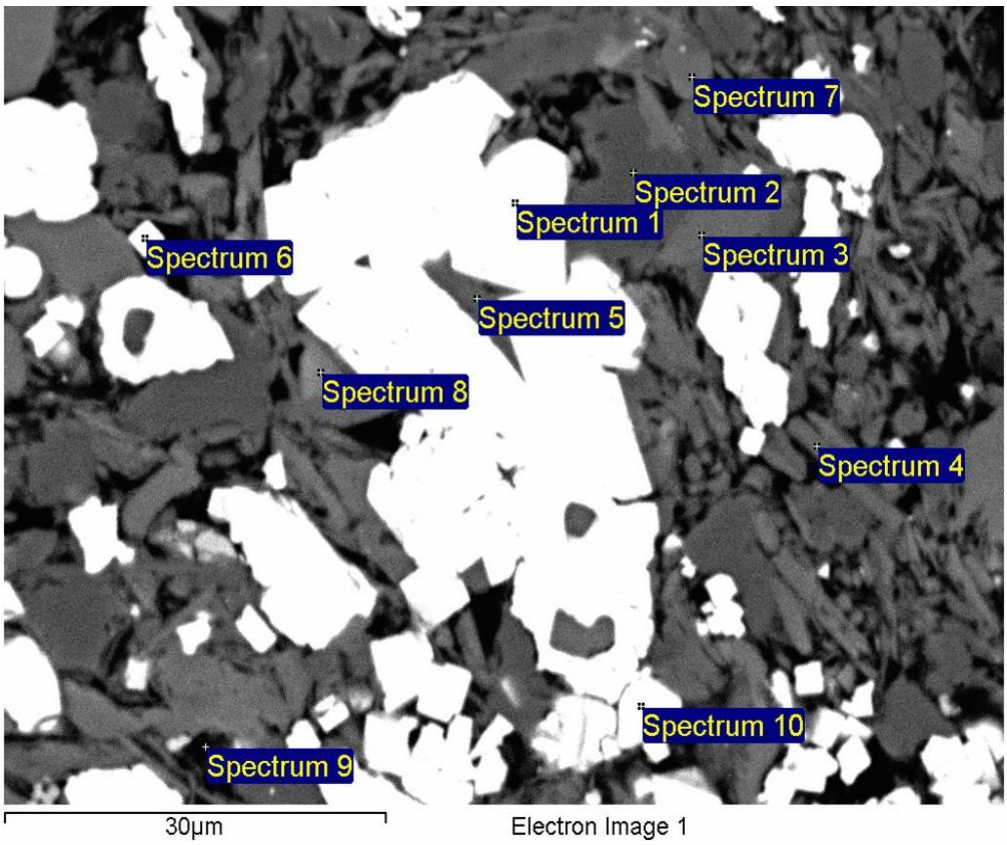

Figure 4-17 SEM image of the minerals pyrite in spectrum 1, 6, and 10 with white color, microcline in light gray with spectrum 3, 7 and 8, and muscovite in dark gray.

Table 4-7 the minerals and atomic percent of the elemental compositions of the spectrums from the images of SEM in Figure 4-17

Spectrum	O	Mg	Al	Si	S	K	Fe	Mineral
1					67.60		32.40	Pyrite
2	44.81			55.19				Quartz
3	39.98		10.60	38.23		11.19		Microcline
4	41.68	1.42	18.40	29.96		7.24	1.31	Muscovite
5	40.88	2.08	16.50	31.06	2.53	6.95		Muscovite
6					67.67		32.33	Pyrite
7	40.18		10.40	38.74		10.68		Microcline
8	40.60		11.00	38.02		9.24		Microcline
9	35.13	1.64	17.27	34.98	4.29	6.69		Muscovite
10					67.90		32.10	Pyrite

KS1 sample from Konows gate area

The carbonate minerals are important hosts for calcium and magnesium: dolomite $CaMg(CO_3)_2$, calcite $CaCO_3$. The XRF result depicted almost equal amount of Ca and Mg in the KS1 sample with a slightly higher value of calcium, which may come from calcite. From the XRD, the calcite peak is higher than the dolomite one, pointing to other calcium containing minerals. In Figure 4-18 below chalcopyrite showed in white. It was not found in the XRD due to its small amount in the whole bulk analysis. The dark spectrum 1 and 2 (in Figure 4-18 below) are quartz grains which was found in the XRD too.

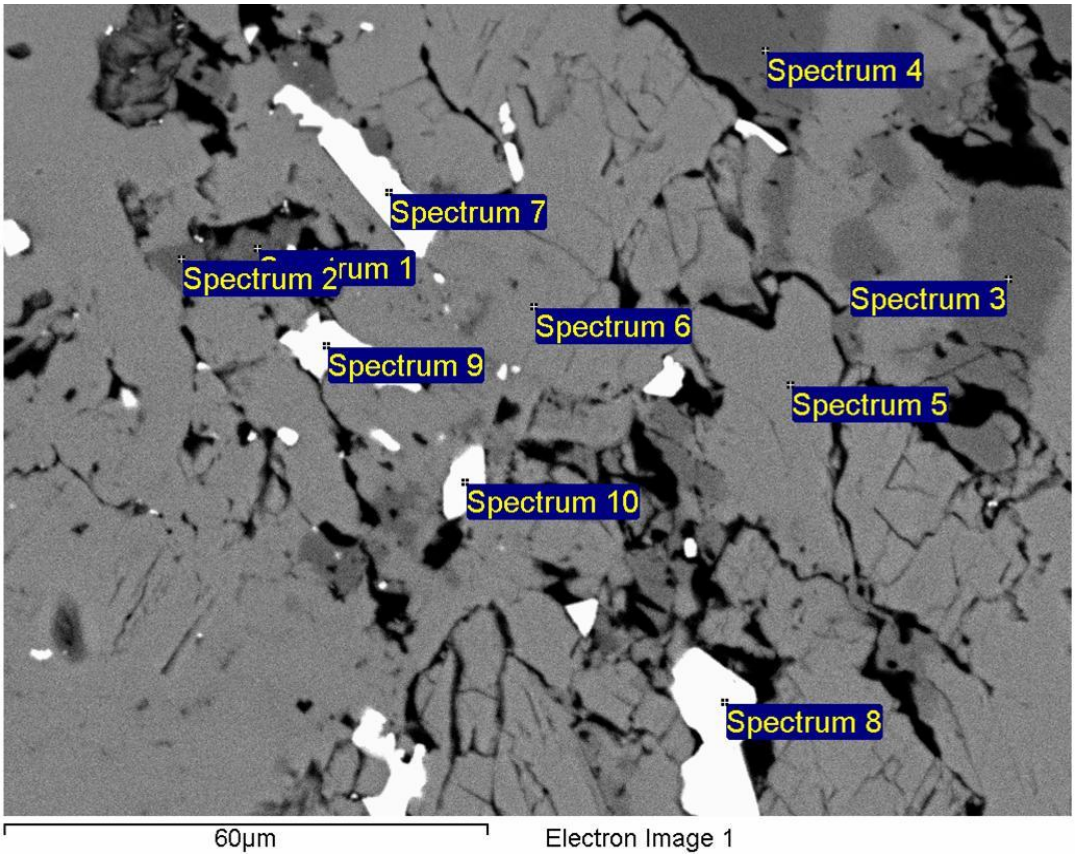

Figure 4-18 SEM image in dark gray color with spectrums 1 and 2 quartz, with spectrums 3 and 4 with slightly bright from quartz is dolomite, light gray in spectrums 5 and 6 is calcite and the white color chalcopyrite in spectrums 7, 8, 9 and 10

Table 4-8 the elemental compositions of the minerals in the fig – 5.14 in atomic%

Spectrum	O	Mg	Al	Si	S	K	Ca	Fe	Cu	minerals
1	47.94		2.06	49.07		0.93				Quartz
2	48.05			51.95						Quartz
3	60.50	15.90					20.92	2.68		Dolomite
4	59.91	17.66					20.64	1.79		Dolomite
5	61.70						38.30			Calcite
6	61.04						38.96			Calcite
7					50.98			26.37	22.65	Chalcopyrite
8					51.97			25.42	22.61	Chalcopyrite
9					51.33		1.14	24.72	22.81	Chalcopyrite
10					51.18		1.70	24.95	22.18	Chalcopyrite

KS2 sample from Konows gate area

In the SEM micrograph barite and sphalerite were detected in the sample. They were not found in the XRD. This may be due to low abundance in the bulk of the rock. In both the SEM and XRD analysis the minerals quartz, calcite, pyrite, and microcline were found.

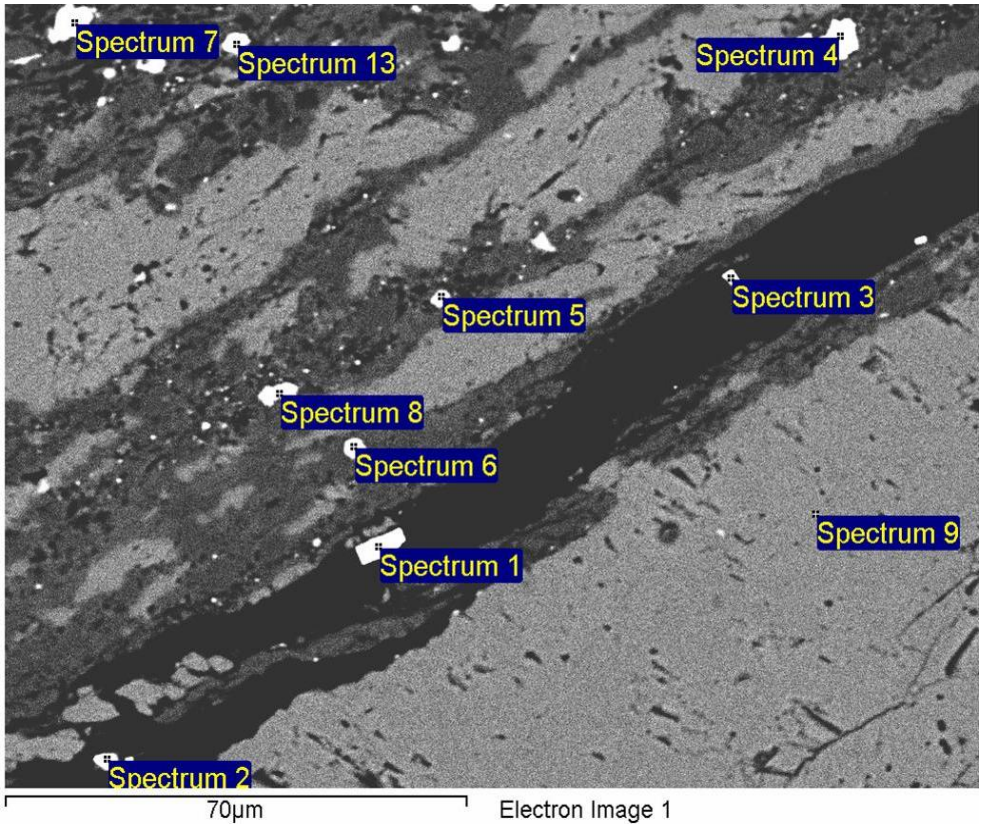

Figure 4-19 barite, quartz, pyrite, microcline and sphalerite micrograph

Table 4-9 elemental composition of the SEM image in Figure 4-19 in weight %

Spectrum	O	Al	Si	S	K	Fe	Zn	Ba	minerals
1	9.05			16.23				74.31	Barite
2	7.76			18.13				70.61	Barite
3	9.68			18.37				71.95	Barite
4				54.99		45.01			Pyrite
5			2.21	54.18		43.61			Pyrite
6				55.47		44.53			Pyrite
7				53.72		46.28			Pyrite
11	27.78	7.05	60.62		4.54				Microcline
12	28.55	1.21	70.24						Quartz
13	3.47	2.01	4.02	39.44			51.1		Sphalerite
14			1.30	54.33		44.37			Pyrite

In Figure 4-20 the mineral calcite, pyrite and quart are depicted. The quartz is not as such reactive mineral. The pyrite undergoes oxidation reaction and the calcite can dissolve with the presence of water and oxygen. The water and oxygen can enter through pore spaces and fracture zones so that pyrite oxidation in the presence of calcite can takes place in the alum shale. This formation is common in all the samples analyzed and can be representation of the geochemical reaction in the alum shale.

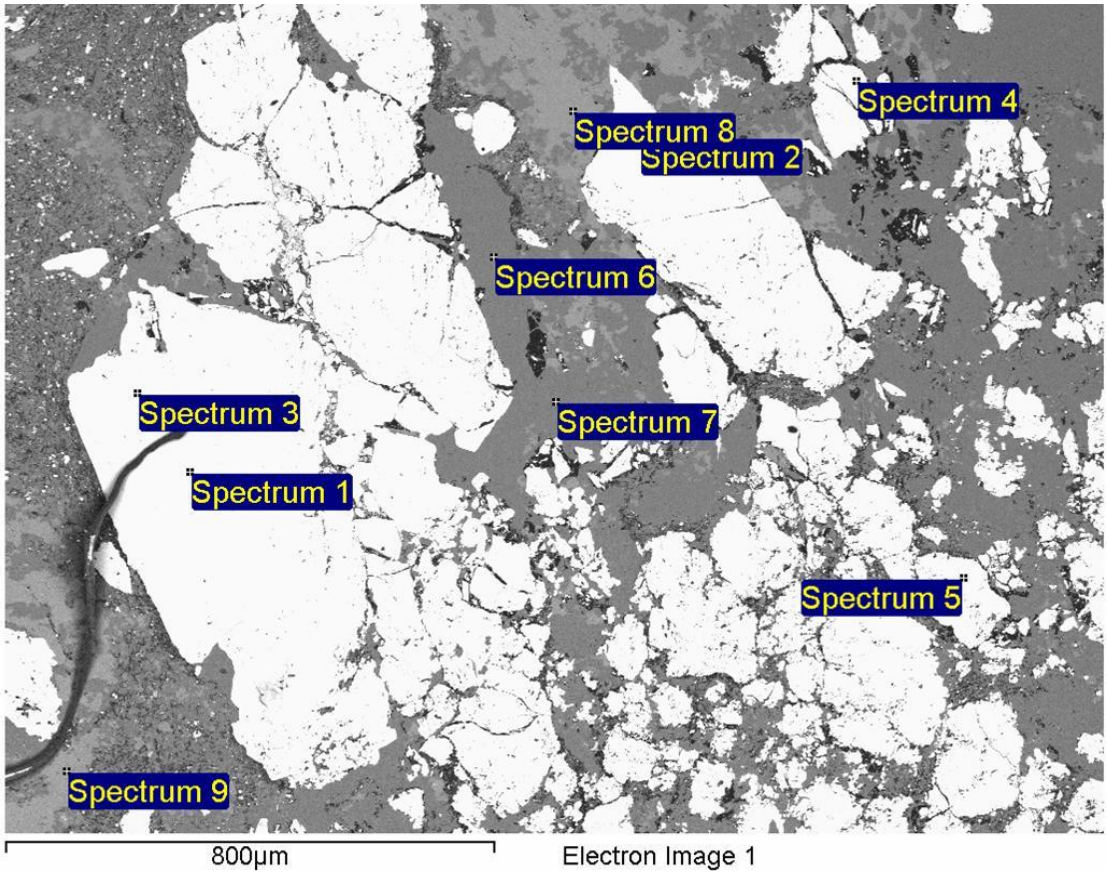

Figure 4-20 SEM detected calcite, pyrite and quartz

Table 4-10 elemental composition of the minerals detected in Figure 4-20 in weight%

Spectrum	O	Si	S	Ca	Fe	Minerals
1			52.98		47.02	Pyrite
2			52.07		47.93	Pyrite
3			54.58		45.42	Pyrite
4			53.61		46.39	Pyrite
5			54.26		45.74	Pyrite
6	32.99	67.01				Quartz
7	26.38	73.62				Quartz
8	34.03			65.97		Calcite

Black shale sample

As it was found in the petrographic microscope, it was also possible to see the pyrrhotite in the SEM from the black shale sample. However, in the SEM it is very difficult to differentiate the pyrrhotite from the reflection intensity of chalcopyrite and pyrite (see Figure 4-21). The advantage of the SEM is to see the chemical composition of the minerals at the same time with the backscatter image and the iron and sulfur ratio of the pyrite and the pyrrhotite also elucidated in table 4-11.

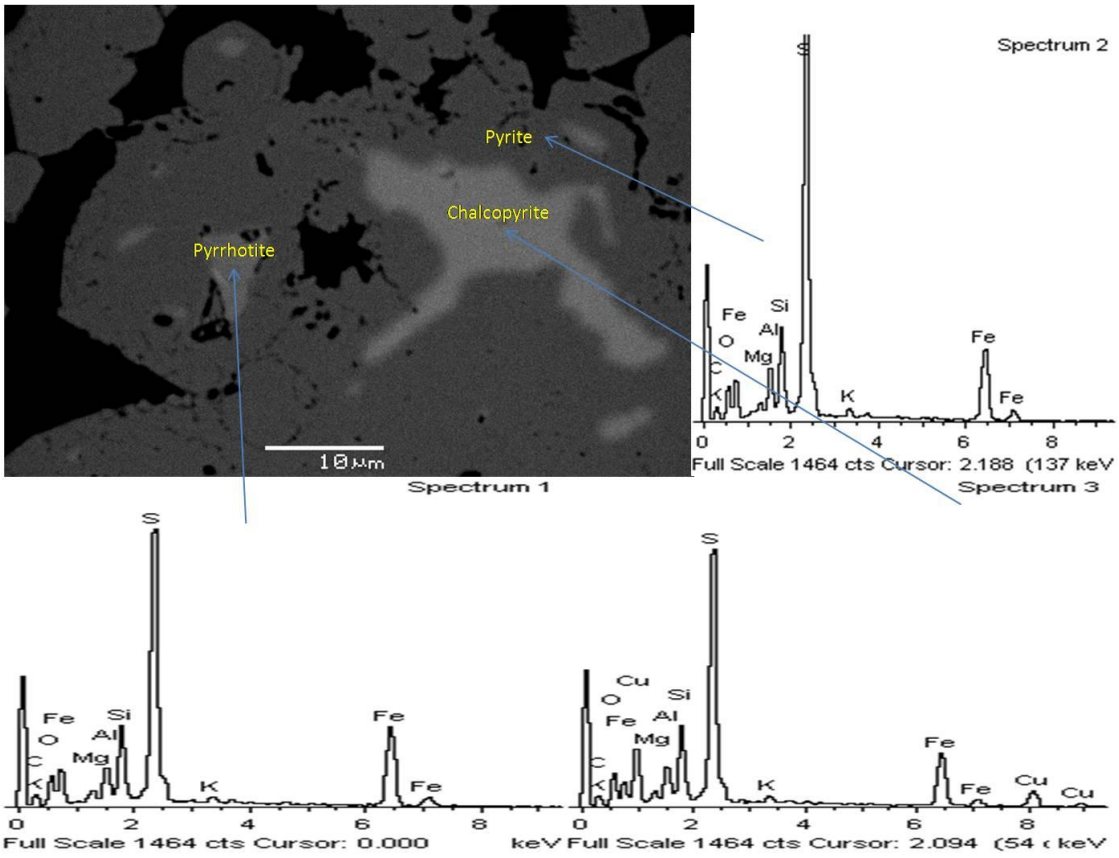

Figure 4-21 Pyrrhotite in light gray, chalcopyrite in white and pyrite in dark gray color of SEM image without carbon coating which have backscatter of the surface was showed up in the spectrums in addition to the minerals spectrum

Table 4-11 Spectral compositions of the minerals in the black shale sample of the spectrums from Figure 4-21

Spectrum	C	Mg	Al	Si	S	Fe	K	Cu	O	Minerals
1	9.21	0.41	1.22	2.72	10.40	9.19	0.27	-002	66.60	Pyrrhotite
2	8.97	0.34	1.17	2.30	12.19	6.69	0.25	003	68.06	Pyrite
3	8.49	0.47	1.26	2.96	10.13	6.62	0.26	3.71	66.11	Chalcopyrite

4.1.5.2 SEM analysis of rough-cut of sample from Konows gate areas

To see how the minerals structural associated together in the rock samples and measure the pyrite grain size, a rough-cut of the sample from the Konows gate area was analysed in the SEM. The chemical compositions of the grains were analysed in atomic percent and presented in the following Figure 4-22 and the measured grain size is presented in Figure 4-23.

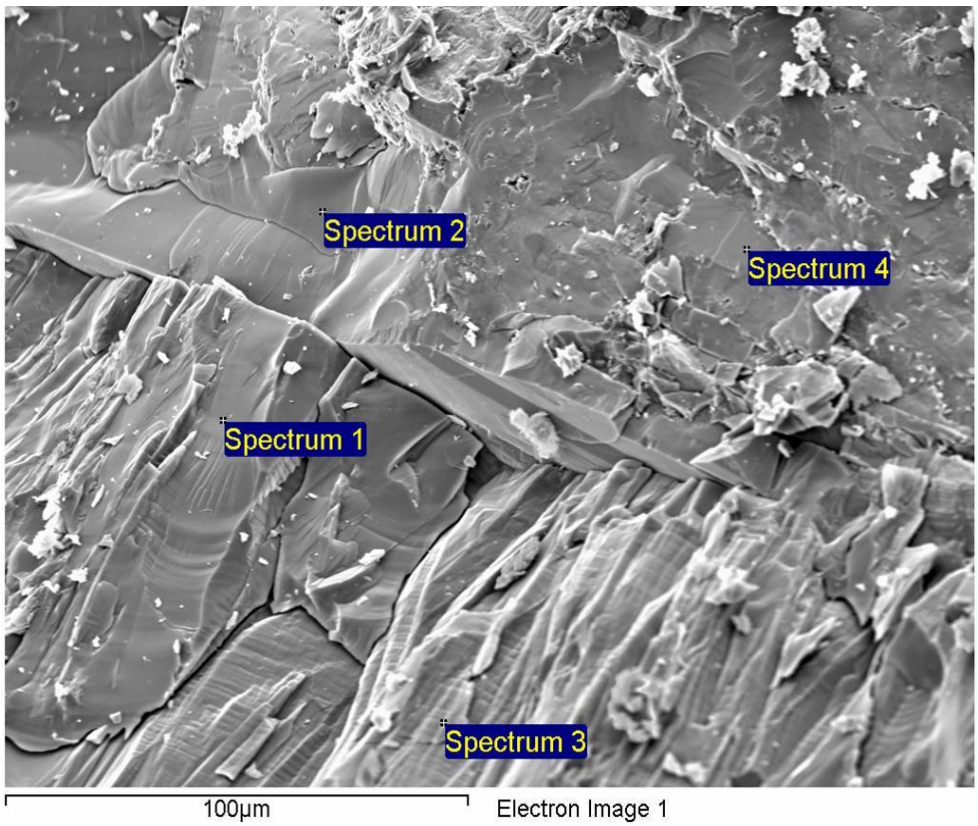

Figure 4-22 one of the structural arrangement of pyrite with spectrum 2 and 4, and quartz with spectrum 1 and 3

Table 4-12 chemical compositions of the spectrums of the pyrite and quartz in the Figure 4-22

Spectrum	C	O	Si	S	Fe	Minerals
1	33.71	38.10	28.19			Quartz
2	42.03			39.24	18.73	Pyrite
3	40.16	33.96	25.88			Quartz
4				65.89	34.11	Pyrite

In the spectrum 2 and 4 sulfur and iron were found in two to one ratio which is the pyrite composition and spectrum 1 and 3 were quartz with some carbon associated with it. The structure outline perpendicular overlay of the pyrite cubic formation with quartz grains which may be a line where fracture starts to develop.

One of the advantage of the SEM were to have the weight or atomic percentage of the different minerals identified from their backscatter variability. In the petrographic microscope study, it was possible to see in different color of the three sulfide types with better identification from their reflection in the optical light but not easy to quantify the minerals content or not user friendly system.

Generally the microscopic study have the advantage of measuring the grain size and as well as identifying mineralogical composition in qualitative terms from their optical properties and quantitatively from point count analysis in the ore microscopy and back scatter emission of the secondary X-ray in the SEM. It is also possible to see the nature of the depositional environment like the tectonicity and folding properties and the development of the fracture lines and formation of minerals following certain patterns.

The disadvantage is only small portion of the rock sample used to see through the microscopes, which may not be good enough to represent the whole sample rock and difficult to get general information about the rock. It may take very long time and become tedious to do many samples to have the representative data for the whole rock. For the case of the ore microscopic study, it needs very skilled personal to prepare the samples and detect through the microscope.

4.2 Modeling of the reactivity of the alum shale

4.2.1 Reactivity of the minerals in the alum and black shale samples

The reactivity of the alum shale is mainly controlled by the iron sulfide, calcite, water and oxygen. The other minerals like the illite and K-feldspar are not such reactive minerals in the alum shale. The pyrite, which is the most abundant mineral in the alum shale, plays the central role in the reactivity of the shale and its aqueous oxidation is modeled using the PREEQC with respect to different levels of the calcite, pyrrhotite, oxygen and water. The amount of pyrrhotite which is one of the very reactive iron sulfides was low. It was not detected by the bulk XRD mineralogical analyses, but very little spot found during the microscopic analysis of the black shale sample. However the sulfur analysis gives what is considered a correct value of pyrrhotite (as acid soluble sulfide).

Though time the change in mineralogical composition of the alum shale due to the aqueous oxidation of pyrite need to be assessed to avoid hazard on the overlaying buildings. Therefore the rates of pyrite oxidation with the coexisting minerals in the alum shale were simulated. The simulations are discussed in detail in the following sections.

4.2.2 Rates of pyrite oxidation

The formula for rate law of change in solute concentration due to the reactions was taken from Appelo (Appelo and Postma 2005) and used for calculating the rate of the reaction and the specific rates from data compiled by Williamson and Rimstidt (Williamson and Rimstidt 1994). The overall reaction rate (R) in mol/L/s is given by

$$R = k\, A_o/V\, (m/m_o)^n\, g(c)$$

Where k is the specific rate constant (mol/m^2/s), A_o is the initial surface area of the solid (m^2), more precisely the reactive surface area, V is the volume of solution (m^3), m_o is the initial moles of solid, m is the moles of solid at a given time, and $(m/m_o)^n$ is

a factor to account for changes in A_o / V during dissolution and also for selective dissolution and aging of the solid. For uniformly dissolving spheres and cubes n = 2/3=0.67.

The g (c) is a function that comprises the effects of the solution composition on the rate, like the distance from equilibrium, and the effects of catalysis and inhibition (Aagaard and Helgeson 1982). The simulations in this study were done to see the calcite and pyrrhotite effects on the rate of the pyrite oxidation.

Two different simulations were done to see the effect of calcite. The first simulation was done with the concentration level of the calcite in the alum shale and the second simulation is without calcite. Both simulations were done with fixed amount of oxygen. Since pyrrhotite is very reactive mineral, it may have an effect of increasing the rate of the pyrite oxidation even at very small concentration. The third and fourth simulation was done to see the effect of pyrrhotite at two different levels. The first was undertaken at the minimum concentration effect and the second a high concentration to clearly see the effect on the rate of the pyrite oxidation.

One last simulation was undertaken to see the effect of oxygen and water. In this simulation constant supply of oxygen with atmospheric pressure was added into the solution. The input data are described in detail in the sections below.

Concentration of Pyrite and Calcite

The level of pyrite was calculated from the measured chemical analysis data from the Konows gate with the lower total sulfur content, which is 7.29%. Since the XRD mineralogical analysis and the microscopic analysis of the sample revealed pyrite to be the only disulfide mineral in the sample. The monosulfide (0.034%) and the sulfate (0.027%) measured, were subtracted from the total sulfur to get a value 7.2% of sulfur in the pyrite form. In the simulations below the simulations below the pyretic concentration of 3.015 moles per liter solution was used.

The concentration of calcite calculated from the calcium concentration analyzed using the XRF. Since the mineralogical analysis of the sample using XRD showed the calcite is the only calcium containing mineral found in the sample. Therefore the concentration of calcite used in the simulations is 1.14% by weight. The input calcite concentration becomes 2.837 moles per liter.

Surface area of pyrite

The oxidation of pyrite is directly proportional to its effective surface area, so that the framboidal and euhedral pyrite have extremely high difference in their oxidation rate. The framboidal pyrite which was found more in the Slemmestad areas compared to the Konows gate area has higher surface area than the cubic pyrite. The framboidal pyrite grains have 1 to 5 µm diameter and the cubic pyrites have 150 to 600 µm diameter (Lowson 1982). Even if the pyrite concentration found in the Slemmestad area is very small compared with the Konows gate area, their reactivity is high due to their high surface area.

The surface area of the pyrite was calculated from approximated cubic structure of euhedral pyrite grain sides measured using the SEM analysis of the rough cut sample (see Figure 4 - 23). The measured sides were 300X200X100 μm^3 in the middle the big grain. The geometry of the grains assumed to be close to cubic so that the surface area is calculated as follows

The volume of the grain (V_g) was calculated

$V_g = 200X300X100\ \mu m^3 = 6X10^{-12}\ m^3$

The specific gravity which is the density of pyrite to the density of water is 4.9 to 5.2. An average value of the specific gravity of 5 was taken and the density of pyrite becomes 5000 Kg/m^3 compared with water. Therefore the volume of 1Kg pyrite is 0.0002 m^3.

The number of grains per Kg pyrite = volume of 1Kg pyrite/volume of a grain = 0.0002m^3/6e-12 m^3= 3.33e+7

The surface area of a grain (A_g) = 2(100x200 + 100x300 + 200x300) μm^2= 2.2e-7 m^2
The surface area of 1Kg grain = A_g * No. grains per 1Kg grains = 2.2e-7 m^2*3.33e+7= 7.3326 m^2

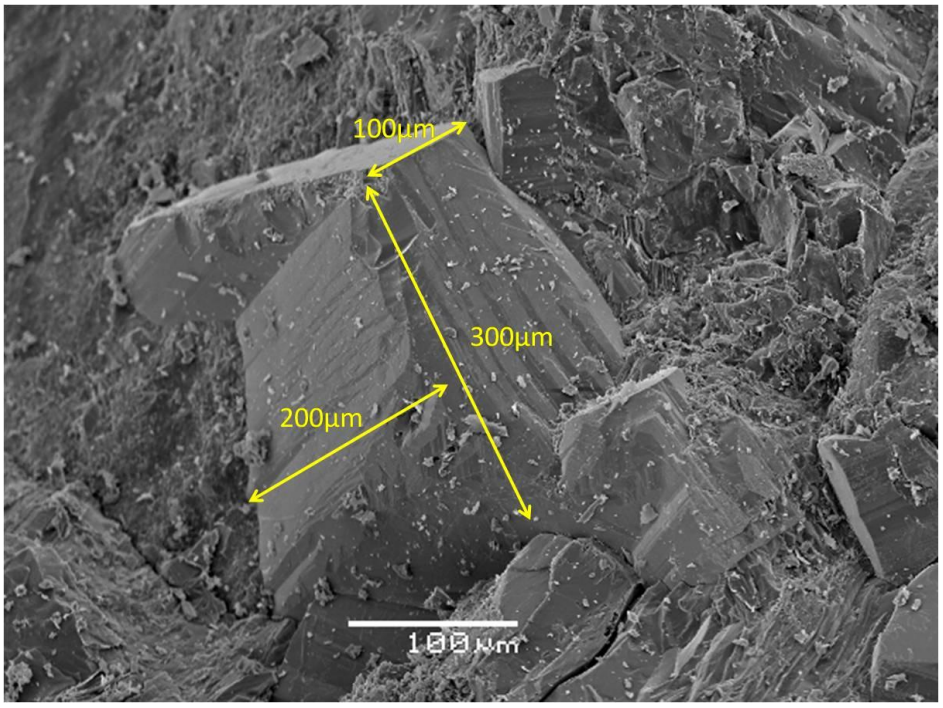

Figure 4-23 structure of pyrite grain measure sides 300X200X100 μm^3 in the middle the big grain

Specific rate of reaction

The specific rate of pyrite oxidation by O_2 is based on detailed measurements in solutions with varying concentrations of aqueous species that influence the rate is described by Williamson and Rimstidt (Williamson and Rimstidt 1994)

$$r= 10^{-8.19} m_{O2}{}^{0.5} m_{H+}{}^{-0.11}$$

This rate expression is applicable only for the dissolution reaction, and when the solution contains oxygen. The rate has a square root dependency on the oxygen concentration, indicating a large effect at low oxygen concentrations while at higher

concentration the effect is small. The effect of pH on the rate is very small. The rate of pyrite oxidation by Fe^{3+} is many times faster than the presence of oxygen which is again described by Williams and Rimstidt (1994).

$$r = 10^{-6.07} m_{Fe3+}{}^{0.93} m_{Fe2+}{}^{-0.40}$$

The overall rate determining step in the oxidation of pyrite is the cathodic site of the reaction where Fe^{2+} and H^{+} compete with Fe^{3+} for sorption (Rimstidt and Vaughan 2003). The corrected numerical model for calculating the specific rate of pyrite which avoids artifacts at the high and low concentration limits and also used in PHREEQC is

$$r = 6.3x10^{-4}\ mFe_{3+}{}^{0.92}\ (1 + mFe_{2+}/10^{-6})^{-0.43}$$

Where r is in moles/m2/s

4.2.3 The effect of calcite on pyrite oxidation

Oxidation of pyrite with the presence of calcite

The oxidation of pyrite with calcite was done for the period of 100 years time. The level of pyrite decreased from 3.02 to 1.95 moles per liter which is 1.07 moles or 128 gram (see the result of the simulation in Figure 4-24 and Table 4-13 below). On the other hand the level of gypsum ($CaSO_4$) increased by 1.498 moles or 204 gram. Since initial solution of the simulation had 0.005 moles per liter gypsum with saturation index (SI) of - 0.01 and the first simulation had SI of 1.73 the whole 204 gram gypsum precipitated (SI above zero indicates precipitation). The increase in gypsum was due to calcite dissolution resulted in increased calcium ion in the solution which reacted with sulfate released from pyrite oxidation to form gypsum. The sulfur from pyrite oxidation also forms sulfate containing mineral like FeSO4 and others. The sulfate released from oxidized pyrite has 68.5 g of the sulfur (calculated based on the oxidation reaction in section 2.3.2 the first equation 1 mole pyrite oxidized to releases 2 moles of sulfate ions) out of which 48.1 g precipitated as gypsum and the rest 20.5 g used to make other sulfate compounds. If we recalculate back from the sulfur to pyrite, the amount of pyrite become 0.75 moles which is 89.98 g. the density of pyrite is 5 g/cm^3 and the volume of 89.98 g is 18 cm^3. Gypsum has a specific gravity of 2.32 (2.32 g/cm^3), which is almost half of pyrite density. 204 g

gypsum has 88 cm^3. The difference in volume is 70 cm^3. The calcite destruction is not considered in the change of volume since the density difference between calcite (density 2.72 g/cm^3) and gypsum is insignificant.

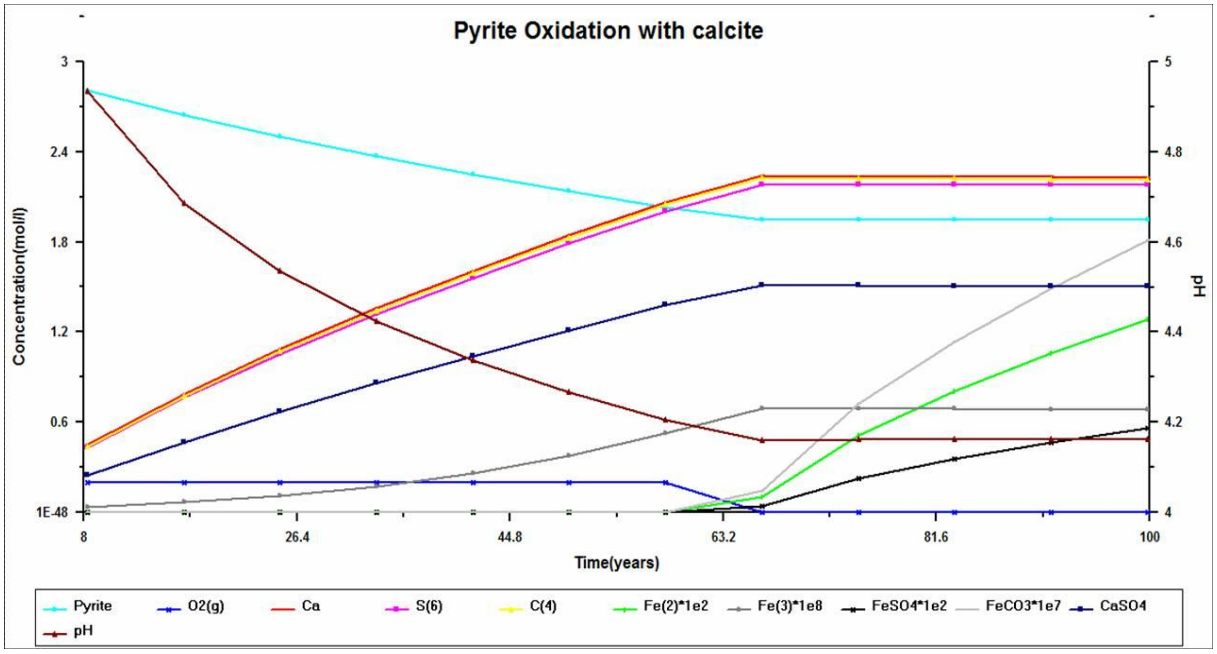

Figure 4-24 the simulation result of pyrite oxidation with calcite level in the sample in equilibrium with the pore water solution. The pyrite level in light blue, pH in brown, sulfate in pink, oxygen in light blue, iron sulfate in black, Fe(3) in light gray, Fe(2) in green and calcium sulfate in dark blue

Table 4-13 the simulation result of pyrite oxidation with the calcite level in the sample in equilibrium with the pore water solution.

Time (years)	Pyrite	$O_2(g)$	Ca	SO_4	CO_3	Fe(2)	Fe(3)	$FeSO_4$	$FeCO_3$	$CaSO_4$	pH
8.3	2.81	0.2	0.45	0.43	0.435	4.0e-16	4e-10	1.6e-16	5.0e-20	0.246	4.94
16.6	2.65	0.2	0.79	0.76	0.773	1.5e-15	7e-10	6.3e-16	9.1e-20	0.465	4.69
25.0	2.50	0.2	1.09	1.05	1.071	3.1e-15	1e-9	1.4e-15	1.3e-19	0.669	4.53
33.3	2.37	0.2	1.36	1.32	1.342	5.4e-15	2e-9	2.4e-15	1.6e-19	0.860	4.42
41.6	2.25	0.2	1.61	1.56	1.592	8.3e-15	3e-9	3.6e-15	1.9e-19	1.041	4.34
49.9	2.14	0.2	1.84	1.79	1.827	1.2e-14	4e-9	5.1e-15	2.2e-19	1.212	4.27
58.2	2.03	0.2	2.07	2.01	2.049	1.6e-14	5e-9	6.9e-15	2.5e-19	1.377	4.21
66.6	1.95	3e-44	2.24	2.18	2.225	1.0e-3	6.9e-9	4.4e-4	1.4e-8	1.510	4.16
74.9	1.95	4e-47	2.24	2.18	2.222	5.2e-3	6.9e-9	2.3e-3	7.2e-8	1.507	4.16
83.2	1.95	7e-48	2.24	2.18	2.219	8.1e-3	6.9e-9	3.5e-3	1.1e-7	1.506	4.16
91.5	1.95	2e-48	2.23	2.18	2.217	1.1e-2	6.9e-9	4.6e-3	1.5e-7	1.505	4.16
99.8	1.95	1e-48	2.23	2.18	2.215	1.3e-2	6.8e-9	5.6e-3	1.8e-7	1.504	4.16

The rate of pyrite oxidation or gradient of change in pyrite through time was high in the first 67 years and become close to zero which means the level of pyrite became constant. This is due to the hydrogen ion concentration is controlled by the carbonate released from the calcite dissolution. The carbonate ion reacts with the hydrogen ion to form bicarbonate ions. The ferric iron in the solution precipitates in the form of goethite at pH above 4 which intern the oxidation of pyrite hindered by the calcite dissolution due to reduced reactive surface area. The rate of oxidation of pyrite from year 8.3 to 58.2 which is the last time the concentration of oxygen to go down is 4.95e-10 moles/liter/second which is the overall rate of oxidation by oxygen.

The ferrous iron increases through out the simulation time and the ferric iron also increasing until the year 99.8. The ferric iron starts to decrease in the year 99.8 which may be due to the start of the ferric iron to oxidize the pyrite when the pH going down. In the oxygen depleted water the ferric iron oxidation of pyrite is fast processes. Even if the concentration is very low the ferrous sulfate and carbonate concentration also increased in the simulation time period. The increase in ferrous sulfate and carbonate become high after precipitation of gypsum is ceased.

Oxidation of pyrite in the absence of calcite

The simulation without calcite was done with the same input parameters like the simulation with calcite except the absence of calcite in the equilibrium phase. The result is shown in figure 4-25 and table 4-14 below. It depicted within five days the level of the pyrite went down to 1.94 moles per liter and afterwards the gradient of the pyrite level in time become constant which means the oxidation of the pyrite become close to zero. At the end of the simulation the level of pyrite became 1.8 moles which is lower than the oxidation with calcite (1.95 moles).

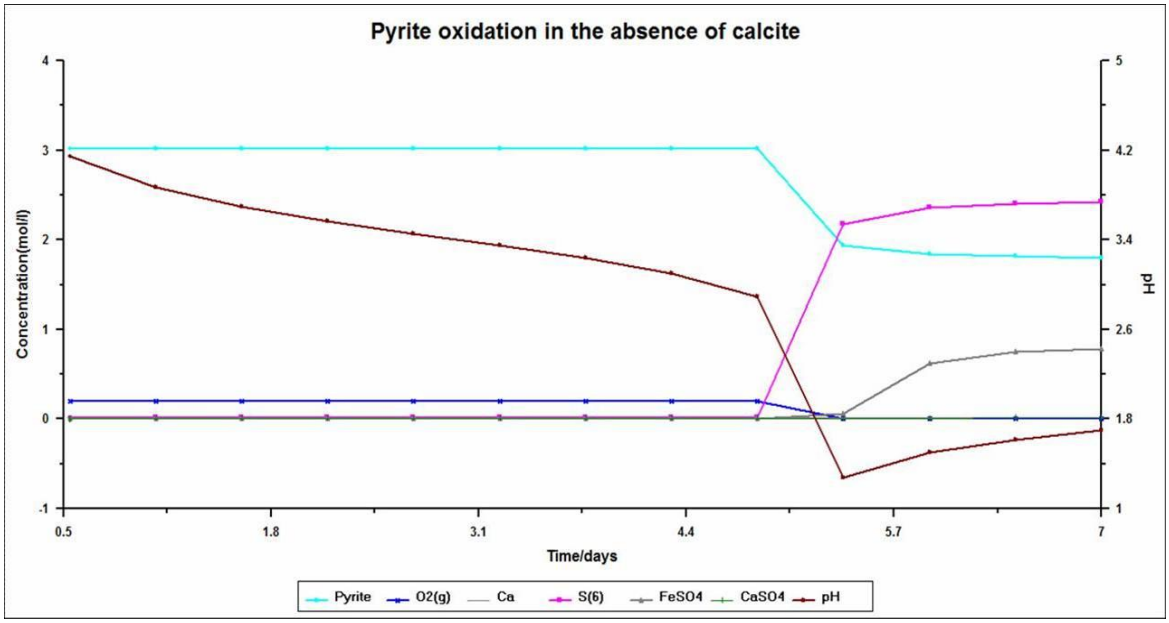

Figure 4-25 the simulation result of pyrite oxidation the absence of calcite. The pyrite level in light blue, pH in brown, sulfate in pink, oxygen in blue, iron sulfate in gray and calcium sulfate in green

Table 4-14 concentrations of selected minerals which changes much after the simulation of pyrite oxidation in the absence of calcite

Time (days)	Pyrite	O_2(g)	Ca	SO_4	Fe(2)	Fe(3)	$FeSO_4$	$CaSO_4$	pH
0.5	3.015	0.2	0.0154	0.02	3.9e-15	2.9e-9	1.2e-15	0.005	4.2
1.1	3.015	0.2	0.0154	0.02	1.4e-14	8.4e-9	4.4e-15	0.005	3.9
1.6	3.015	0.2	0.0154	0.02	3.1e-14	1.8e-8	9.7e-15	0.005	3.7
2.2	3.015	0.2	0.0154	0.02	5.7e-14	3.5e-8	1.8e-14	0.005	3.6
2.7	3.015	0.2	0.0154	0.02	9.6e-14	6.5e-8	3.0e-14	0.005	3.5
3.2	3.015	0.2	0.0154	0.02	1.6e-13	1.2e-7	5.0e-14	0.005	3.4
3.8	3.015	0.2	0.0154	0.02	2.6e-13	2.4e-7	8.2e-14	0.005	3.2
4.3	3.015	0.2	0.0154	0.02	4.9e-13	5.6e-7	1.5e-13	0.005	3.1
4.9	3.014	0.2	0.0154	0.02	1.3e-12	2.2e-6	4.1e-13	0.005	2.9
5.4	1.936	1.1e-30	0.0154	2.18	1.8e-01	1.2	0.06	0.007	1.3
5.9	1.842	5.1e-36	0.0153	2.36	1.6	0.4	0.62	0.009	1.5
6.5	1.814	2.4e-37	0.0153	2.41	2.0	0.2	0.75	0.010	1.6
7.0	1.802	2.8e-38	0.0153	2.43	2.2	0.1	0.79	0.011	1.7

The rate of pyrite oxidation was 2.63e-9 moles/liter/seconds calculated for the period of time starting from the day 0.5 until 4.9 which is a period of time in which the oxidation takes place with oxygen. This shows the rate of pyrite oxidation with out calcite is very fast processes. The rate of pyrite oxidation with out calcite is very high due to the high amount of hydrogen ion in the solution which increases the specific rate of the reaction. Therefore the calcite dissolution controls the rate of pyrite oxidation indirectly through buffering the pH. The hydrogen ion became less mobile due to the release of carbonate from calcite dissolution which forms bicarbonate ions

in the solution. Therefore the calcite dissolution inhibits the pyrite oxidation through the control of hydrogen ion mobility.

The ferric iron increases at the beginning until around five and half days and start decreasing because of its use to oxidize the pyrite at low pH in the absence of oxygen which is a fast process which took down the level of pyrite from 3.014 to 1.936 moles within half a day. The pH slightly rises after day six which may be due to the hydrogen ion was used by ferrous ion to form ferric ion and water.

The calcium sulfate or gypsum growth starts after around five and a half days which may be due to increase in the level of sulfate ion in the solution. It is 0.01 moles per liter at the end of the simulation which is very low compared with the simulation with calcite, because here calcium ion in the solution is used to precipitate together with sulfate. Even if calcite decreases pyrite oxidation on the other hand enhances the gypsum precipitation due to calcium ion release into the solution.

4.2.4 The effect of pyrrhotite in the oxidation of pyrite

Pyrite oxidation with 0.0521 mol/liter pyrrhotite

The effect of pyrrhotite in the simulate was done in the same way as the simulation with calcite but in the case of pyrrhotite simulation 0.05 moles per liter of pyrrhotite was added in equilibrium with the solution.

The rate of pyrite oxidation in the first 58.2 years beginning from year 8.32 was 4.95e-10 moles/liter/second. The rate of pyrite oxidation in the presence of pyrrhotite was calculated using change in pyrite concentration through time. This simulation compared with the simulation with calcite could not show the reaction is faster.

The main difference compared with the values of the oxygen concentration at time 66.6 years is lower in the simulation with pyrrhotite compared with table 4-13 (without pyrrhotite) which indicates that the reaction rate is faster. The effect observed is too small to say the pyrrhotite had a catalytic effect. Therefore another simulation with higher concentration of pyrrhotite was done in the following section.

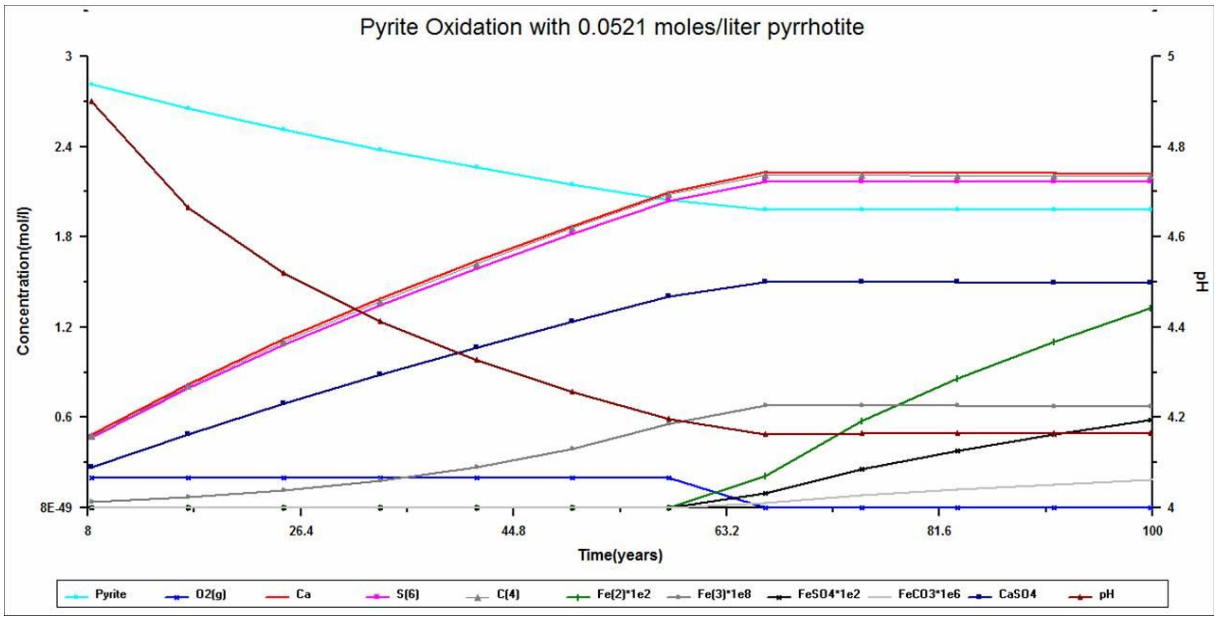

Figure 4-26 concentrations of selected minerals and element which changes much after the simulation with 0.0521 moles per liter pyrrhotite

Table 4-15 concentrations of selected minerals which changes much after the simulation of pyrite oxidation in the presence of 0.0521 moles per liter pyrrhotite

time	Pyrite	O_2(g)	Ca	SO_4	CO_3	Fe(2)	Fe(3)	$FeSO_4$	$FeCO_3$	$CaSO_4$	pH
8.32	2.82	0.2	0.49	0.47	0.47	4.8e-16	4.02e-10	2.0-16	5.4e-20	0.27	4.90
16.6	2.65	0.2	0.82	0.80	0.81	1.6e-15	7.35e-10	7.0e-16	9.5e-20	0.49	4.70
25.0	2.51	0.2	1.12	1.09	1.10	3.4e-15	1.18e-09	1.5e-15	1.3e-19	0.69	4.50
33.3	2.38	0.2	1.39	1.35	1.37	5.7e-15	1.81e-09	2.5e-15	1.7e-19	0.88	4.40
41.6	2.26	0.2	1.64	1.59	1.62	8.7e-15	2.70e-09	3.8e-15	2.0e-19	1.06	4.30
49.9	2.15	0.2	1.88	1.82	1.86	1.2e-14	3.93e-09	5.4e-15	2.3e-19	1.24	4.26
58.2	2.04	0.2	2.10	2.04	2.08	1.6e-14	5.57e-09	7.2e-15	2.6e-19	1.40	4.20
66.6	1.98	1.3e-45	2.23	2.17	2.21	2.1e-03	6.81e-09	9.3e-04	3.0e-08	1.50	4.16
74.9	1.98	2.4e-47	2.23	2.17	2.21	5.8e-03	6.79e-09	2.5e-03	8.2e-08	1.50	4.16
83.2	1.98	4.9e-48	2.22	2.17	2.21	8.6e-03	6.77e-09	3.8e-03	1.2e-07	1.50	4.16
91.5	1.98	1.8e-48	2.22	2.17	2.21	1.1e-02	6.76e-09	4.8e-03	1.6e-07	1.50	4.16
99.8	1.98	8.5e-49	2.22	2.17	2.20	1.3e-02	6.74e-09	5.8e-03	1.9e-07	1.50	4.17

Pyrite oxidation with 0.521 moles/liter pyrrhotite

The simulation to see, if pyrrhotite had a catalytic effect at higher concentration, proved that this was the case. The results are given in Figure 4-27 and Table 4-16. The time to consume the same level of oxygen is now 17 years faster than for the simulations with 0.0521 moles per liter pyrrhotite. This is due to the release of hydrogen ion into the solution which is shown in the gradient of the pH curve. In the first simulation, the pH dropped to 4.9 in year 8.32 and in this simulation the pH dropped to 4.62 in the same year. The concentration of Ca, SO4, CO3, Fe (2), Fe (3), FeSO4, FeCO3, and CaSO4 at the year 8.32 compared with the simulation with

0.0521 moles per liter pyrite raised very high at the first simulation. All the pyrrhotite was used in the first simulation and acidified the solution which also enhances the pyrite oxidation. However the amount of pyrite is not less compared with the simulation above.

The addition of pyrrhotite created low overall rate of pyrite oxidation since incomplete oxidation of pyrrhotite yields pyrite which increases the amount at the end of the 58.2 years. The rate of pyrite oxidation from year 8.32 to 58.2 is 4.95e-10 which is similar to the rate calculated with the 0.05 pyrrhotite concentration in the above simulation. The rate of change of pyrite with time is same due to the addition of pyrite from the pyrrhotite. Oxidative dissolution always produces a mineral with decreased cation content (increased sulfur content). Substantial cation loss from minerals can occur when the cations have high mobility in the minerals like pyrrhotite(Rimstidt and Vaughan 2003).

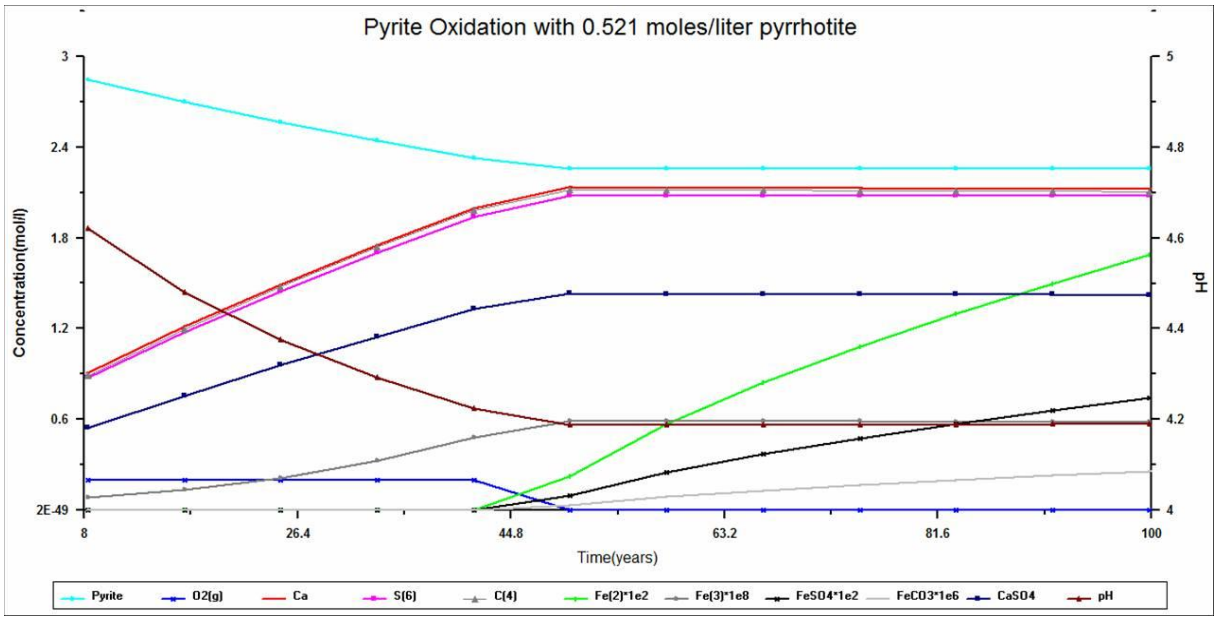

Figure 4-27 the rate of pyrite oxidation with 0.521 moles per liter pyrrhotite with concentrations of selected minerals and element with significant change in concentration

Table 4-16 concentrations of selected minerals which changes much after the simulation of pyrite oxidation in the presence of 0.521 moles per liter pyrrhotite

time	Pyrite	O2(g)	Ca	SO_4	CO_3	Fe(2)	Fe(3)	FeSO4	$FeCO_3$	$CaSO_4$	pH
8.3	2.85	0.2	0.91	0.88	0.89	2.04e-15	8.0e-10	8.8e-16	1.1e-19	0.55	4.62
16.6	2.70	0.2	1.21	1.18	1.20	4.10e-15	1.4e-9	1.8e-15	1.4e-19	0.76	4.48
25.0	2.57	0.2	1.49	1.45	1.48	6.84e-15	2.1e-9	3.0e-15	1.8e-19	0.96	4.38
33.3	2.44	0.2	1.75	1.70	1.74	1.03e-14	3.2e-9	4.5e-15	2.1e-19	1.15	4.29
41.6	2.33	0.2	2.00	1.94	1.98	1.44e-14	4.8e-9	6.3e-15	2.4e-19	1.33	4.22
50.0	2.26	7.2e-46	2.14	2.08	2.12	2.21e-3	5.9e-9	9.7e-4	3.4e-8	1.43	4.19
58.2	2.26	1.6e-47	2.13	2.08	2.12	5.72e-3	5.9e-9	2.5e-3	8.7e-8	1.43	4.19
66.6	2.26	3.3e-48	2.13	2.08	2.11	8.44e-3	5.9e-9	3.7e-3	1.3e-7	1.43	4.19
74.9	2.26	1.2e-48	2.13	2.08	2.11	1.08e-2	5.9e-9	4.8e-3	1.6e-7	1.43	4.19
83.2	2.26	5.9e-49	2.13	2.08	2.11	1.30e-2	5.9e-9	5.7e-3	1.8e-7	1.43	4.19
91.5	2.26	3.3e-49	2.12	2.08	2.11	1.50e-2	5.8e-9	6.6e-3	2.3e-7	1.42	4.19
99.8	2.26	2.0e-49	2.12	2.08	2.11	1.69e-2	5.8e-9	7.4e-3	2.6e-7	1.42	4.19

Pyrrhotite with least Fe-deficient forms have hexagonal and orthorhombic (FeS) structures whereas those with greater iron deficiency have monoclinic symmetry (Arnold 1967, Janzen et al. 2000, Thomas et al. 2001). However in the pyrrhotite oxidation neither its crystal structure or trace metal content had a consistent or systematic effect on pyrrhotite oxidation rate (Janzen et al. 2000). The increased in surface area due to fracture on the surface may have fast rate of oxidation and created an acidic solution.

The formation of gypsum is low compared both pyrrhotite simulation with the 0.0521 moles/liter and the calcite simulation in section 6.2.1 due to the limitation of the oxygen level. Fixed level of oxygen was added in both simulations; however with an increase the level of the oxygen it is possible to see high concentration of gypsum produced and the excess pyrite is also oxidized.

4.2.5 Effect oxygenated water in the rate of pyrite oxidation

This simulation was done to see the effect of excess oxygen and water in the alum shale with low concentration of pyrite. The concentration of the pyrite was 0.3015 moles per liter in this simulation. The overall rate of pyrite oxidation with oxygen was 2.4e-11 moles per liter per second. The rate of pyrite destruction is low because of concentration is very low compared with the other simulations. At higher pH the oxidation of pyrite is controlled by oxygen and is slow compared with the oxidation by ferric iron at low pH. The oxidation continues as far as there is oxygen supply.

In subsurface cases the rate is limited by the physical control of the oxygen availability which is the diffusion of oxygen through the fracture zones and pore spaces. In the groundwater oxygen may be supplied both from advective transport and oxygen from recharge the unsaturated zone (Appelo and Postma 2005). Above the groundwater level on top of the saturated zone where there may be fracture zones for access of oxygen. However, with depth from the top of the saturated zone, the amount oxygen will decrease and the main oxidizing agent may be Fe^{3+} instead of oxygen.

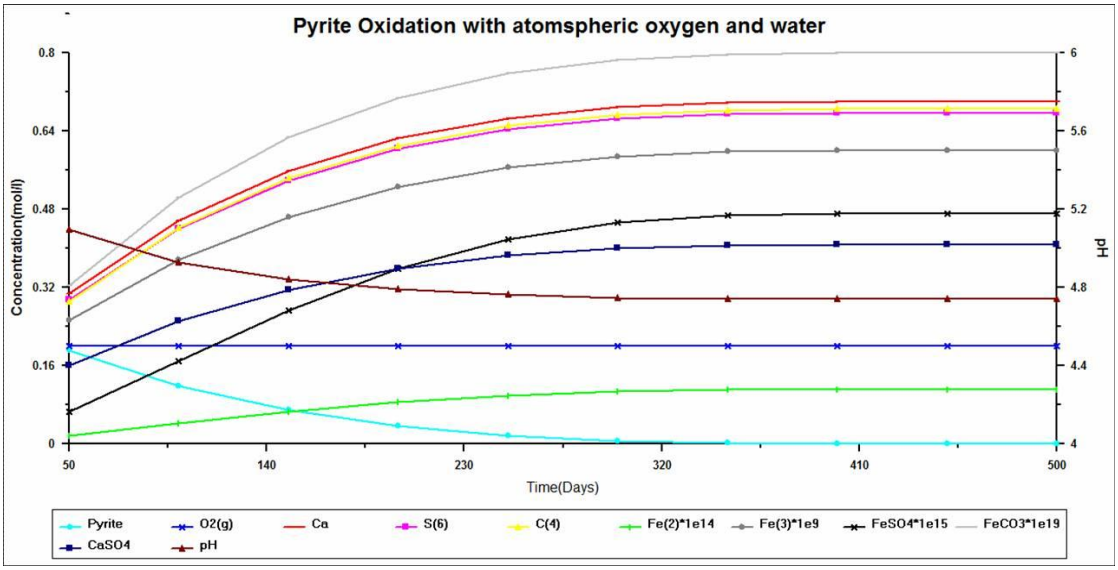

Figure 4-28 the simulation result of the pyrite oxidation with atmospheric level oxygen

Table 4-17 the simulation result of selected ions and minerals which changes significantly with time.

time	Pyrite	$O_2(g)$	Ca	SO_4	CO_3	Fe(2)	Fe(3)	$FeSO_4$	$FeCO_3$	$CaSO_4$	pH
50	0.191	0.2	0.307	0.294	0.292	0.0170	0.252	0.066	0.324	0.1591	5.10
100	0.118	0.2	0.457	0.440	0.442	0.042	0.376	0.170	0.504	0.2506	4.93
150	0.0687	0.2	0.559	0.539	0.543	0.066	0.464	0.274	0.627	0.3148	4.84
200	0.0364	0.2	0.625	0.604	0.610	0.085	0.526	0.360	0.708	0.3579	4.79
250	0.0165	0.2	0.666	0.644	0.651	0.099	0.566	0.418	0.758	0.3847	4.76
300	0.0057	0.2	0.689	0.665	0.673	0.107	0.588	0.452	0.785	0.3993	4.75
350	0.0011	0.2	0.698	0.675	0.683	0.110	0.598	0.467	0.797	0.4056	4.74
400	3e-5	0.2	0.700	0.677	0.685	0.111	0.600	0.471	0.799	0.4071	4.74
450	0.0	0.2	0.700	0.677	0.685	0.111	0.600	0.471	0.799	0.4071	4.74
500	0.0	0.2	0.700	0.677	0.685	0.111	0.600	0.471	0.799	0.4071	4.74

Note: the concentrations of Fe (2), Fe (3), $FeSO_4$, and $FeCO_3$ are multiplied by 10^{14}, 10^{9}, 10^{15} and 10^{19} respectively

In reality this may happen in the alum shale depicted in Fig 4-28 and 4-29 pictures from the Slemmestad sampling site). The alum shale rock which is exposed to the surface have reddish brown color on the surface and in between the layering of the shale in which it was possible for the water and oxygen to go through. The reddish brown color is due to iron oxide which is formed by the release of iron from the oxidation reaction.

Figure 4-29 Inside of one alum shale rock split into two where the hammer placed. The reddish brown color is due to iron oxide

Figure 4-30 water leaking through alum shale

In general the rate of pyrite oxidation and the resulting gypsum growth were dependent on the amount of calcite, pyrrhotite and oxygenated water in the alum shale. The calcite had inhibition effect on the rate of pyrite oxidation and pyrrhotite had catalytic effect.

4.3 Free swelling test

Free swelling test was done on one of the samples from the Konows gate and the black shale sample from the Slemmestad. The Slemmestad black shale sample did not show any swelling and the Konows gate sample showed only 1 cm^3 increase in volume. According to Brekke the volume should increase from 10 cm^3 to more than 13 cm^3 which is proved to contain expanding clay or smectite (Brekke and Selmer-Olsen 1965).

Chapter 5 Conclusion

The mineralogical analysis by XRD of the alum shale from the Konows gate and Slemmestad areas showed pyrite to be the most abundant sulfide mineral, with the highest concentration in the Konows gate samples. The black shale sample from Slemmestad had lower pyrite content, not detectable by the bulk XRD analysis. However, pyrite was detected in both reflected light petrographic and SEM microscopic analyses, as while as indirectly from the sulfur chemical analysis and XRD. The analysis using the reflected petrographic microscope also revealed pyrrhotite in the black shale sample. The occurrence of pyrrhotite was confirmed by SEM on the same specimen spot as mineral grains with the same chemical composition. Thus it was possible to see pyrrhotite using the SEM, but it may be difficult to differentiate the intensity from pyrite, chalcopyrite and sphalerite.

The XRF result elucidated the high concentration of pyrite in the Konows gate area compared with the Slemmestad area. The total sulfur content of the Konows gate area is twice that in the sample from Slemmestad. The ratio of the iron to total sulfur from the XRF is close to 1:2 which indicates that most of the sulfur is associated with iron in the pyrite form. The chemical analysis of the two samples from the Konows gate showed more than 0.01% monosulfides. The alum shale there should then have potential of swelling according to the NGI manual. The black shale sample had less than 0.01% monosulfides, and consequently no potential of swelling.

The microscopic mineralogical analysis successfully detected the minerals in smaller concentration which were not detected in the XRD, such as pyrrhotite, chalcopyrite, sphalerite, barite, dolomite and graphite. None of these were found by the bulk XRD analysis.

The presence of calcite in the alum shale inhibited the rate of pyrite oxidation by reducing the hydrogen ion concentration in the solution. The hydrogen ion concentration is reduced due to the formation of bicarbonate ions with the release of

carbonate ions from the dissolution of calcite. On the other hand calcite dissolution enhanced the growth of gypsum due to increased calcium ions in the solution.

The pyrrhotite had a reverse effect than that of calcite. It oxidized very fast and acidified the solution there by catalyzing the pyrite oxidation. During the oxidation the oxygen concentration goes down very fast and the pyretic oxidation by the ferric iron, which is very fast, takes over. With low pyrite input and a constant supply of oxygen the processes of pyrite oxidation is very slow.

The swelling of the alum shale is caused by decrease in density due to change in mineralogical composition which occurs mainly through the development of gypsum when pyrite is oxidized together with calcite dissolution. The rate and amounts depend on the mineralogical composition of the shale and the level of oxygenated water coming in contact with the alum shale. Free swelling test result showed no expanding clay or smectite in the sample from the Konows gate and the black shale sample of the Slemmestad.

References

Aagaard, P. and Helgeson, H.G. 1982. Thermodynamic and kinetic constraints on reaction rates among minerals and aqueous solutions. I. Theoretical considerations. *American Journal of Science* 282, 237-285.

Appelo, C.A.J. and Postma, D. 2005. *Geochemistry, groundwater and pollution*. 2nd edition ed: A.A. Balkema publishers. 649 pp.

Arnold, R.G. 1967. Range in composition and structure of 82 natural terrestrial pyrrhotites. *Canadian Mineralogist* 9, 31-50.

Bastiansen, R., Moum, J. and Rosenqvist, I.T.H. 1957. Bidrag til belsning av visse bygningstikniske problemer ved Oslo-området alunskifere. *Norwegian Geotechnical Institute* 22, 69.

Belzile, N., Chen, Y., Cai, M. and Y, L. 2004. A review on pyrrhotite oxidation *Journal of Geochemical Exploration* 84, 65-76.

Bharati, S., Patience, R.L., Larter, S.R., Standen, G. and Poplett, I.J.F. 1996. Elucidation of the Alum Shale Kerogen structure using a multi-disciplinary approach. *Organic Geochemistry* 23, No. 11/12, 1043-1058.

Boggs, S.J., ed. 2006. *Principles of Sedimentology and Stratigraphy*. Fourth utg. Upper Saddle River, New Jersey: Pearson Education, Inc.

Brekke, T. and Selmer-Olsen, R. 1965. Stability problems in underground constructions caused by montmorillonite-carrying joints and faults. *Engineering Geology* 1 (1), 3-19.

Czerewko, M.A., Cripps, J.C., Reid, J.M. and Duffell, C.G. 2003. Sulfur species in geological materials - sources and quantification. *Cement and concrete composites* 25 (7), 657-671.

Deer, W.A., Howie, R.A. and Zussman, J. 1966. *An Introduction to the Rock-Forming Minerals*, London and Harlow: LONGMANS. 528 pp.

Hagelia, P., Sibbick, R.G., Crammond, N.J. and Larsen, C.K. 2003. Thaumasite and secondary calcite in some Norwegian concretes. *Cement and concrete composites* 25 (8), 1131-1140.

Janzen, M.P., Nicholson, R.V. and Scharer, J.M. 2000. Pyrrhotite reaction kinetics: reaction rates for oxidation by oxygen, ferric iron, and for non-oxidative dissolution. *Geochimica et cosmchimica acta* 64, 1511-1522.

Larsen, B.T. and Olaussen, S. *The Oslo Region: A study in classical Palaeozoic Geology*. Norsk Geologisk Forening 2005 Accsessed.

Lowson, R.T. 1982. Aqueous Oxidation of Pyrite by Molecular Oxygen. *American Chemical Society* 82, N0. 5, 461 - 497.

Moore, D.M. and Reynolds, R.C. 1989. *X-Ray Diffraction and the Identification and Analysis of Clay Minerals*, New York: Oxford University Press, Inc. 332 pp.

Moum, J. and Rosenqvist, I.T. 1959. Sulphate attack on concrete in the Oslo region. *Journal of American Concrete Institute* 56, 18-26.

Nesse, W.D. 2004. *Introduction to Optical Mineralogy*. third edition ed, New York: Oxford University Press. 348 pp.

Parkhurst, D.L. and Appelo, C.A.J. *User's Guide to PHREEQC (Version 2)--A Computer Program for Speciation, Batch-Reaction, One-Dimensional Transport, and Inverse Geochemical Calculations*. USGS 1999 Accsessed. Available at http://wwwbrr.cr.usgs.gov/projects/GWC_coupled/phreeqc/html/final-1.html.

Pofsai, M. and Dodonay, I. 1990. Pyrrhotite superstructures: Part I. Fundamentals structures of the NC (N=2, 3, 4 and 5) type. *European journal of mineralogy* 2, 525-528.

Ramberg, I.B., Bryhni, I. and Nøttvedt, A. 2006. *Landet Blir Til Norges geologi*, Trondheim: Norsk Geologisk Forening. 608 pp.

Rimstidt, J.D. and Vaughan, D.J. 2003. Pyrite oxidation: A state-of-the-art assessment of the reaction mechanism. *Geochimica et cosmochimica acta* 67 (5), 873-880.

Roberts, W.L., Rapp, G.R. and Weber, J. 1974. Encyclopedia of Minerals, 693.

Steger, H.F. and Desjardins, L.E. 1978. Oxidation of sulphide minerals: 4. Pyrite, chalcopyrite, and pyrrhotite. *Chemical geology* 23, 225-237.

Steinmetz, R., ed. 1984. *Scanning Electron Microscopy Atlas*, *Method in Exploration series*: The American Association of Petroleum Geologists.

Thomas, J.E., Skinner, W.M. and Smart, R.S.C. 2001. A mechanism to explain sudden changes in rates and products for pyrrhotite dissolution in acid solution. *Geochimica et cosmchimica acta* 65, 1-12.

Thomas, J.E., Smart, R.S.C. and Skinner, W.M. 2000. Kinetics factors for oxidative and non-oxidative dissolution of iron sulfides. *Minerals Engineering* 10-11, 1149-1159.

Vaughan, D.J. and Craig, J.R. 1978. Mineral Chemistry of Metal Sulphides. *Cambridge university press*, 493.

Ward, J.C. 1970. The structure and properties of some iron sulphides. *Review pure applied chemistry* 20, 175-206.

Williamson, M.A. and Rimstidt, J.D. 1994. The kinetics and electrochemical rate-determining step of aqueous pyrite oxidation. *Geochimica et cosmchimica acta* 58, 5443-5454.

Appendix - A

XRD diffractograms, pattern list and view and peak list

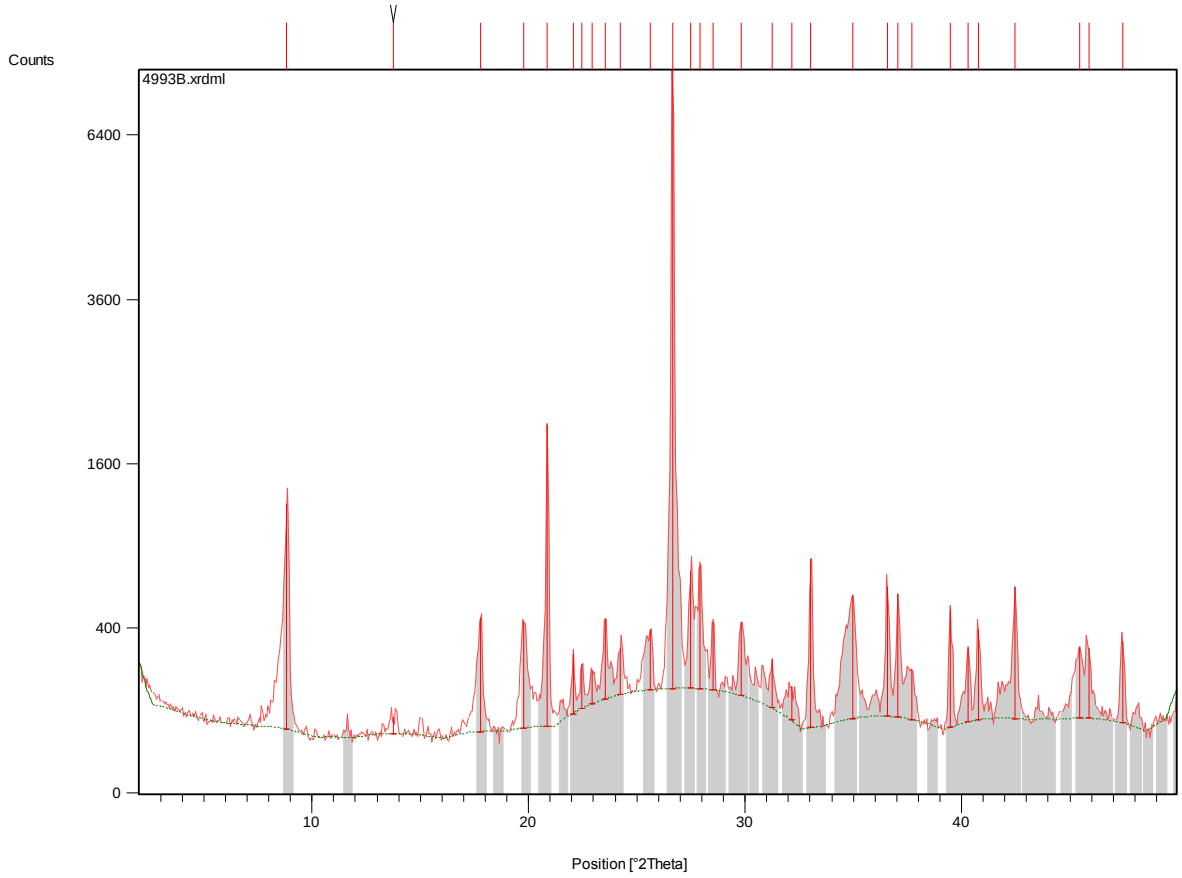

Figure A-1 Diffractogram of sample SL from the Slemmestad area

Compound Name	Ref. Code	Empirical Formula	Score
Quartz, syn	46-1045	Si O2	64
Muscovite-2\ITM\RG#1	06-0263	K Al2 (Si3 Al) O10 (O H , F)2	55
Pyrite	24-0076	Fe S2	54
Bernalite	46-1436	Fe +3 (O H)3	35
Microcline	01-0705	K Al Si3 O8	39
Gypsum	03-0044	Ca S O4 !2 H2 O	23

Table A-1 Minerals identified in the SL sample of the Slemmestad area

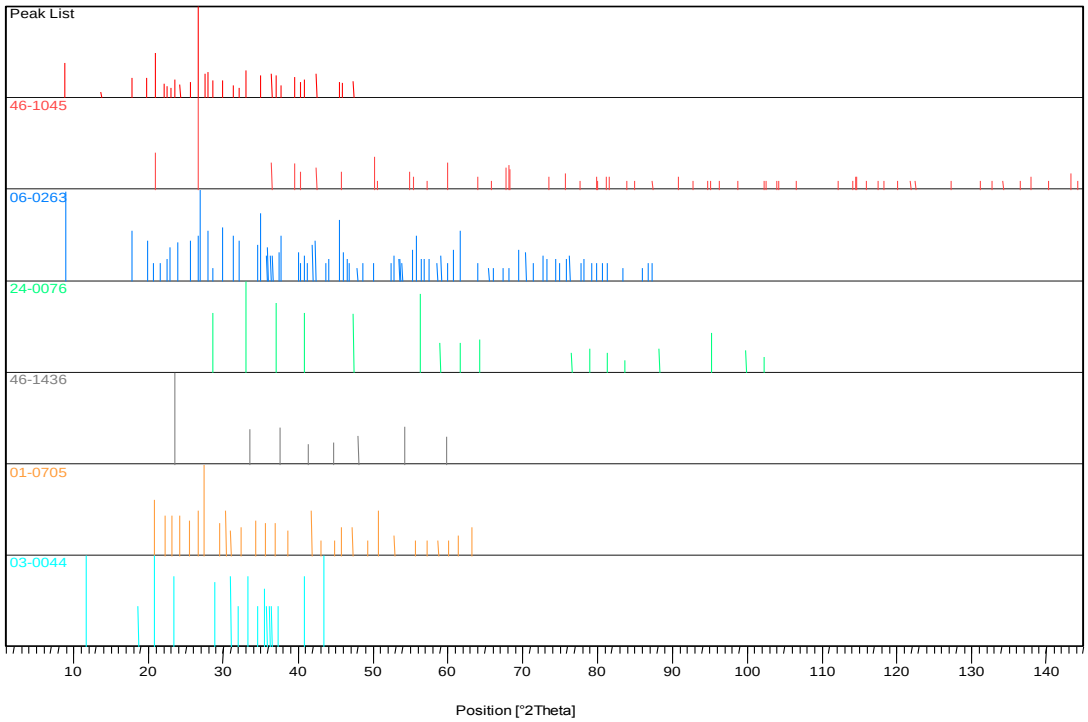

Figure A-2 Pattern of the peaks and identified minerals from the sample SL

Pos. [°2Th.]	d-spacing [Å]	Matched by	Height [cts]	FWHM [°2Th.]
8,8380	10,00570	06-0263	1177,88	0,1771
13,7707	6,43072		36,06	0,3542
17,7719	4,99091	06-0263	400,03	0,1771
19,7610	4,49279	06-0263	373,59	0,2952
20,8632	4,25787	46-1045; 06-0263; 01-0705; 03-0044	1942,75	0,1771
22,0492	4,03145	01-0705	196,84	0,1771
22,4706	3,95680	06-0263	141,88	0,1771
22,9381	3,87719	06-0263; 01-0705	105,78	0,1771
23,5286	3,78121	46-1436; 03-0044	322,91	0,1771
24,2512	3,67017	01-0705	171,20	0,1771
25,6239	3,47657	06-0263; 01-0705	242,29	0,4133
26,6517	3,34480	46-1045; 06-0263; 01-0705	7972,98	0,1771
27,4896	3,24472	01-0705	568,04	0,1771
27,9301	3,19454	06-0263	630,60	0,1771
28,5269	3,12905	06-0263; 24-0076	291,76	0,1771
29,8206	2,99618	06-0263	296,46	0,1771
31,2437	2,86288	06-0263; 01-0705; 03-0044	161,44	0,1771
32,1449	2,78465	06-0263; 03-0044	91,52	0,3542
33,0412	2,71113	24-0076	746,83	0,1771
34,9627	2,56641	06-0263	499,47	0,2362
36,5746	2,45692	46-1045; 06-0263; 03-0044	544,26	0,1771
37,0702	2,42521	24-0076; 01-0705; 03-0044	503,06	0,1771
37,6969	2,38632	06-0263; 46-1436	147,49	0,4133
39,4965	2,28164	46-1045	434,16	0,1771
40,3147	2,23720	46-1045; 06-0263	236,74	0,1771
40,7681	2,21336	06-0263; 24-0076; 03-0044	317,46	0,1771
42,4699	2,12852	46-1045; 06-0263	545,54	0,2362
45,4485	1,99571	06-0263	235,11	0,4133
45,8651	1,97855	46-1045; 06-0263; 01-0705	228,81	0,3542
47,4296	1,91529	24-0076; 01-0705	269,60	0,2160

Table A-2 the peaks list and the mineral matched by code

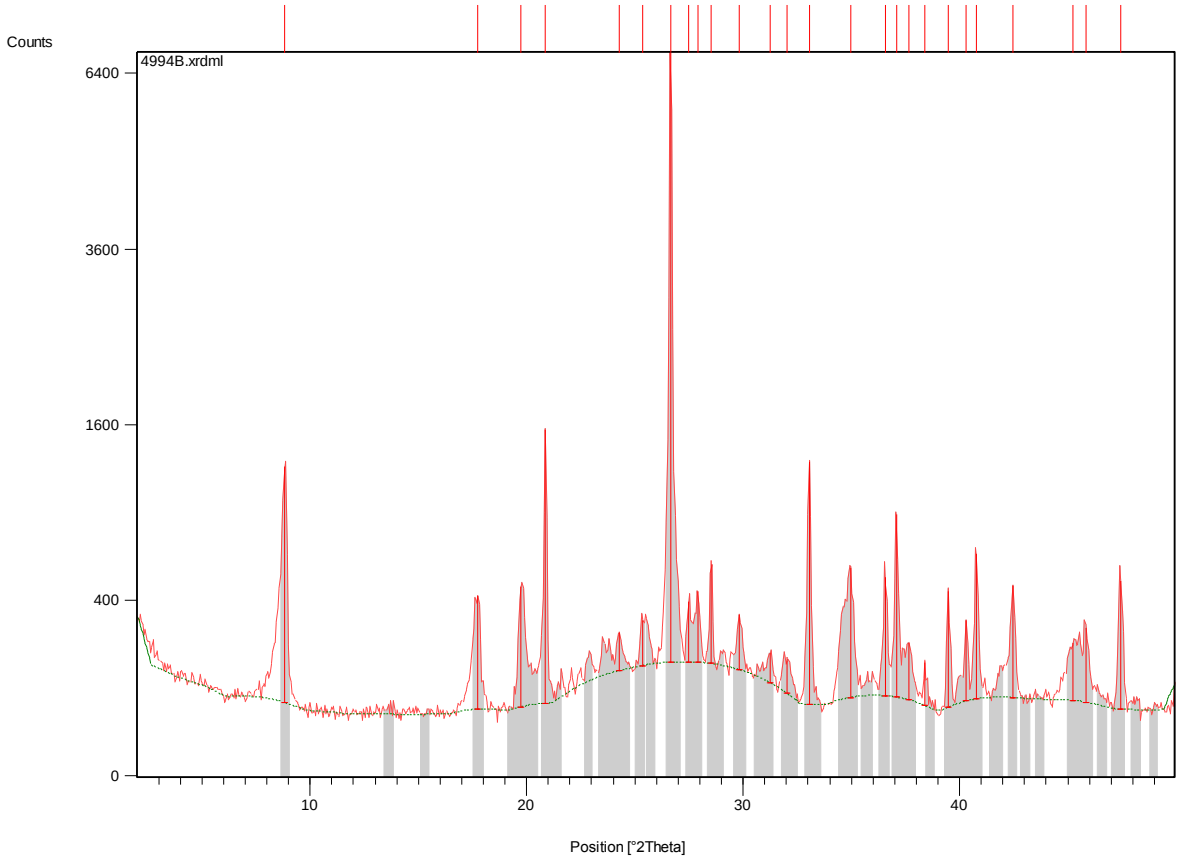

Figure A-3 Diffractogram of sample KS3 from the Konows gate area

Compound Name	Ref. Code	Empirical Formula	Score
Quartz, syn	46-1045	Si O2	66
Pyrite, syn	06-0710	Fe S2	57
Illite-2\ITM\RG#1 [NR]	26-0911	(K , H3 O) Al2 Si3 Al O10 (O H)2	36
Orthoclase, Ba-rich	19-0002	(K , Ba , Na) (Si , Al)4 O8	35
Glauconite-1\ITM\RG, Cr-rich [NR]	45-1337	K (Al , Cr , Mg)2 (Si , Al)4 O10 (O H)2	23

Table A-3 Minerals identified in the KS3 sample of the Konows gate area

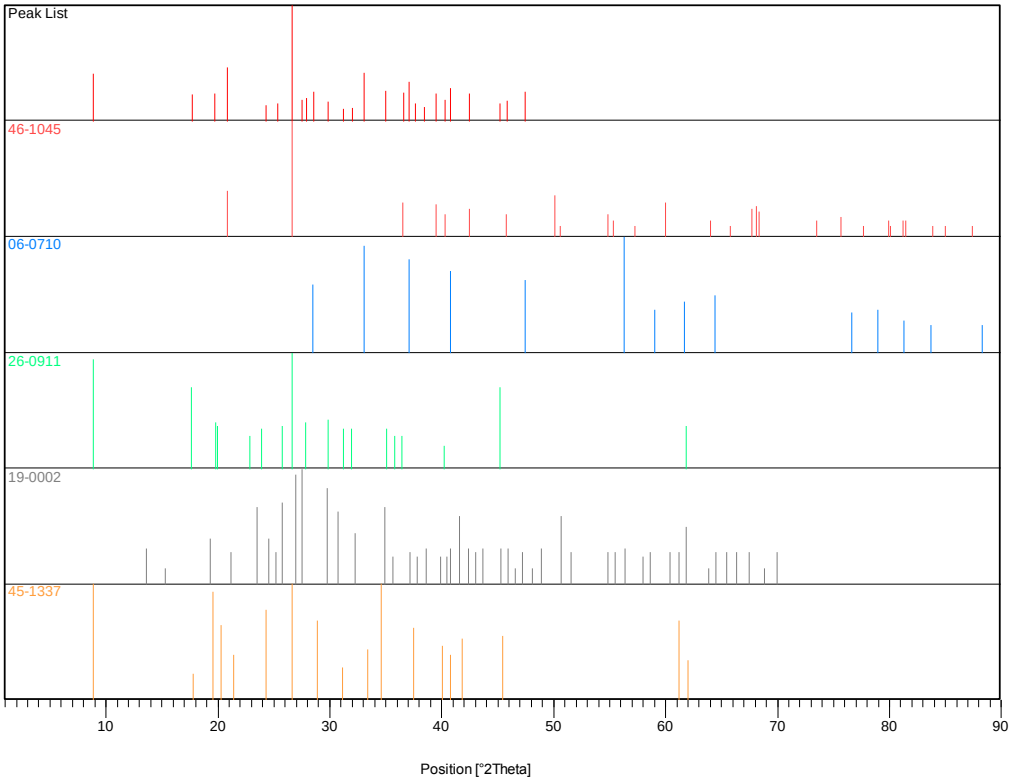

Figure A-4 Pattern of the peaks and identified minerals from the sample KS3

Pos. [°2Th.]	d-spacing [Å]	Matched by	Height [cts]	FWHM [°2Th.]
8,8255	10,01989	26-0911; 45-1337	1172,69	0,1771
17,7403	4,99972	26-0911; 45-1337	361,19	0,2952
19,7494	4,49540	26-0911; 45-1337	405,66	0,2362
20,8637	4,25776	46-1045	1484,25	0,1771
24,2618	3,66858	45-1337	123,74	0,2362
25,3698	3,51081	19-0002	156,07	0,2362
26,6497	3,34504	46-1045; 26-0911; 45-1337	6914,71	0,1771
27,4818	3,24562	19-0002	225,03	0,1771
27,9115	3,19662	26-0911	273,30	0,1771
28,5292	3,12880	06-0710	439,33	0,1771
29,8300	2,99526	26-0911; 19-0002	192,86	0,1771
31,2467	2,86261	26-0911; 45-1337	83,84	0,2362
32,0134	2,79579	26-0911	94,25	0,3542
33,0518	2,71029	06-0710	1218,22	0,2362
34,9682	2,56602	26-0911; 19-0002	483,63	0,2362
36,5670	2,45741	46-1045; 26-0911	428,27	0,1771
37,0878	2,42409	06-0710; 19-0002	806,09	0,1771
37,6750	2,38765	19-0002; 45-1337	155,30	0,2952
38,4094	2,34367	19-0002	103,35	0,1771
39,4913	2,28192	46-1045	382,14	0,1771
40,3200	2,23692	46-1045; 26-0911; 19-0002	241,00	0,1500
40,7727	2,21312	06-0710; 19-0002; 45-1337	565,59	0,1771
42,4701	2,12851	46-1045; 19-0002	391,30	0,2362
45,2374	2,00453	26-0911; 19-0002	156,23	0,3542
45,8414	1,97952	46-1045; 19-0002	216,03	0,1771
47,4456	1,91468	06-0710; 19-0002	435,67	0,2160

Table A-4 the peaks list and the mineral matched by code from sample KS3

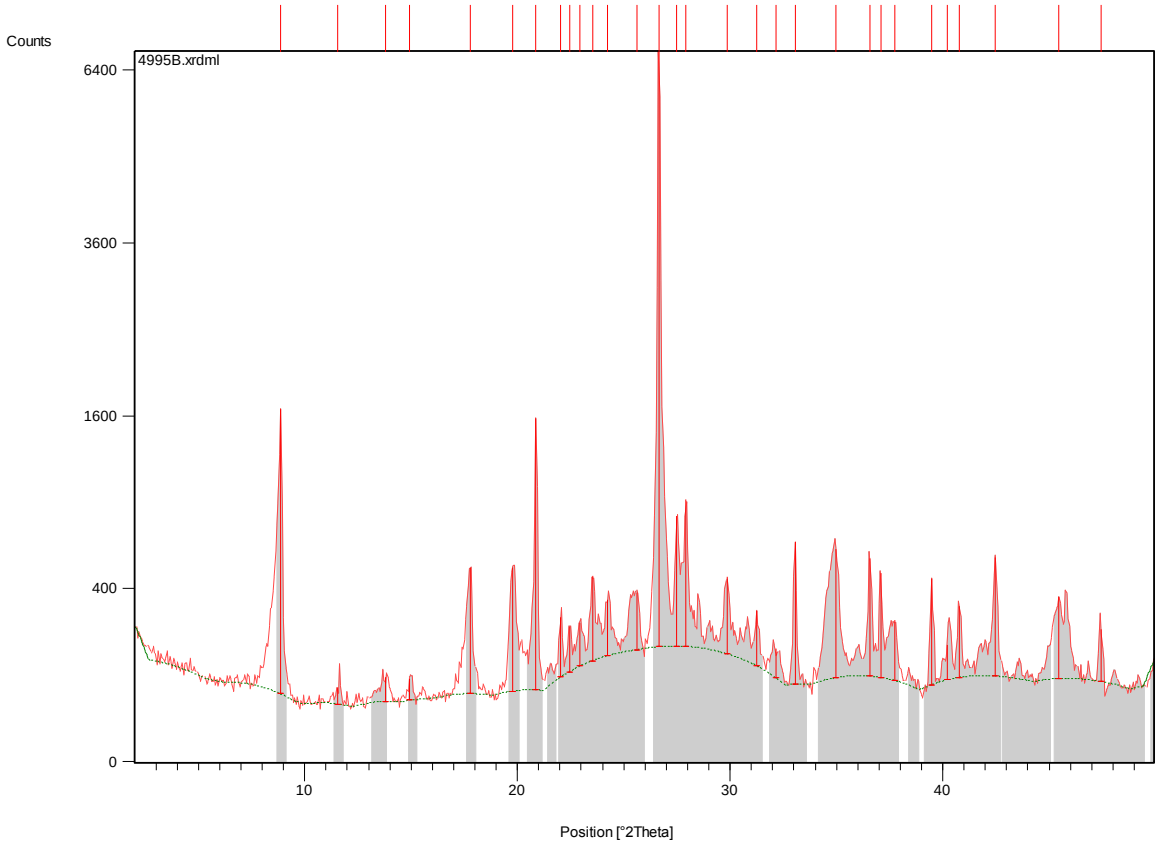

Figure A-5 Diffractogram of sample SW from the Slemmestad area

Compound Name	Ref. Code	Empirical Formula	Score
Quartz, syn	46-1045	Si O2	62
Muscovite-2\ITM\RG#1	06-0263	K Al2 (Si3 Al) O10 (O H , F)2	56
Microcline	01-0705	K Al Si3 O8	38
Gypsum, syn	33-0311	Ca S O4 !2 H2 O	20
Pyrite, syn	06-0710	Fe S2	47
Sanidine, high, syn	10-0353	K Al Si3 O8	42

Table A-5 Minerals identified in the SW sample of the Slemmestad area

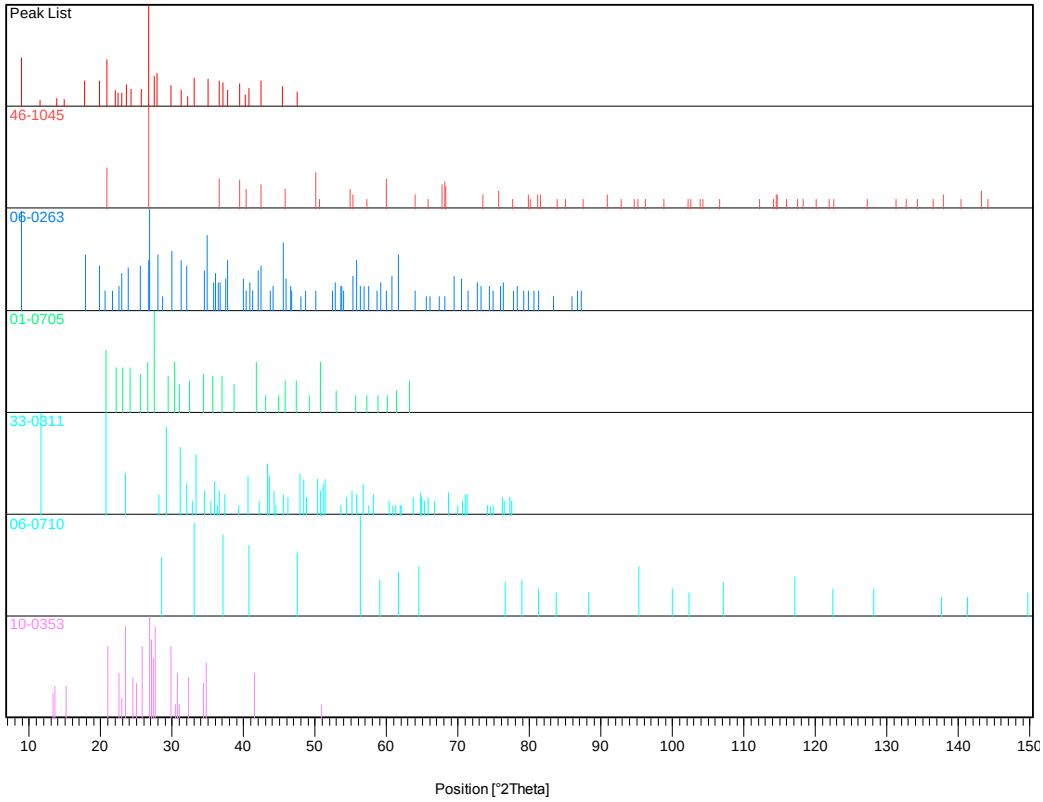

Figure A-6 Pattern of the peaks and identified minerals from the sample SW

Pos. [°2Th.]	d-spacing [Å]	Matched by	Height [cts]	FWHM [°2Th.]
8,8462	9,99640	06-0263	1603,70	0,1771
11,5490	7,66236	33-0311	30,93	0,3542
13,7852	6,42401	10-0353	48,14	0,4723
14,9322	5,93302	10-0353	40,87	0,3542
17,7672	4,99223	06-0263	442,52	0,2362
19,7830	4,48786	06-0263	440,42	0,2952
20,8710	4,25631	46-1045; 06-0263; 01-0705; 33-0311; 10-0353	1513,95	0,2362
22,0362	4,03380	01-0705	182,83	0,1771
22,4395	3,96220	06-0263; 10-0353	135,89	0,1771
22,9250	3,87938	06-0263; 01-0705; 10-0353	135,84	0,2362
23,5293	3,78111	33-0311; 10-0353	327,46	0,1771
24,2549	3,66961	01-0705	201,84	0,1771
25,6302	3,47574	06-0263; 01-0705; 10-0353	218,53	0,1771
26,6525	3,34470	46-1045; 06-0263; 01-0705; 10-0353	6902,50	0,1771
27,4948	3,24411	01-0705; 10-0353	628,91	0,1771
27,9311	3,19442	06-0263; 33-0311	743,03	0,1771
29,8455	2,99374	06-0263; 10-0353	302,46	0,1771
31,2681	2,86070	06-0263; 01-0705; 33-0311	183,37	0,1771
32,1601	2,78337	06-0263; 33-0311; 10-0353	77,37	0,4723
33,0469	2,71067	06-0710	566,95	0,1771
34,9678	2,56604	06-0263; 10-0353	513,67	0,2952
36,5733	2,45700	46-1045; 06-0263; 33-0311	455,86	0,1771
37,0830	2,42440	01-0705; 06-0710	382,92	0,1181
37,7631	2,38228	06-0263	181,04	0,4133
39,4802	2,28254	46-1045; 33-0311	369,25	0,1771
40,1965	2,24350	46-1045; 06-0263	94,46	0,2362
40,7724	2,21313	06-0263; 33-0311; 06-0710	230,56	0,1771
42,4793	2,12808	46-1045; 06-0263	462,48	0,2362
45,4623	1,99514	06-0263; 33-0311	270,62	0,3542
47,4363	1,91503	01-0705; 06-0710	150,40	0,2160

Table A-6 the peaks list and the mineral matched by code from sample SW

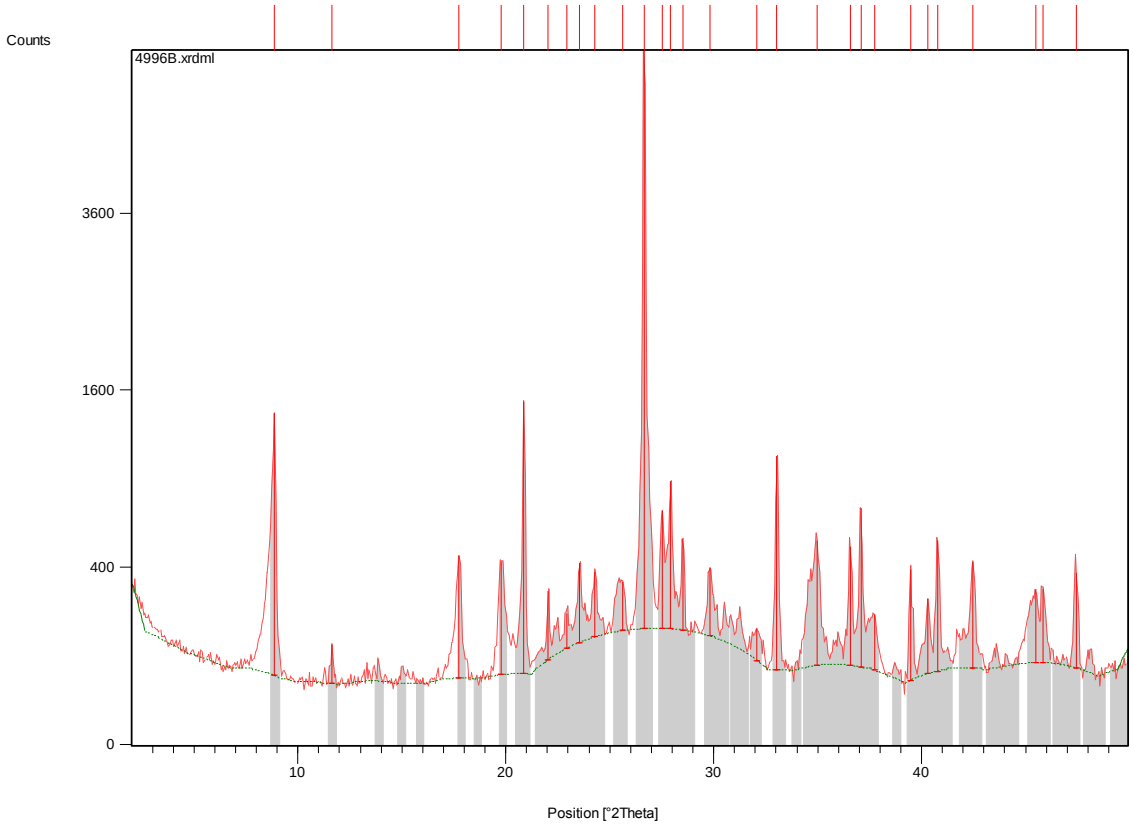

Figure A-7 Diffractogram of sample SM from the Slemmestad area

Compound Name	Ref. Code	Empirical Formula	Score
Quartz, syn	46-1045	Si O2	65
Pyrite, syn	06-0710	Fe S2	58
Muscovite-2\ITM\RG#1	06-0263	K Al2 (Si3 Al) O10 (O H , F)2	54
Orthoclase	08-0048	K (Al , Fe) Si2 O8	50
Albite, ordered	20-0554	Na Al Si3 O8	42
Gypsum	03-0044	Ca S O4 !2 H2 O	28

Table A-5 Minerals identified in the SM sample of the Slemmestad area

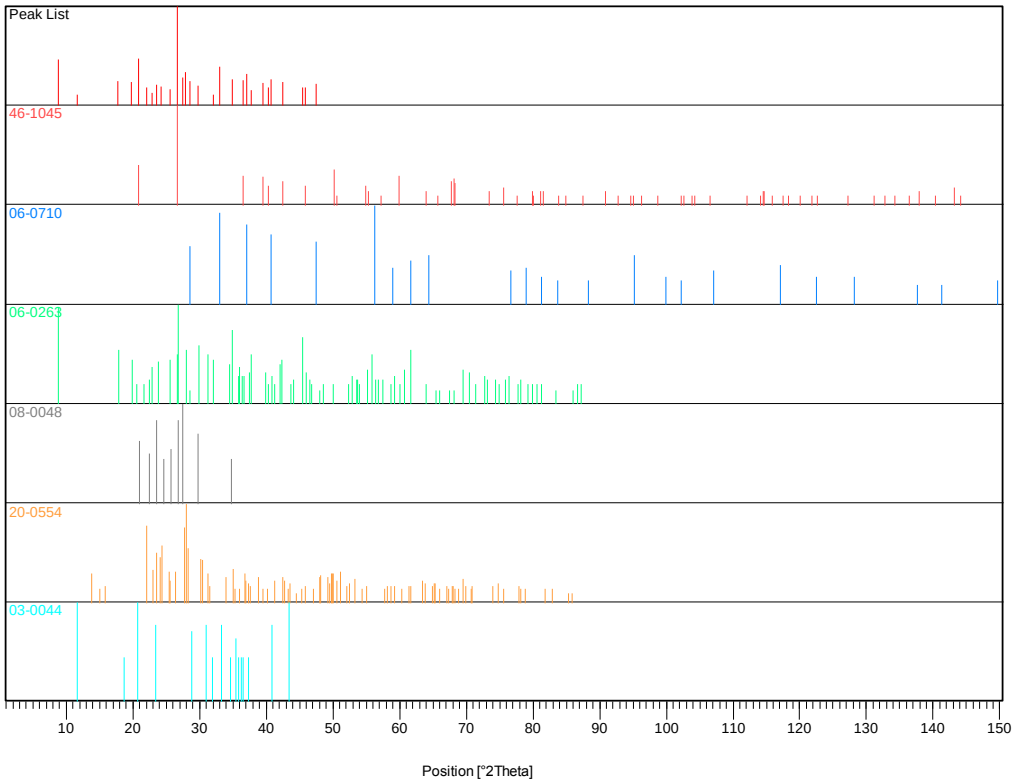

Figure A-8 Pattern of the peaks and identified minerals from the sample SM

Pos. [°2Th.]	d-spacing [Å]	Matched by	Height [cts]	FWHM [°2Th.]
8,8465	9,99613	06-0263	1346,17	0,1771
11,6184	7,61676	03-0044	79,43	0,1771
17,7536	4,99600	06-0263	397,29	0,2362
19,7697	4,49085	06-0263	362,63	0,2362
20,8680	4,25690	46-1045; 08-0048; 03-0044	1437,01	0,1771
22,0400	4,03311	20-0554	211,28	0,1771
22,9185	3,88048	06-0263; 20-0554	103,58	0,1771
23,5423	3,77904	08-0048; 20-0554; 03-0044	288,51	0,1771
24,2657	3,66801	20-0554	229,74	0,1771
25,6244	3,47651	06-0263; 08-0048; 20-0554	173,11	0,4723
26,6538	3,34453	46-1045; 06-0263; 08-0048; 20-0554	6320,65	0,1771
27,5048	3,24295	08-0048	524,89	0,1771
27,9311	3,19442	06-0263; 20-0554	713,91	0,1771
28,5195	3,12984	06-0710; 06-0263; 20-0554	377,86	0,1771
29,8193	2,99631	06-0263; 08-0048	249,11	0,2362
32,0938	2,78897	06-0263; 03-0044	84,12	0,3542
33,0462	2,71073	06-0710	995,74	0,1771
34,9734	2,56564	06-0263; 20-0554	449,07	0,2362
36,5723	2,45707	46-1045; 06-0263; 20-0554; 03-0044	420,47	0,1771
37,0761	2,42483	06-0710; 20-0554; 03-0044	636,75	0,1181
37,7293	2,38434	06-0263; 20-0554	147,62	0,3542
39,4892	2,28204	46-1045; 20-0554	339,58	0,1771
40,3200	2,23692	46-1045; 06-0263; 20-0554	207,00	0,1500
40,7712	2,21320	06-0710; 06-0263; 03-0044	459,39	0,1771
42,4761	2,12823	46-1045; 06-0263; 20-0554	352,49	0,2362
45,4774	1,99451	06-0263; 20-0554	220,77	0,4133
45,8520	1,97908	46-1045; 06-0263; 20-0554	221,26	0,1771
47,4396	1,91491	06-0710	299,48	0,2160

Table A-8 the peaks list and the mineral matched by code from sample SM

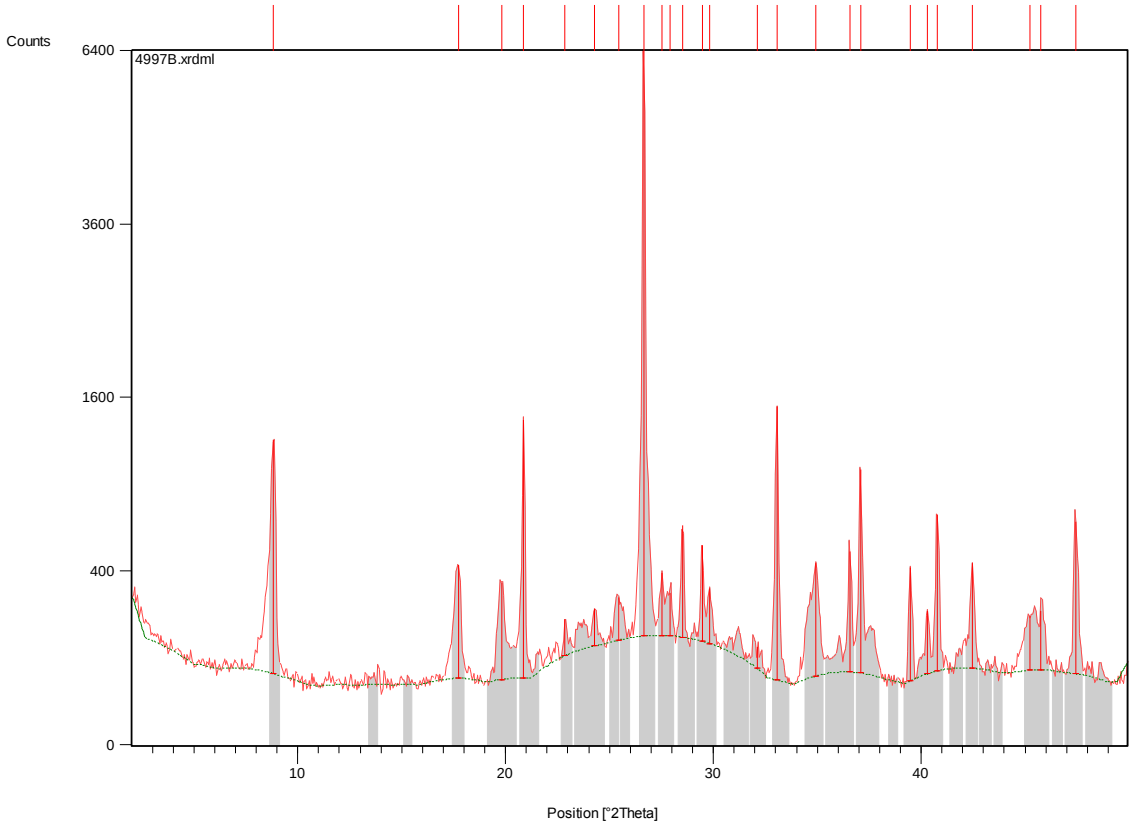

Figure A-9 Diffractogram of sample KS1 from the Konows gate area

Pattern List: KS1

Compound Name	Ref. Code	Empirical Formula	Score
Quartz, syn	46-1045	Si O2	68
Pyrite	24-0076	Fe S2	62
Illite-2\ITM\RG#1 [NR]	26-0911	(K , H3 O) Al2 Si3 Al O10 (O H)2	33
Orthoclase, Ba-rich	19-0002	(K , Ba , Na) (Si , Al)4 O8	35
Calcite, syn	05-0586	Ca C O3	39
Glauconite-1\ITM\RG, Cr-rich [NR]	45-1337	K (Al , Cr , Mg)2 (Si , Al)4 O10 (O H)2	22

Table A-9 Minerals identified in the KS1 sample of the Konows gate area

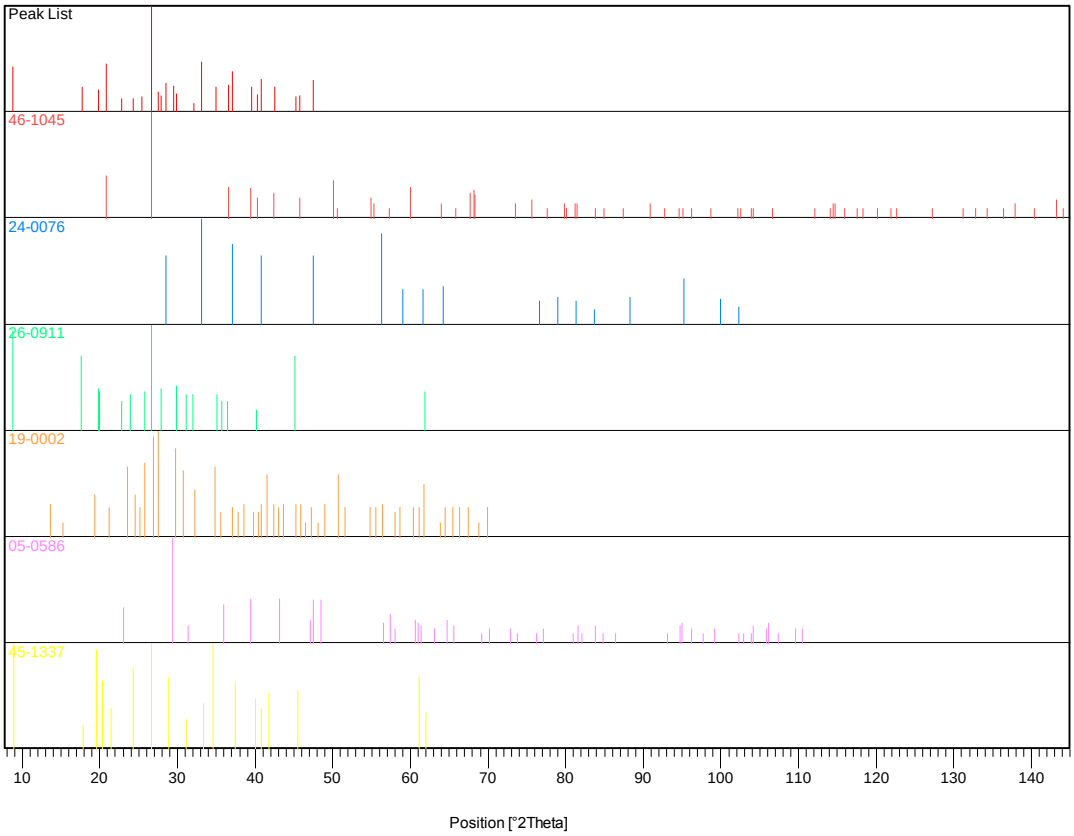

Figure A-10 Pattern of the peaks and identified minerals from the sample KS1

Pos. [°2Th.]	d-spacing [Å]	Matched by	Height [cts]	FWHM [°2Th.]
8,8256	10,01975	26-0911; 45-1337	1172,44	0,2362
17,7286	5,00299	26-0911; 45-1337	371,93	0,2362
19,7974	4,48462	26-0911; 45-1337	290,99	0,2952
20,8583	4,25886	46-1045	1348,49	0,1771
22,8628	3,88981	26-0911; 05-0586	106,49	0,1771
24,2929	3,66396	45-1337	114,98	0,1771
25,4508	3,49983	19-0002	145,14	0,4723
26,6460	3,34549	46-1045; 26-0911; 45-1337	6466,57	0,1771
27,5091	3,24246	19-0002	233,64	0,1771
27,8989	3,19804	26-0911	151,27	0,1771
28,5153	3,13029	24-0076	488,77	0,1771
29,4549	3,03255	05-0586	386,54	0,1181
29,8325	2,99501	26-0911; 19-0002	189,97	0,1771
32,1060	2,78793	26-0911; 19-0002	48,92	0,4723
33,0542	2,71009	24-0076	1466,38	0,2362
34,9295	2,56877	26-0911; 19-0002	378,18	0,2362
36,5681	2,45734	46-1045; 26-0911	429,18	0,1771
37,0859	2,42421	24-0076; 19-0002	937,13	0,1771
39,4879	2,28211	46-1045; 05-0586	364,64	0,1771
40,3171	2,23707	46-1045; 26-0911; 19-0002	171,48	0,1771
40,7788	2,21280	24-0076; 19-0002; 45-1337	632,66	0,1771
42,4708	2,12848	46-1045; 19-0002	361,82	0,1771
45,2411	2,00438	26-0911; 19-0002	148,17	0,3542
45,7673	1,98255	46-1045; 19-0002	163,84	0,3542
47,4486	1,91457	24-0076; 19-0002; 05-0586	593,65	0,2160

Table A-10 the peaks list and the mineral matched by code from sample KS1

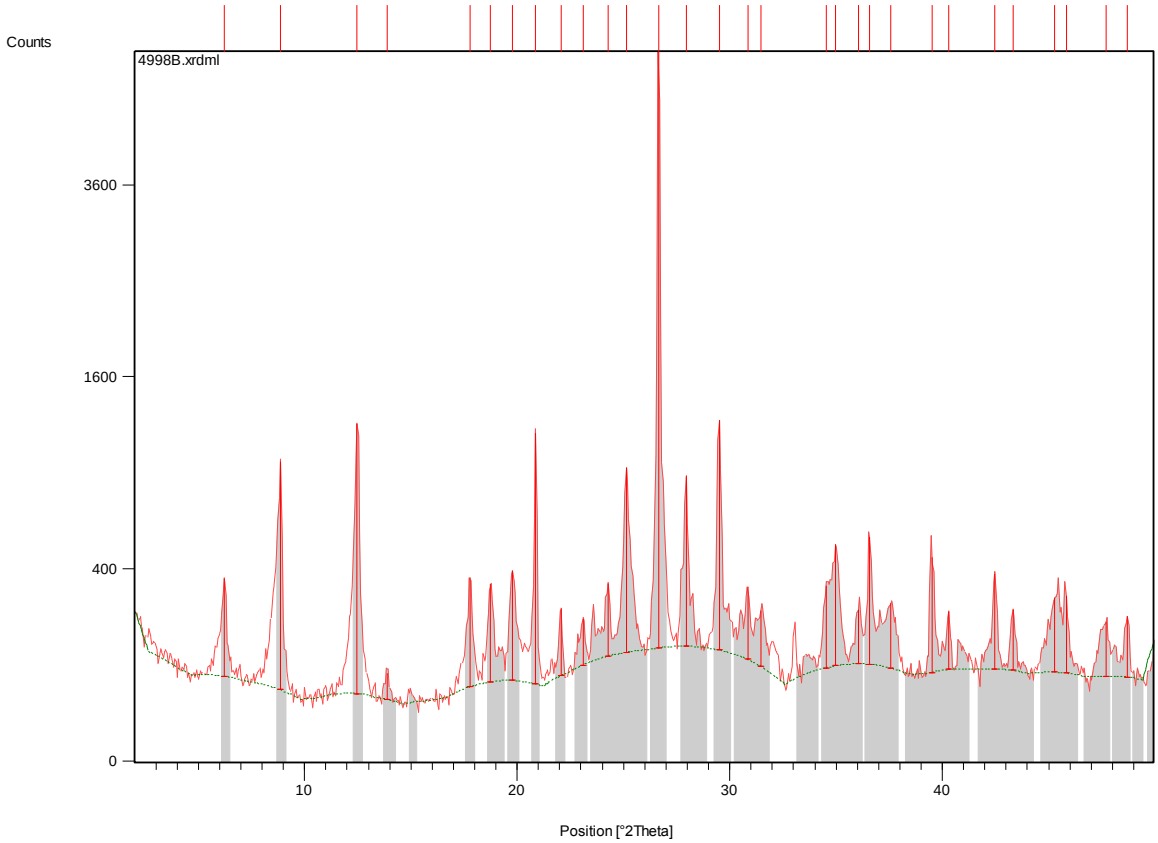

Figure A-11 Diffractogram of sample BS from the Slemmestad area

Compound Name	Ref. Code	Empirical Formula	Score
Quartz, syn	46-1045	Si O2	65
Clinoclore, ferroan	07-0076	(Mg2.8 Fe1.7 Al1.2) (Si2.8 Al1.2) O10 (O H)8	63
Calcite	24-0027	Ca C O3	47
Albite, Ca-rich, ordered	41-1480	(Na , Ca) Al (Si , Al)3 O8	43
Ankerite	12-0088	Ca (Mg0.67 Fe0.33 +2) (C O3)2	30
Muscovite-3\ITT\RG	07-0042	(K , Na) (Al , Mg , Fe)2 (Si3.1 Al0.9) O10 (O H)2	58

Table A-11 Minerals identified in the BS sample of the Slemmestad area

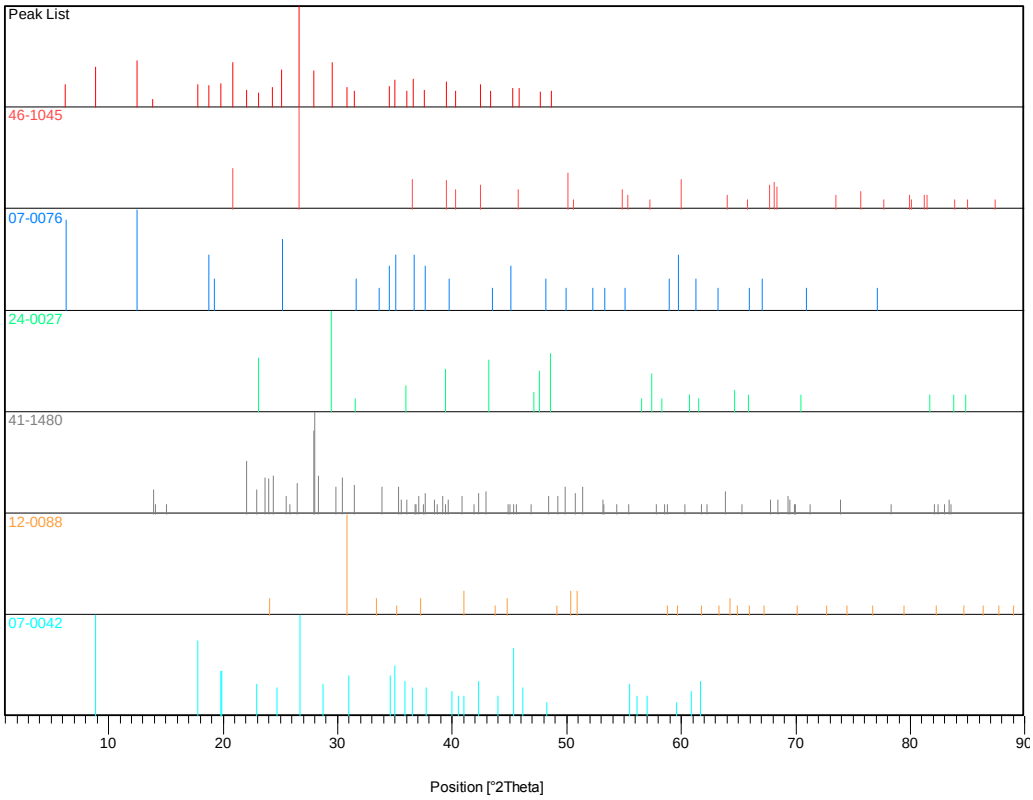

Figure A-12 Pattern of the peaks and identified minerals from the sample BS

Pos. [°2Th.]	d-spacing [Å]	Matched by	Height [cts]	FWHM [°2Th.]
6,2155	14,22038	07-0076	283,82	0,1771
8,8422	10,00103	07-0042	916,35	0,1771
12,4722	7,09717	07-0076	1188,90	0,2362
13,8729	6,38360	41-1480	42,79	0,3542
17,7874	4,98659	07-0042	306,17	0,1771
18,7536	4,73181	07-0076	272,93	0,2362
19,7675	4,49134	07-0042	323,65	0,2362
20,8575	4,25902	46-1045	1104,22	0,1771
22,0509	4,03115	41-1480	176,33	0,1771
23,1009	3,85025	24-0027; 41-1480; 07-0042	119,78	0,2362
24,2613	3,66866	41-1480; 12-0088	222,34	0,1771
25,1351	3,54306	07-0076	803,28	0,2362
26,6490	3,34513	46-1045; 41-1480; 07-0042	5602,55	0,1771
27,9501	3,19229	41-1480	739,11	0,1771
29,5025	3,02776	24-0027	1131,22	0,1771
30,8392	2,89950	12-0088; 07-0042	219,15	0,1771
31,4606	2,84364	07-0076; 24-0027; 41-1480	149,95	0,3542
34,5294	2,59762	07-0076; 07-0042	241,20	0,1771
34,9906	2,56443	07-0076; 12-0088; 07-0042	413,41	0,2362
36,0493	2,49151	24-0027; 41-1480; 07-0042	146,92	0,1771
36,5787	2,45665	46-1045; 07-0076; 41-1480; 07-0042	446,15	0,1771
37,5557	2,39496	07-0076; 41-1480; 07-0042	176,41	0,3542
39,5117	2,28079	46-1045; 24-0027; 41-1480	365,63	0,1771
40,3115	2,23737	46-1045	150,96	0,1771
42,4772	2,12818	46-1045; 41-1480; 07-0042	290,02	0,2362
43,3099	2,08917	07-0076; 24-0027	161,62	0,2362
45,2828	2,00263	07-0076; 41-1480; 07-0042	205,35	0,3542
45,8221	1,98031	46-1045; 41-1480	213,56	0,1771
47,7116	1,90620	24-0027	134,20	0,4133
48,6897	1,86863	24-0027	151,24	0,2160

Table A-12 the peaks list and the mineral matched by code from sample BS

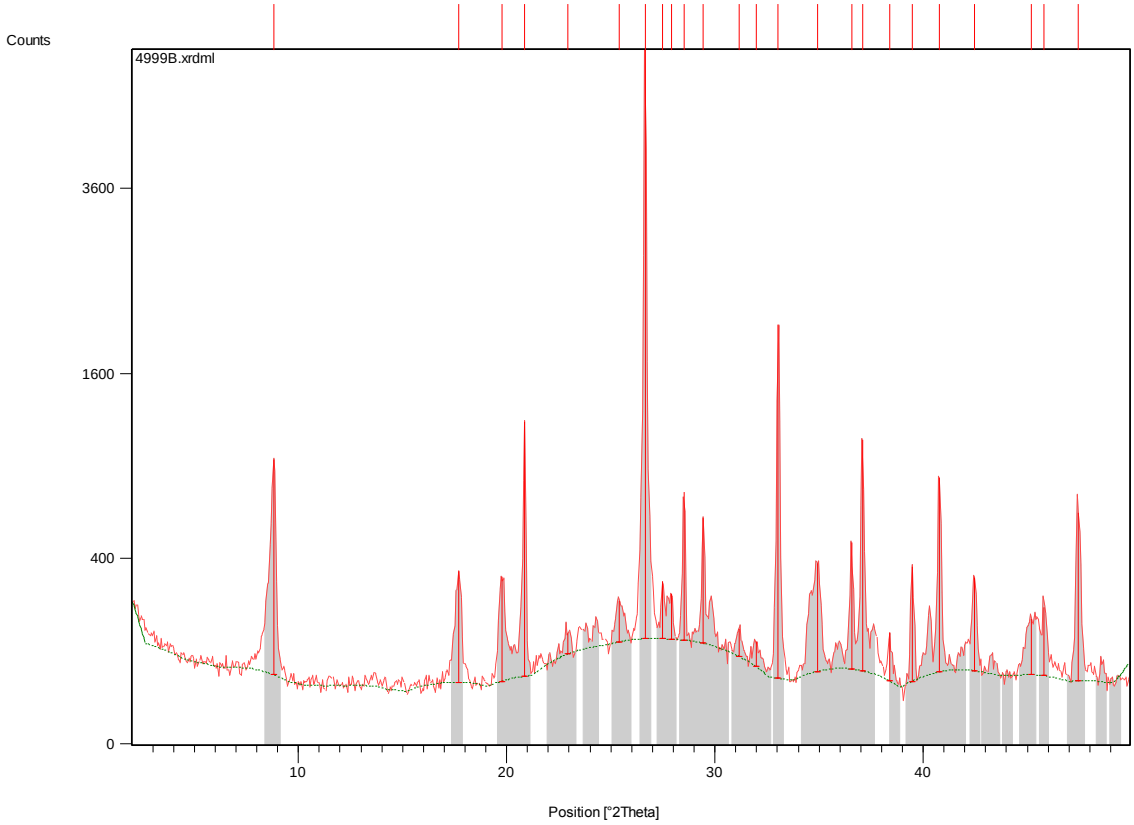

Figure A-13 Diffractogram of sample KS2 from the Konows gate area

Compound Name	Ref. Code	Empirical Formula	Score
Quartz, syn	46-1045	Si O2	68
Pyrite	24-0076	Fe S2	56
Illite-2\ITM\RG#1 [NR]	26-0911	(K , H3 O) Al2 Si3 Al O10 (O H)2	38
Calcite	47-1743	Ca C O3	41
Microcline	01-0705	K Al Si3 O8	30
Illite-2\ITM#2\RG	24-0495	K0.7 Al2.1 (Si , Al)4 O10 (O H)2	34

Table A-13 Minerals identified in the KS2 sample of the Konows gate area

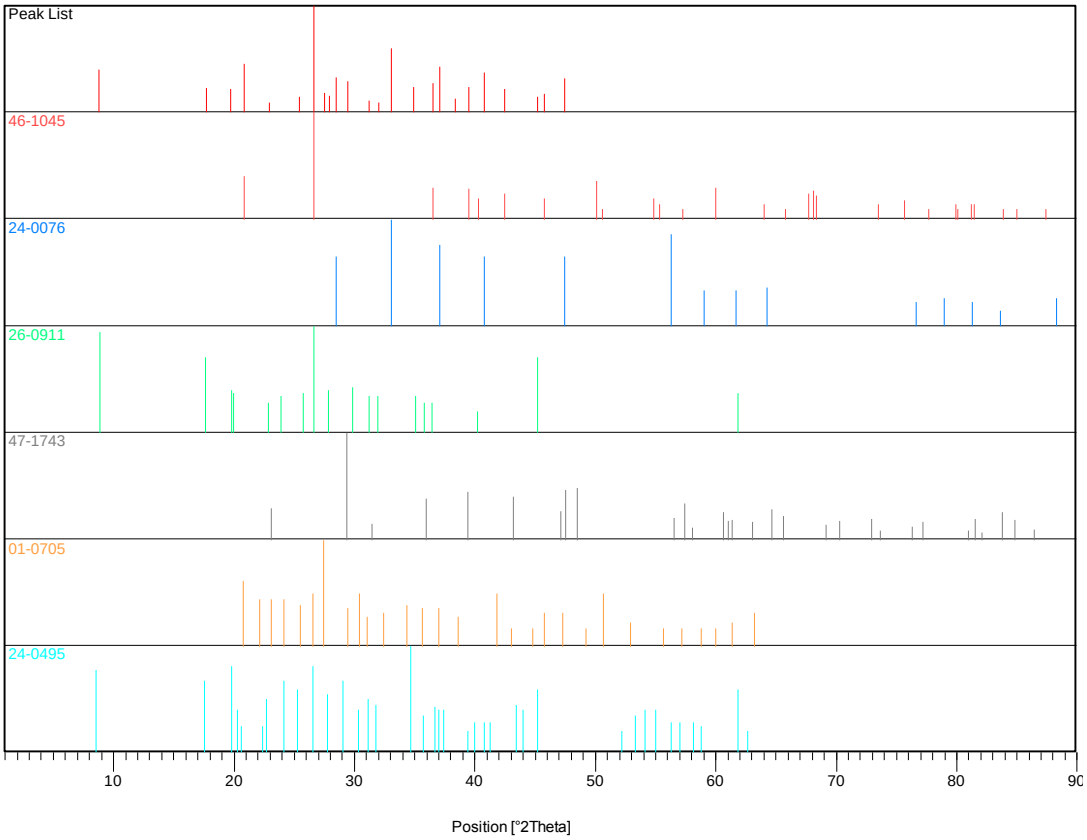

Figure A-14 Pattern of the peaks and identified minerals from the sample KS2

Pos. [°2Th.]	d-spacing [Å]	Matched by	Height [cts]	FWHM [°2Th.]
8,8058	10,04224	26-0911; 24-0495	891,60	0,2362
17,7028	5,01025	26-0911; 24-0495	305,71	0,2362
19,7552	4,49412	26-0911; 24-0495	280,66	0,2952
20,8469	4,26116	46-1045; 01-0705; 24-0495	1157,37	0,1771
22,9514	3,87499	26-0911; 47-1743; 01-0705	48,19	0,3542
25,4170	3,50440	01-0705; 24-0495	118,15	0,4723
26,6403	3,34620	46-1045; 26-0911; 01-0705; 24-0495	5595,27	0,1771
27,4863	3,24510	01-0705	182,15	0,1771
27,9000	3,19791	26-0911; 24-0495	135,17	0,1500
28,5081	3,13107	24-0076	616,33	0,1771
29,4364	3,03441	47-1743; 01-0705	479,86	0,1771
31,1798	2,86860	26-0911; 01-0705; 24-0495	65,37	0,3542
31,9897	2,79780	26-0911; 24-0495	53,47	0,3542
33,0448	2,71084	24-0076	2004,81	0,1771
34,9297	2,56876	26-0911; 24-0495	319,24	0,2362
36,5546	2,45822	46-1045; 26-0911; 24-0495	411,41	0,1771
37,0811	2,42452	24-0076; 01-0705; 24-0495	1021,81	0,1771
38,3891	2,34487	01-0705	98,47	0,2362
39,4832	2,28237	46-1045; 47-1743; 24-0495	322,64	0,1771
40,7800	2,21274	24-0076; 24-0495	769,61	0,1771
42,4659	2,12872	46-1045	260,41	0,1771
45,1949	2,00632	26-0911; 24-0495	125,76	0,4723
45,7955	1,98140	46-1045; 01-0705	164,70	0,3542
47,4497	1,91453	24-0076; 47-1743; 01-0705	579,57	0,2880

Table A-14 the peaks list and the mineral matched by code from sample KS2

Appendix - B

Chemical Analysis of sulfides

Analysis of sulfur from Konows gate sample – KS1

Reactive sulfur (Monosulfides)

Sample weight (g)	10
Volume of iodine used in the solution to react with CdS (ml)	20
Normality in the iodine solution	0.1
Volume of thiosulfate needed to neutralize the iodine solution used i9n the analysis	20
Normality in the thiosulfate solution	0.1
Volume of the thiosulfate used to consume the rest of the iodine solution in the analysis	17.7
% reactive sulfur (S)	0.037

Acid soluble sulfate

Sample weight (g)	10
Weight of precipitated barium sulfate	0.0198
% wt sulfate (SO3)	0.068
% sulfur (S) from wt sulfate	0.027

Total sulfur (sum of monosulfides, disulfides and acid soluble sulfates)

Sample weight (g)	1.0
Weight of precipitated barium sulfate after oxidation with sulfide	0.531
% total sulfur (S)	7.29

Analysis of sulfur from Konows gate sample – KS2

Reactive sulfur (Monosulfides)

Sample weight (g)	10
Volume of iodine used in the solution to react with CdS (ml)	20
Normality in the iodine solution	0.1
Volume of thiosulfate needed to neutralize the iodine solution used i9n the analysis	20
Normality in the thiosulfate solution	0.1
Volume of the thiosulfate used to consume the rest of the iodine solution in the analysis	17.9
% reactive sulfur (S)	0.034

Acid soluble sulfate

Sample weight (g)	10
Weight of precipitated barium sulfate	0.0255
% wt sulfate (SO3)	0.087
% sulfur (S) from wt sulfate	0.035

Total sulfur (sum of monosulfides, disulfides and acid soluble sulfates)

Sample weight (g)	1.0
Weight of precipitated barium sulfate after oxidation with sulfide	0.7008
% total sulfur (S)	9.62

Analysis of sulfur from Konows gate black shale sample – BS

Reactive sulfur (Monosulfides)

Sample weight (g)	10
Volume of iodine used in the solution to react with CdS (ml)	none
Normality in the iodine solution	none
Volume of thiosulfate needed to neutralize the iodine solution used i9n the analysis	none
Normality in the thiosulfate solution	none
Volume of the thiosulfate used to consume the rest of the iodine solution in the analysis	none
% reactive sulfur (S)	<0.001

Acid soluble sulfate

Sample weight (g)	10
Weight of precipitated barium sulfate	0.0072
% wt sulfate (SO3)	0.025
% sulfur (S) from wt sulfate	0.01

Total sulfur (sum of monosulfides, disulfides and acid soluble sulfates)

Sample weight (g)	1.0
Weight of precipitated barium sulfate after oxidation with sulfide	0.0619
% total sulfur (S)	0.85

Appendix - C

Petrography Microscopic Results

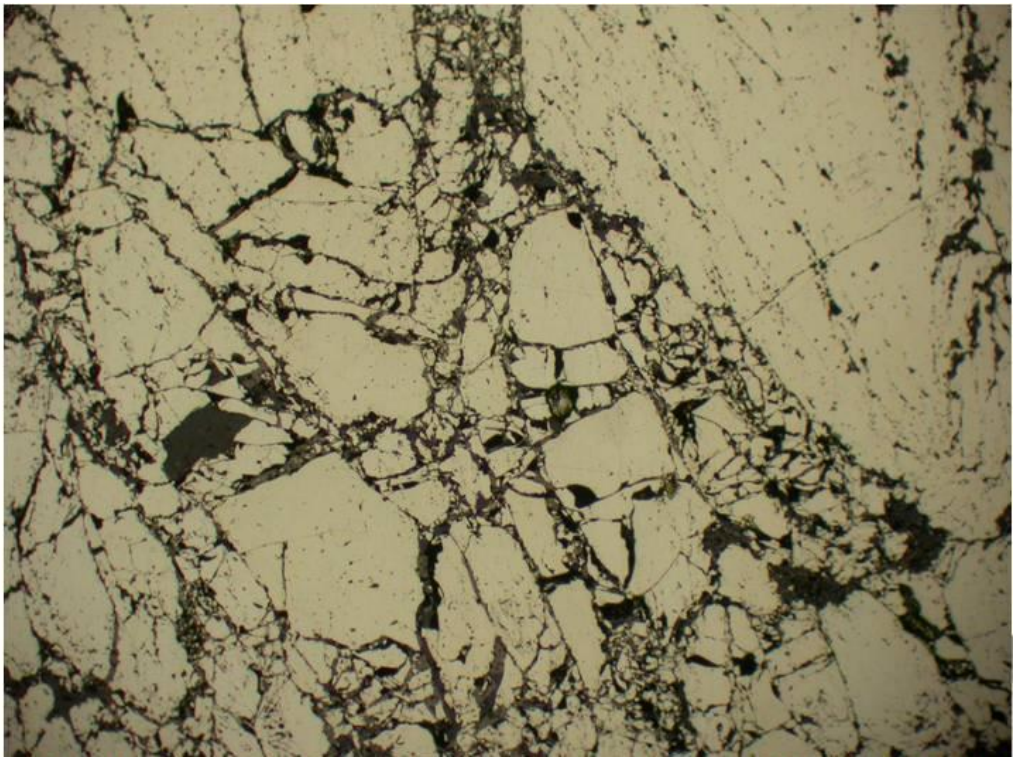

Figure C-1 Fracture of pyrite due to tectonization from Konows gate area. Recrystallized pyrite X10 objective lenses KS-2

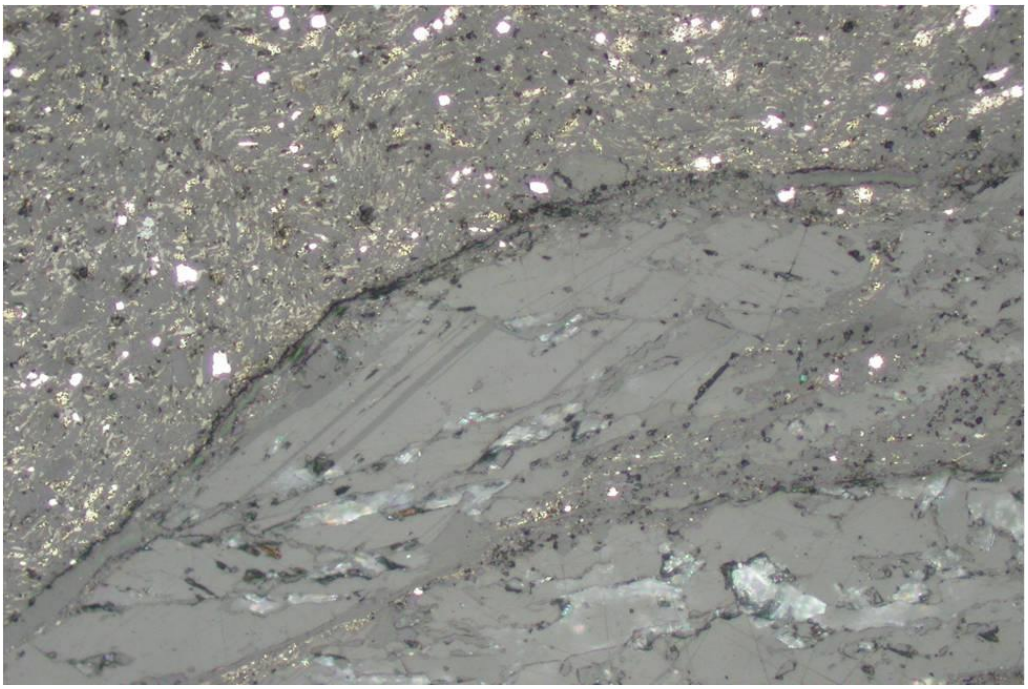

Figure C-2 Calcite and framboidal pyrite with white spots from Konows gate area. KS-2 X40 objective lenses

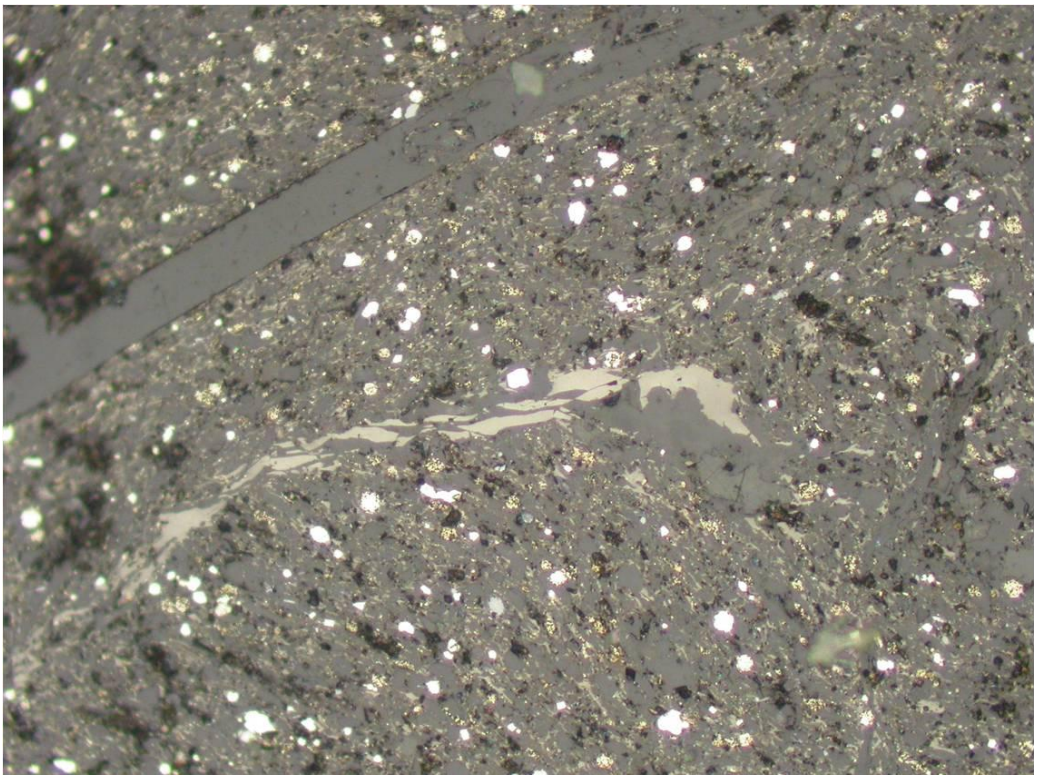

Figure C-3 Yellow grey formation of graphite in vein recrystallized and framboidal pyrite with white spots in the Konows gate area,KS-2 X40

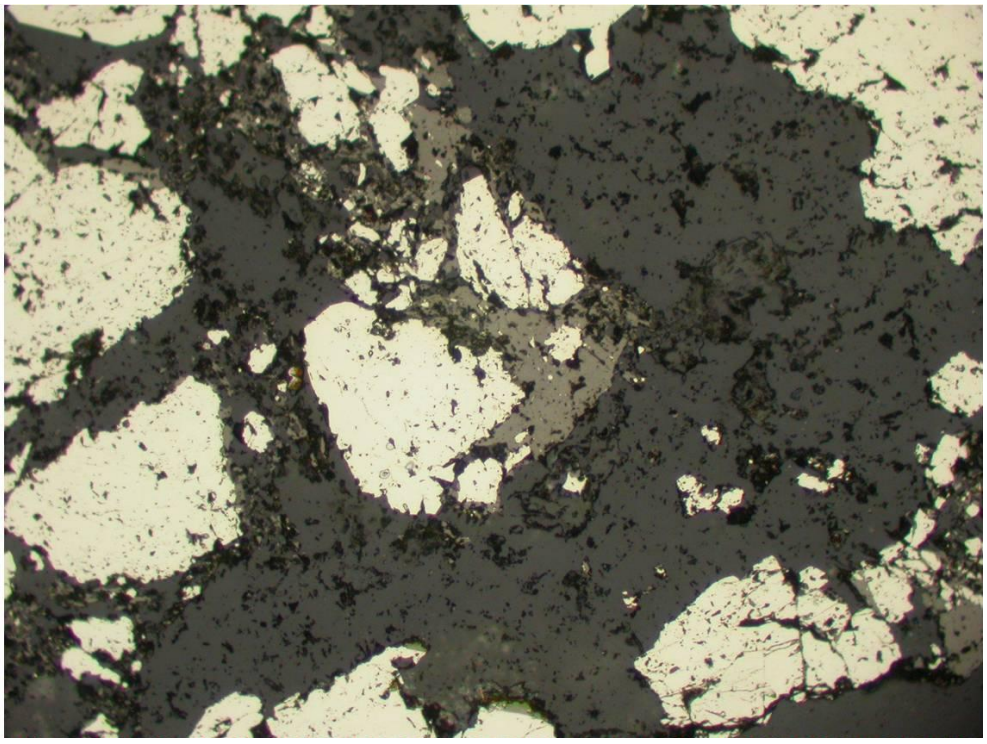

Figure C-4 Recrystallization of framboidal pyrite from Konows gate area, X20 KS-1

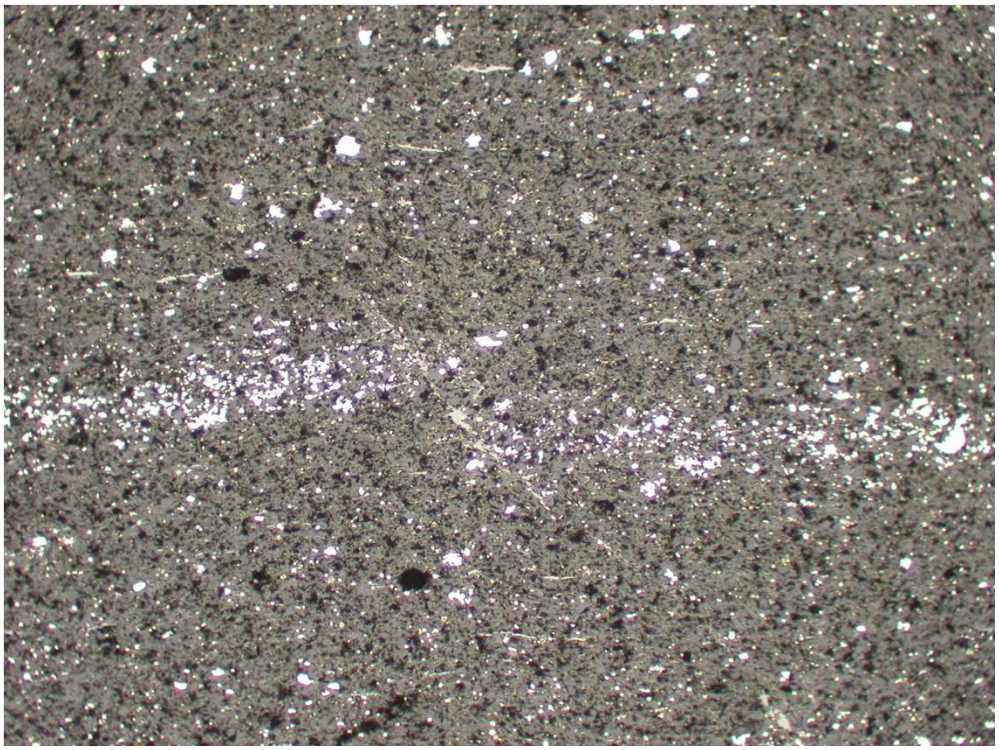

Figure C-5 layer of framboidal pyrite with graphite on fault plane, X10 SM

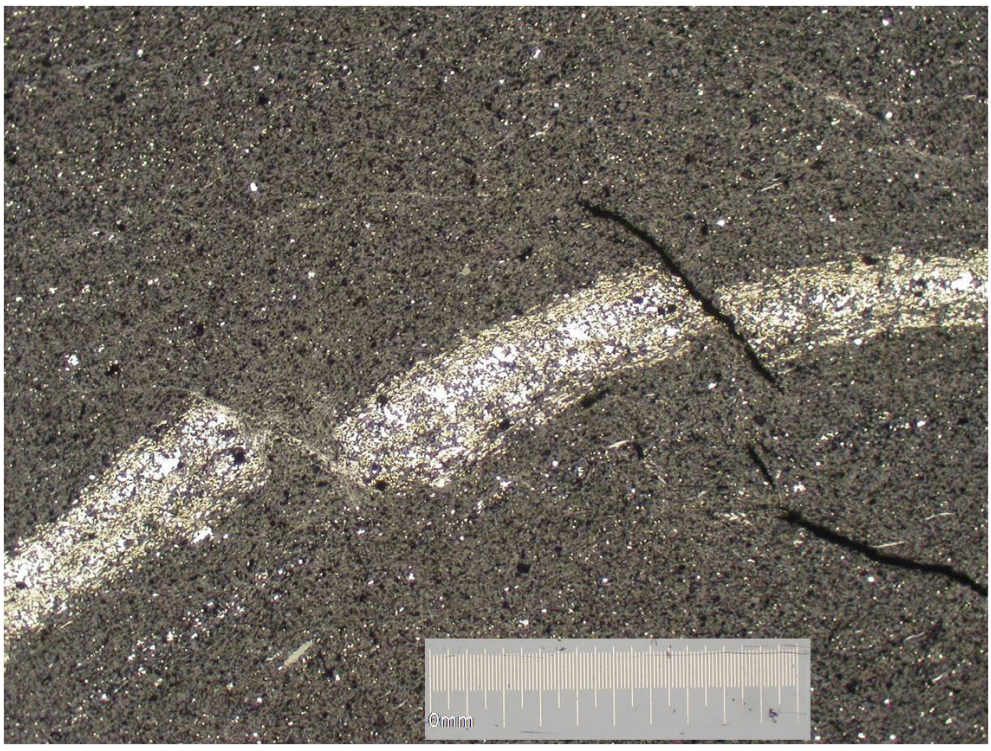

Figure C-6 Faulted pyrite layer with recrystallized graphite in the fault zone, X5 SWE

Figure C-7 Tectonized “fish” of recrystallized pyrite (with chalcopyrite) rimmed with recrystallized coarse graphite. X5 BS

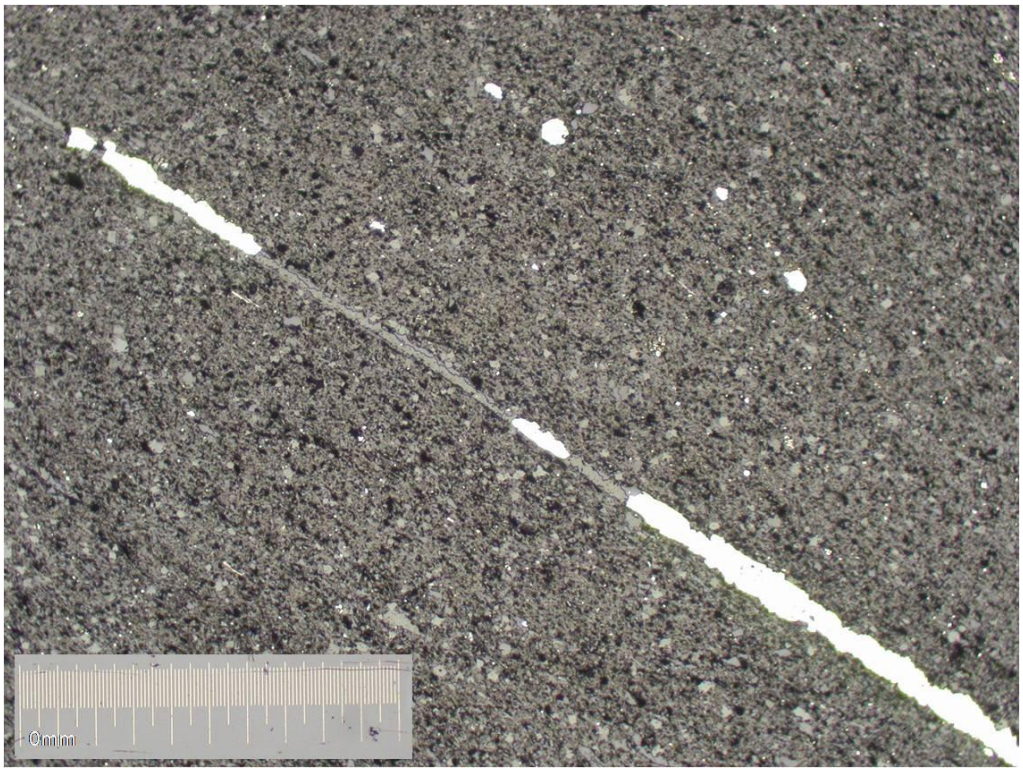

Figure C-8 Formation of calcite and pyrite in the vein, X5 BS

Appendix - D

Modeling Script in PREEQC

Pyrite oxidation with calcite

```
Title pyrite oxidation

SOLUTION 1
pH 7.6
temp 25
-units mg/l
Ca 615
Na 26
K 22
Mg 110
Cl 276
N(+5) 25
S(+6) 1841

Phases
Pyrrhotite
      FeS +1.0000 H+  =  + 1.0000 Fe++ + 1.0000 HS-
      log_k          -3.7193
      delta_H              -7.9496    kJ/mol
EQUILIBRIUM_PHASES 1
Pyrrhotite 0 0.05
Goethite 2
Calcite 0 2.837
O2(g) -0.7 4

 RATES
 Pyrite  # rates from data compiled by Williamson and Rimstidt 1994, GCA 58, 5443
 -start
  1 A = 0.73326* m0   # initial surface area in m2 indicates 200 um size crystals
 10 if SI("Pyrite")>0 then goto 100  # step out when supersaturated...
 20 fH = mol("H+")
 30 fFe2 = (1 + tot("Fe(2)") / 1e-6)
 50 rO2 = 10^-8.19 * mol("O2")^0.5 * fH^-0.11    # ...rate with oxygen
 60 rO2_Fe3 = 6.3e-4 * tot("Fe(3)")^0.92 * fFe2^-0.43 # .rate with oxygen and Fe3+
 70 goto 90
 90 rate = A * (m/m0)^0.67 * (rO2 + rO2_Fe3) * (1 - SR("Pyrite"))   # ...sum terms, zero at equilibrium
 100 save rate * time
 -end
KINETICS 1
  Pyrite; -m0 3.015; -steps 3.15e9 in 12 time steps
INCREMENTAL_REACTIONS true

SELECTED_OUTPUT
-file withcalcite.csv
-totals Ca S(6) C(4) Fe(2) Fe(3)
-molalities CaSO4 FeSO4 FeCO3 Fe+2 Fe+3

USER_GRAPH
 -chart_title "Pyrite Oxidation with calcite"
 -initial_solutions false
 -axis_titles Time(years) Concentration(mol/l) pH
 -headings time Pyrite O2(g) Ca S(6) C(4) Fe(2)*1e2 Fe(3)*1e8 FeSO4*1e2 FeCO3*1e7 CaSO4 pH
 -start
 10 graph_x total_time/31557600
 20 graph_y kin("Pyrite"), 10^si("O2(g)"), tot("Ca"), tot("S(6)"), tot("C(4)"), tot ("Fe(2)")*1e2, tot("Fe(3)")*1e8, mol("FeSO4")*1e2,
mol("FeCO3")*1e6, mol("CaSO4")
 30 graph_sy  -la("H+")
 -end
END
```

Pyrite oxidation in the absence of calcite

```
Title pyrite oxidation
SOLUTION 1
pH 7.6
temp 25
-units mg/l
Ca 615
Na 26
K 22
Mg 110
Cl 276
N(+5) 25
S(+6) 1841

EQUILIBRIUM_PHASES 1
Goethite 2
#Calcite 0
O2(g) -0.7 4

 RATES
 Pyrite  # rates from data compiled by Williamson and Rimstidt 1994, GCA 58, 5443
 -start
  1 A = 0.73326* m0   # initial surface area in m2 indicates 200 um size crystals
 10 if SI("Pyrite")>0 then goto 100  # step out when supersaturated...
 20 fH = mol("H+")
 30 fFe2 = (1 + tot("Fe(2)") / 1e-6)
 50 rO2 = 10^-8.19 * mol("O2")^0.5 * fH^-0.11    # ...rate with oxygen
 60 rO2_Fe3 = 6.3e-4 * tot("Fe(3)")^0.92 * fFe2^-0.43 # .rate with oxygen and Fe3+
 70 goto 90
 80 rem
 81 rFe3 = 1.9e-6*tot("Fe(3)")^0.28*fFe2^-0.52*fH^-0.3
 90 rate = A * (m/m0)^0.67 * (rO2 + rO2_Fe3 + rFe3) * (1 - SR("Pyrite"))   # ...sum terms, zero at equilibrium
 100 save rate * time
 -end

KINETICS 1
  Pyrite; -m0 3.015; -steps 6.048e5 in 13 time steps

INCREMENTAL_REACTIONS true

SELECTED_OUTPUT
-file woutcalcite.csv
-totals Ca S(6) Fe(2) Fe(3)
-molalities CaSO4 FeSO4 Fe+2 Fe+3
USER_GRAPH
 -chart_title "Pyrite oxidation in the absence of calcite"
 -initial_solutions false
 -axis_titles "Time/days" "Concentration(mol/l)" "pH"
 -headings time Pyrite O2(g) Ca S(6) Fe(2) Fe(3) FeSO4 CaSO4 pH
```

```
 -start
 10 graph_x total_time/86400
 20 graph_y kin("Pyrite"), 10^si("O2(g)"), tot("Ca"), tot("S(6)"), tot("Fe(2)"), tot("Fe(3)"), mol("FeSO4"), mol("CaSO4")
 30 graph_sy  -la("H+")
 -end
END
```

Pyrite oxidation with 0.05 moles/liter pyrrhotite

```
Title pyrite oxidation

SOLUTION 1
pH 7.6
temp 25
-units mg/l
Ca 615
Na 26
K 22
Mg 110
Cl 276
N(+5) 25
S(+6) 1841

phases
Pyrrhotite
      FeS +1.0000 H+  =  + 1.0000 Fe++ + 1.0000 HS-
      log_k          -3.7193
      delta_H            -7.9496   kJ/mol
EQUILIBRIUM_PHASES 1
pyrrhotite 0 0.0521   #reactive sulfur above 0.01% is has an effect
Goethite 2
Calcite 0 2.837
O2(g) -0.7  4

 RATES
 Pyrite  # rates from data compiled by Williamson and Rimstidt 1994, GCA 58, 5443
 -start
  1 A = 0.73326* m0   # initial surface area in m2 indicates 200 um size crystals
 10 if SI("Pyrite")>0 then goto 100  # step out when supersaturated...
 20 fH = mol("H+")
 30 fFe2 = (1 + tot("Fe(2)") / 1e-6)
 50 rO2 = 10^-8.19 * mol("O2")^0.5 * fH^-0.11    # ...rate with oxygen
 60 rO2_Fe3 = 6.3e-4 * tot("Fe(3)")^0.92 * fFe2^-0.43 # .rate with oxygen and Fe3+
 70 goto 90
 90 rate = A * (m/m0)^0.67 * (rO2 + rO2_Fe3) * (1 - SR("Pyrite"))   # ...sum terms, zero at equilibrium
 100 save rate * time
 -end
KINETICS 1
  Pyrite; -m0 3.015; -steps 3.15e9 in 12 time steps #time is 100 years. if it is 10 years the default 10 mol oxygen will be finshed
and error show up
INCREMENTAL_REACTIONS true
```

```
SELECTED_OUTPUT
-file oxgenatedwater.csv
-totals Ca S(6) C(4) Fe(2) Fe(3)
-molalities CaSO4 FeSO4 FeCO3 Fe+2 Fe+3

USER_GRAPH
 -chart_title "Pyrite Oxidation with atomspheric oxygen and water"
 -initial_solutions false
 -axis_titles Time(years) Concentration(mol/l) pH
 -headings time Pyrite O2(g) Ca S(6) C(4) Fe(2) Fe(3) FeSO4 FeCO3 CaSO4 pH
 -start
 10 graph_x total_time/31557600
 20 graph_y kin("Pyrite"), 10^si("O2(g)"), tot("Ca"), tot("S(6)"), tot("C(4)"), tot ("Fe(2)"), tot("Fe(3)"), mol("FeSO4"), mol("FeCO3"),
mol("CaSO4")
 30 graph_sy  -la("H+")
 -end
END
```

Pyrite oxidation with 0.5 moles/liter pyrrhotite

```
Title pyrite oxidation

SOLUTION 1
pH 7.6
temp 25
-units mg/l
Ca 615
Na 26
K 22
Mg 110
Cl 276
N(+5) 25
S(+6) 1841

phases
Pyrrhotite
      FeS +1.0000 H+  =  + 1.0000 Fe++ + 1.0000 HS-
      log_k          -3.7193
      delta_H            -7.9496   kJ/mol
EQUILIBRIUM_PHASES 1
pyrrhotite 0 0.521   #reactive sulfur above 0.01% is has an effect
Goethite 2
Calcite 0 2.837
O2(g) -0.7  4

 RATES
 Pyrite  # rates from data compiled by Williamson and Rimstidt 1994, GCA 58, 5443
 -start
  1 A = 0.73326* m0   # initial surface area in m2 indicates 200 um size crystals
```

```
 10 if SI("Pyrite")>0 then goto 100  # step out when supersaturated...
 20 fH = mol("H+")
 30 fFe2 = (1 + tot("Fe(2)") / 1e-6)
 50 rO2 = 10^-8.19 * mol("O2")^0.5 * fH^-0.11    # ...rate with oxygen
 60 rO2_Fe3 = 6.3e-4 * tot("Fe(3)")^0.92 * fFe2^-0.43 # .rate with oxygen and Fe3+
 70 goto 90
 90 rate = A * (m/m0)^0.67 * (rO2 + rO2_Fe3) * (1 - SR("Pyrite"))   # ...sum terms, zero at equilibrium
 100 save rate * time
 -end
KINETICS 1
  Pyrite; -m0 3.015; -steps 3.15e9 in 12 time steps #time is 100 years. if it is 10 years the default 10 mol oxygen will be finshed and error show up
INCREMENTAL_REACTIONS true

SELECTED_OUTPUT
-file oxgenatedwater.csv
-totals Ca S(6) C(4) Fe(2) Fe(3)
-molalities CaSO4 FeSO4 FeCO3 Fe+2 Fe+3

USER_GRAPH
 -chart_title "Pyrite Oxidation with atomspheric oxygen and water"
 -initial_solutions false
 -axis_titles Time(years) Concentration(mol/l) pH
 -headings time Pyrite O2(g) Ca S(6) C(4) Fe(2) Fe(3) FeSO4 FeCO3 CaSO4 pH
 -start
 10 graph_x total_time/31557600
 20 graph_y kin("Pyrite"), 10^si("O2(g)"), tot("Ca"), tot("S(6)"), tot("C(4)"), tot ("Fe(2)"), tot("Fe(3)"), mol("FeSO4"), mol("FeCO3"), mol("CaSO4")
 30 graph_sy  -la("H+")
 -end
END
```

Pyrite oxidation with atmospheric level oxygen and water

```
Title pyrite oxidation

SOLUTION 1
pH 7.6
temp 25
-units mg/l
Ca 615
Na 26
K 22
Mg 110
Cl 276
N(+5) 25
S(+6) 1841

phases
```

```
Pyrrhotite
      FeS +1.0000 H+  =  + 1.0000 Fe++ + 1.0000 HS-
      log_k          -3.7193
      delta_H          -7.9496   kJ/mol
EQUILIBRIUM_PHASES 1
pyrrhotite 0 0.0521
Goethite 2
Calcite 0 2.837
O2(g) -0.7

 RATES
 Pyrite  # rates from data compiled by Williamson and Rimstidt 1994, GCA 58, 5443
 -start
  1 A = 0.73326* m0   # initial surface area in m2 indicates 200 um size crystals
 10 if SI("Pyrite")>0 then goto 100  # step out when supersaturated...
 20 fH = mol("H+")
 30 fFe2 = (1 + tot("Fe(2)") / 1e-6)
 50 rO2 = 10^-8.19 * mol("O2")^0.5 * fH^-0.11    # ...rate with oxygen
 60 rO2_Fe3 = 6.3e-4 * tot("Fe(3)")^0.92 * fFe2^-0.43 # .rate with oxygen and Fe3+
 70 goto 90
 90 rate = A * (m/m0)^0.67 * (rO2 + rO2_Fe3) * (1 - SR("Pyrite"))   # ...sum terms, zero at equilibrium
 100 save rate * time
 -end
KINETICS 1
  Pyrite; -m0 0.3015; -steps 1.57788e10 in 10 time steps #time is 1000 years. the default 10 mol oxygen
INCREMENTAL_REACTIONS true

SELECTED_OUTPUT
-file oxgenatedwater.csv
-totals Ca S(6) C(4) Fe(2) Fe(3)
-molalities CaSO4 FeSO4 FeCO3 Fe+2 Fe+3

USER_GRAPH
 -chart_title "Pyrite Oxidation with atomspheric oxygen and water"
 -initial_solutions false
 -axis_titles Time(Days) Concentration(mol/l) pH
 -headings time Pyrite O2(g) Ca S(6) C(4) Fe(2)*1e14 Fe(3)*1e9 FeSO4*1e15 FeCO3*1e19 CaSO4 pH
 -start
 10 graph_x total_time/31557600
 20 graph_y kin("Pyrite"), 10^si("O2(g)"), tot("Ca"), tot("S(6)"), tot("C(4)"), tot ("Fe(2)")*1e14, tot("Fe(3)")*1e9,
mol("FeSO4")*1e15, mol("FeCO3")*1e19, mol("CaSO4")
 30 graph_sy  -la("H+")
 -end
END
```